Integrating InP Waveguides: Measuring Processing Stress and Modelling Intersecting Waveguides With Low Crosstalk

Michael G. Daly, B.Sc.(Eng.), M.Eng.

A thesis submitted to the School of Graduate Studies in partial fulfillment of the requirements for the degree
Doctor of Philosophy
McMaster University
February 1996

DOCTOR OF PHILOSOPHY (1996) McMASTER UNIVERSITY
(Engineering Physics) Hamilton, Ontario

TITLE: Integrating InP Waveguides: Measuring Processing Stress and Modelling Intersecting Waveguides With Low Crosstalk.

AUTHOR: Michael George Daly, B.Sc. (Eng.) (Queen's University)
M. Eng. (McMaster University)

SUPERVISOR: P.E. Jessop
NUMBER OF PAGES: 116

Integrating InP Waveguides: Measuring Processing Stress and Modelling Intersecting Waveguides With Low Crosstalk

Contents

List of Figures

Abstract

Two major problems in InP waveguide design were studied. The first of these is the effect of processing induced stress on the mode of an InP/InGaAsP waveguide. The stress in such a waveguide was measured by the technique of the Degree of Polarization of Photoluminescence. The measured stress map was modeled to quantify the spatial distribution of index change within the waveguide itself. The mode of the single-mode waveguide with the stress effects was calculated using the beam propagation technique. The resultant mode exhibited a double peaking which agreed well with the observed mode of the actual waveguide.

The second problem studied was that of crossed waveguides. Crossed waveguides are necessary in optoelectronic integrated circuits due to the multiple light paths and planar nature of the fabrication process. Each arm of these crosses requires good throughput with very little power coupled into the other waveguide. Although this is easy to achieve at large crossing angles, at angles below $\approx 10°$ a significant fraction of the light may couple into the crossing waveguide.

This thesis uses the beam propagation method to characterize the loss and crosstalk. Two modified versions of the X-crossed waveguide structure were developed and have shown crosstalk improvements, at angles below 10°, of greater than 20 dB. These improvements are easy to implement and are important due to the extra design freedom they allow the designers of optoelectronic circuits.

Acknowledgments

The accomplishment represented by this thesis is due to the help and support of many people. My thanks goes to my supervisor Paul Jessop for his friendship and support as well as to the members of my supervisory committee - John Simmons and Peter Smith. Doug Bruce deserves thanks for his help and advice as well as for the many lunch time conversations. Although not on my supervisory committee, Dan Cassidy has aided this work a great deal through the loan of equipment as well as through interesting and helpful conversations.

A graduate program would not be the same without the friends who kept me sane when I needed it. Some of these people are: David Jez, Kevin Cearns, Xiucheng Wu, Michael Ersoni and Eugene Tan.

My parents instilled the importance of school from an early age and without their support I would not have come so far. My faith in God was a great help during the rough times which seem to occur in all thesis projects. Lastly, my wife, Ruth, and my son, Graeme, have missed my company, as I have missed theirs, during the long hours it took to produce this thesis. I look forward to having more time to spend with you both.

Chapter 1

Introduction to Integrated Optics

1.1 Introduction

Research in integrated optics began in 1969 with its proposal by Bell Laboratories' S.E. Miller [1]. Miller proposed a hybrid design in which various active devices could be interconnected by a passive dielectric substrate. Since then, monolithic designs which incorporate active and passive devices manufactured from one substrate material have grown in importance. The possible advantages of an optoelectronic integrated circuit (OEIC) include small size, improved cost of production and stability. Miller and those who followed proposed many different materials and techniques for integrating optical waveguides and devices. These consisted of semiconductors, $LiNbO_3$, polymers, and glass in both hybrid and monolithic configurations [2][3].

With the improvement of light emitting diodes (LEDs) and laser diodes (LD's) as well as optical fibre propagation losses the importance of optical communications further spurred the interest in OEICs. Currently interest in OEICs is at its highest level ever but integration is still possible only on a small scale.

This thesis is concerned with two major problems of integration. The first of these deals with the problem of measuring stress due to metal or dielectric overlayers on InP waveguides. The measurement of

stress is an important problem since it can affect the lifetime of devices on the OEIC as well as the waveguide properties by perturbing the refractive index. The second concerns the crossing of waveguides with low loss and low crosstalk. The crossing of waveguides is of extreme importance due to the planar nature made necessary by the current configurations of OEICs.

1.2 Structure of this Thesis

Chapter 1 of this thesis will introduce optical waveguides. Both slab (two-dimensional) waveguides and rectangular (three-dimensional) waveguides will be discussed. Methods of solution for these types of waveguides are presented and discussed. A review of coupled mode theory is also presented.

The integration of devices and fabrication of opto-electronic integrated circuits (OEICs) is summarized to highlight the sources of stress induced in the fabrication process which will be discussed in Chapter 4 and the need for X-crossed waveguides in OEIC's which will be discussed in Chapters 5 and 6.

Chapter 2 introduces the theory of the degree of polarization of photoluminescence. This technique will be used in Chapter 4 to quantify the stress induced by metal contact overlayers on optical waveguides.

Chapter 3 derives the important equations for beam propagation methods (BPM's). These methods and their limitations will be presented. It will be shown how to implement this method both to calculate lowest order eigenmodes and to analyze the propagation of a waveguide mode through a structure.

Chapter 4 shows how the technique of the degree of polarization of photoluminescence and the imaginary distance beam propagation technique can be used to measure the stress caused in a waveguide by a metal contact layer and to model the mode distortion which the stress causes.

Chapter 5 presents a discussion of standard X-crossed waveguide structures and uses a finite difference beam propagation technique to examine the throughput and crosstalk behavior of these crossings.

Chapter 6 uses a finite difference beam propagation technique to

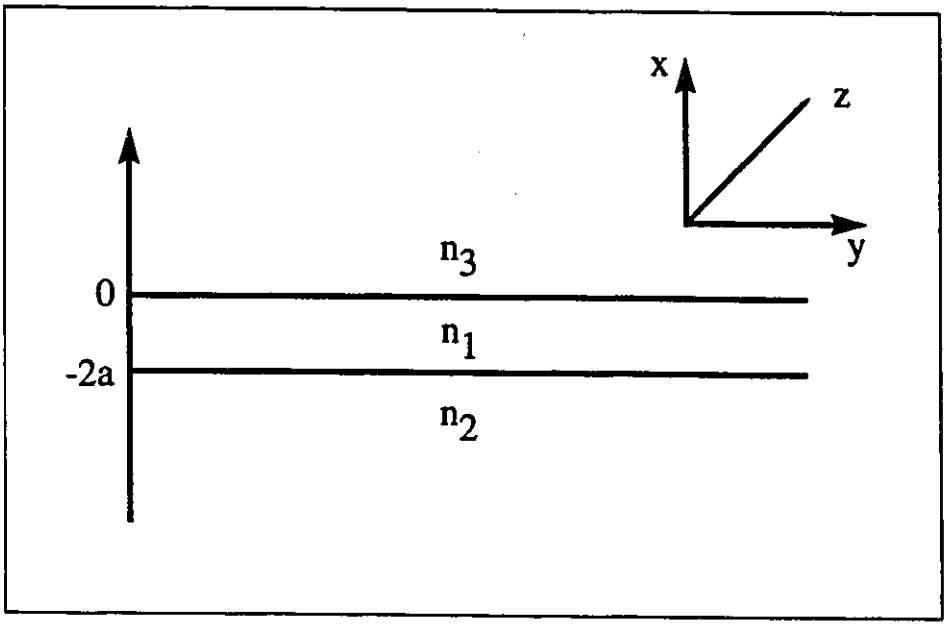

Figure 1.1: The basic geometry for an optical waveguide. To have confinement $n_1 >> n_2$ and $n_1 >> n_3$.

analyze changes in the transverse structure of a waveguide X-crossing. Two improvements are presented which greatly increase the performance of these crossings at certain angles.

The final chapter sums up the results of previous chapters. Suggestions for future work are also presented.

1.3 Optical Waveguides

1.3.1 Introduction

An optical waveguide is a structure that constrains the optical energy to follow a prescribed path. The constraint is produced by varying the refractive index of a material to form light pipes. The refractive index of a material, n, is related to the dielectric constant, ε, by $n^2 = \varepsilon$.

If the waveguide has a refractive index profile that does not vary in the propagation direction (z direction), the refractive index can be

written as

$$n(x, y, z) = n(x, y). \tag{1.1}$$

$n(x, y)$ can be either a real or a complex function. The imaginary component of a medium's refractive index is related to its optical attenuation coefficient, α, by

$$n_i = \frac{\lambda}{4\pi}\alpha \tag{1.2}$$

For simplicity we will assume lossless waveguides, making $n(x, y)$ a real function.

The solution for electromagnetic wave propagation in a waveguide results in stationary states called modes. A waveguide mode propagates without radiating energy. The electric field for such a guided mode has the form

$$\mathbf{E}'(x, y, z) = \mathbf{E}(x, y)e^{i(\beta z - \omega t)}. \tag{1.3}$$

$\mathbf{E}(x, y)$ is called the mode profile or mode and β is the propagation constant of the waveguide mode.

The problem to be solved is to find the function $\mathbf{E}(x, y)$ and β given the refractive index profile $n(x, y)$ and the optical frequency ω. The simplest form of optical waveguide is a slab waveguide. A slab waveguide implies that $\partial/\partial y = 0$.

1.3.2 TE Modes of Slab Waveguides

For a slab waveguide as shown in Figure 1.1 the only non-zero field components for Transverse Electromagnetic (TE) modes are E_y,H_x and H_z. The wave equation [4] becomes

$$\frac{\partial^2 E_y}{\partial x^2} + \left(k_0^2 n^2 - \beta^2\right) E_y = 0 \tag{1.4}$$

with the other non zero components given by

$$H_x = -\frac{\beta}{\omega\mu_0} E_y \tag{1.5}$$

$$H_z = -\frac{1}{i\omega\mu_0}\frac{\partial E_y}{\partial x}. \tag{1.6}$$

The Electric field of confined TE waveguide mode has the following form:

$$E_y = \begin{cases} Ae^{-rx} & x \geq 0 \\ A\cos qx + B\sin qx & 0 \geq x \geq -2a \\ (A\cos 2aq - B\sin 2aq)e^{p(x+2a)} & -2a \geq x. \end{cases} \tag{1.7}$$

The values of p,q, and r are related to the waveguide parameters, through Equation 1.4, by

$$q^2 = n_1^2k^2 - \beta^2 \tag{1.8}$$
$$p^2 = \beta^2 - n_2^2k^2 \tag{1.9}$$
$$r^2 = \beta^2 - n_3^2k^2. \tag{1.10}$$

Similarly the z component of the magnetic field for a TE mode is given by:

$$H_z = \frac{i}{\omega\mu_0}\begin{cases} -rAe^{-rx} & x \geq 0 \\ q(-A\sin qx + B\cos qx) & 0 \geq x \geq -2a \\ p(A\cos 2aq - B\sin 2aq)e^{p(x+2a)} & -2a \geq x \end{cases} \tag{1.11}$$

and the x component is:

$$H_x = \frac{-\beta}{\omega\mu_0}\begin{cases} Ae^{-rx} & x \geq 0 \\ A\cos qx + B\sin qx & 0 \geq x \geq -2a \\ (A\cos 2aq - B\sin 2aq)e^{p(x+2a)} & -2a \geq x. \end{cases} \tag{1.12}$$

1.3.3 TM Modes of Slab Waveguides

In exact analogy to the TE modes, the wave equation for TM modes is

$$\frac{\partial^2 H_y}{\partial x^2} + \left(k_0^2n^2 - \beta^2\right)H_y = 0 \tag{1.13}$$

with the other two non-zero components given as

$$E_x = \frac{\beta}{\omega\varepsilon_0 n^2}H_y \tag{1.14}$$
$$E_z = \frac{1}{i\omega\varepsilon_0 n^2}\frac{\partial H_y}{\partial x}. \tag{1.15}$$

The transverse component of the magnetic field is

$$H_y = \begin{cases} Ce^{-rx} & x \geq 0 \\ C\cos qx + D\sin qx & 0 \geq x \geq -2a \\ (C\cos 2aq - D\sin 2aq)e^{p(x+2a)} & -2a \geq x. \end{cases} \tag{1.16}$$

with the other two non-zero components given by

$$E_z = \frac{-i}{\omega\varepsilon_0} \begin{cases} \frac{-rC}{n_3^2}e^{-rx} & x \geq 0 \\ \frac{q}{n_1^2}(-C\sin qx + D\cos qx) & 0 \geq x \geq -2a \\ \frac{p}{n_2^2}(C\cos 2aq - D\sin 2aq)e^{p(x+2a)} & -2a \geq x \end{cases} \tag{1.17}$$

and

$$E_x = \frac{\beta}{\omega\varepsilon_0} \begin{cases} \frac{1}{n_3^2}Ce^{-rx} & x \geq 0 \\ \frac{1}{n_1^2}C\cos qx + D\sin qx & 0 \geq x \geq -2a \\ \frac{1}{n_2^2}(C\cos 2aq - D\sin 2aq)e^{p(x+2a)} & -2a \geq x. \end{cases} \tag{1.18}$$

1.3.4 Eigenvalue Equations

Applying the boundary conditions of the continuity of the tangential components of the field to Equation 1.7 allows the development of the following eigenvalue equation for the TE modes [4]:

$$\tan(2aq) = \frac{q(p+r)}{q^2 - pr}. \tag{1.19}$$

Similarly from Equation 1.16 the eigenvalue equation for the TM modes is

$$\tan(2aq) = \frac{(n_3^2 p + n_2^2 r)n_1^2 q}{n_2^2 n_3^2 q^2 - n_1^4 pr}. \tag{1.20}$$

1.3.5 Slab Waveguides Greater than Three Layers

For slab waveguides with more than three layers, analytic solutions become unwieldy. Walpita[5] has developed a numerical method which is easily implemented for TE and TM slab waveguides of an arbitrary

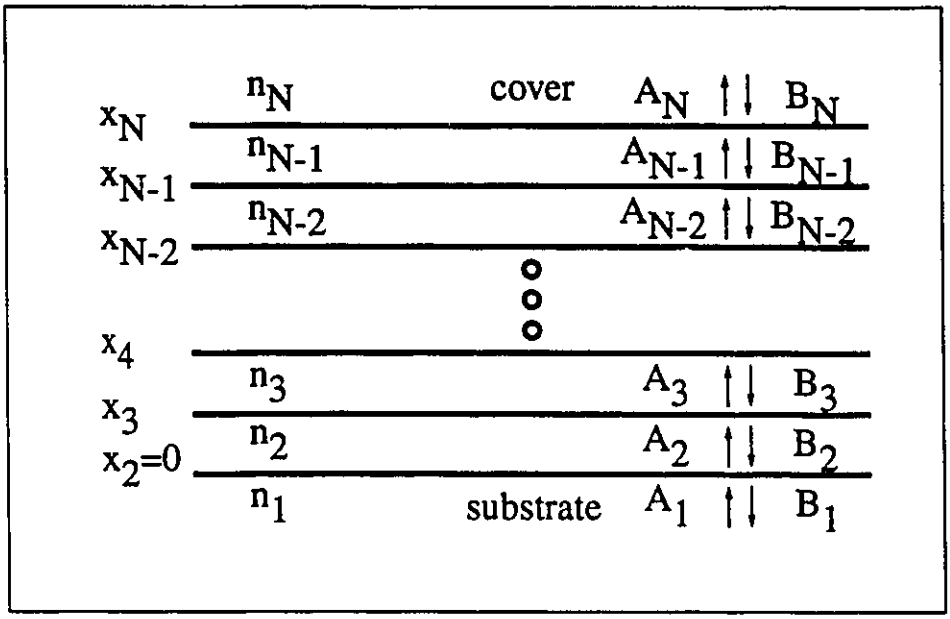

Figure 1.2: An arbitrary N layer slab waveguide.

number of layers. A diagram of an arbitrary N layer slab waveguide is shown in Figure 1.2.

Each of the N layers has a magnetic permeability of $\mu_j, j = 1 \cdots N$ and an electric permittivity of $\varepsilon_{x,j}, j = 1 \cdots N$ and $\varepsilon_{(y,z),j}, j = 1 \cdots N$. The electric displacement in each layer $\mathbf{D}$ is then related to the electric field in each layer $\mathbf{E}$ by

$$\begin{bmatrix} \mathbf{D_x} \\ \mathbf{D_y} \\ \mathbf{D_z} \end{bmatrix} = \varepsilon_0 \begin{bmatrix} n_x^2 & 0 & 0 \\ 0 & n_{y,z}^2 & 0 \\ 0 & 0 & n_{y,z}^2 \end{bmatrix} \begin{bmatrix} \mathbf{E_x} \\ \mathbf{E_y} \\ \mathbf{E_z} \end{bmatrix} \tag{1.21}$$

where ε_0 is the permittivity of free space.

For any layer j, assuming the normal time dependence of the fields, Maxwell's equations hold:

$$\nabla \times \mathbf{E_j} = -i\omega \mathbf{B_j}, \tag{1.22}$$

$$\nabla \times \mathbf{H_j} = i\omega \mathbf{D_j}. \tag{1.23}$$

Further, the electric field in each layer j can be generally written as

$$\mathbf{E_j} = \mathbf{E_{norm}} e^{-i(\beta z - \omega t)} \left[A_j e^{-ip_j(x-x_j)} + B_j e^{ip_j(x-x_j)} \right] \tag{1.24}$$

where β is the propagation constant of the mode to be calculated and E_{norm} is a constant vector which depends on the normalization of the field. p_j is the wavevector component in the x direction. The position x_j occupies the interface between the layers j and $j-1$ with the exception of $x_1 = x_2$.

The values of p and β are related by

$$-p_j^2 = (\beta^2 - k^2 n_{0,j}^2). \tag{1.25}$$

The constant $\mathbf{E_{norm}}$ is

$$\mathbf{E_{norm}} = (0,1,0) \text{ for TE modes} \tag{1.26}$$

$$\mathbf{E_{norm}} = (1,0,0) \text{ for TM modes.} \tag{1.27}$$

The general form of the electric field along with Maxwell's equations gives, for example, for TE waves

$$\mathbf{E_j} = (0,1,0) \left[A_j e^{(-ip_j(x-x_j))} + B_j e^{ip_j(x-x_j)} \right] e^{-i(\beta x - \omega t)} \tag{1.28}$$

$$\mathbf{B_j} = \frac{1}{i\omega} \left[A_j (ip_j, 0, -i\beta) e^{(-ip_j(x-x_j))} \right. \tag{1.29}$$

$$+ \left. B_j (-ip_j, 0, -i\beta) e^{ip_j(x-x_j)} \right] e^{-i(\beta x - \omega t)}. \tag{1.30}$$

Applying the appropriate continuity conditions, which include a finite mode amplitude at $x = \pm\infty$, gives a vector which must be continuous:

$$\begin{bmatrix} \mathbf{E_{yj}} \\ i\omega \mathbf{B_{xj}} \end{bmatrix} = \left[\mathbf{M_j}\right] \begin{bmatrix} A_j \\ B_j \end{bmatrix} \tag{1.31}$$

where for $x_j \leq x \leq x_{j+1}$

$$\left[\mathbf{M_j}\right] = \begin{bmatrix} e^{-ip_j x - x_j} & e^{ip_j(x-x_j)} \\ -\Gamma_j e^{-ip_j(x-x_j)} & \Gamma_j e^{-ip_j(x-x_j)} \end{bmatrix} \tag{1.32}$$

and where

$$\Gamma_j = \frac{p_j}{i} \qquad \text{for TE modes} \tag{1.33}$$

$$\Gamma_j = \frac{p_j}{in^2} \qquad \text{for TM modes.} \tag{1.34}$$

The continuity condition for the fields at each interface allows the development of a relation between the unknowns in each layer.

$$\begin{bmatrix} A_j \\ B_j \end{bmatrix} = \begin{bmatrix} \frac{1}{2} & -\frac{1}{2\Gamma_j} \\ \frac{1}{2} & \frac{1}{2\Gamma_j} \end{bmatrix} \left[\mathrm{M_j}\right]_{x=x_j} \begin{bmatrix} A_{j-1} \\ B_{j-1} \end{bmatrix} \tag{1.35}$$

The recursion relation of the previous equation may be used to generate a 2x2 matrix which relates the constants A_N and B_1.

$$\begin{bmatrix} A_N \\ 0 \end{bmatrix} = \begin{bmatrix} a_1 & a_2 \\ a_3 & a_4 \end{bmatrix} \begin{bmatrix} 0 \\ B_1 \end{bmatrix} \tag{1.36}$$

B_1 is an arbitrary non-zero value. A_1 and B_N must be zero to have wavefunctions which behave appropriately at the limits of the range for x. To obtain the zero on the left of the = sign it is then necessary for the value of a_4 to be 0. The zeros of $a_4(\beta)$ will then provide the values of β for which a guided mode occurs.

If the waveguide has complex indices, β will itself be complex. This method can then be complicated by the need to find the zeros of a two dimensional function. However, for most cases of interest the zeros of the real part of a_4 will be in the vicinity of the complex zeros of a_4 and Newton's method will work. This is the case for all structures considered in this thesis.

1.3.6 Modes of Three-Dimensional Waveguides

In 3-D optical waveguides, where the refractive index is a function of x and y ,the wave equation is not analytically soluble. In this situation there are two widely used approximate methods of solution. These methods are generally applicable if the modes are not near cutoff and the aspect ratio of the waveguide is far from unity.

The modes of such a waveguide are no longer true TE and TM modes. The mode which is (TE like) polarized predominantly in the y direction is referred to as the $E^y_{n,m}$ mode where the n and m are the number of field nodes in the x and y directions respectively. The TM like mode is the $E^x_{n,m}$ mode.

In discussing the specific applicability of each of the following mode calculation methods it is generally necessary to classify the waveguide

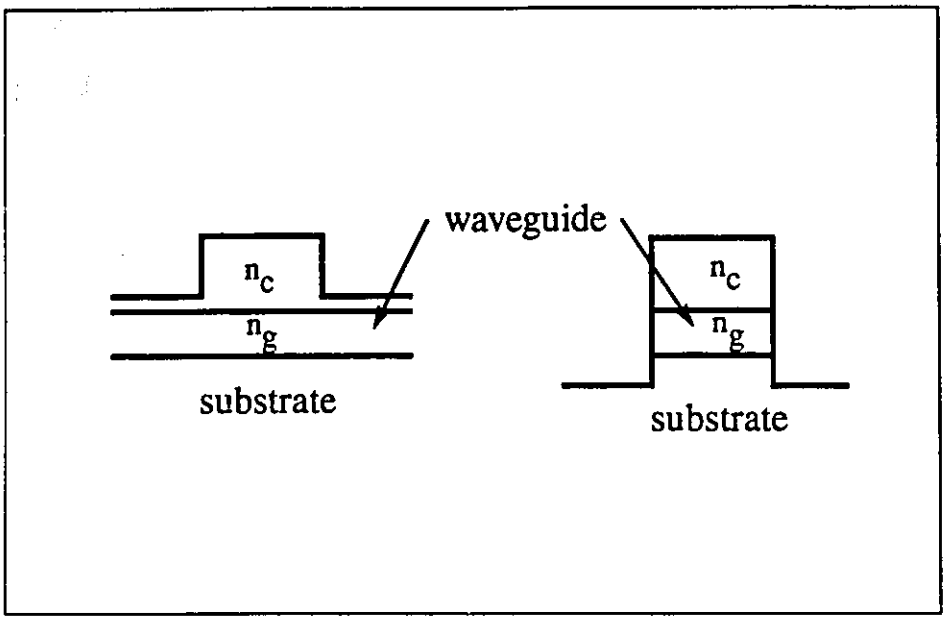

Figure 1.3: A comparison of strip-loaded (left) and step-index (right) waveguide structures.

type. Most three-dimensional semiconductor waveguide structures fall into two broad categories: strip-loaded and step-index. These structures are pictured in Figure 1.3. The major difference between these structures is whether there is a lateral step discontinuity in the waveguiding layer.

Marcatili's Method

Marcatili's method [6] is the first and simplest of these methods. Figure 1.4 shows the geometry under consideration. Most of the optical power is confined to the centre region while lesser amounts are in the edge regions with the four corner regions having the least of all. Marcatili's method concentrates on calculating the fields where the optical power is the greatest and neglecting field matching in the four corners.

The fields for the structure of Figure 1.4 are given by [7]

$$\text{Region1} \quad : \quad A\cos(k_x x + \phi_1) \cdot \cos(k_y y + \phi_2) \tag{1.37}$$

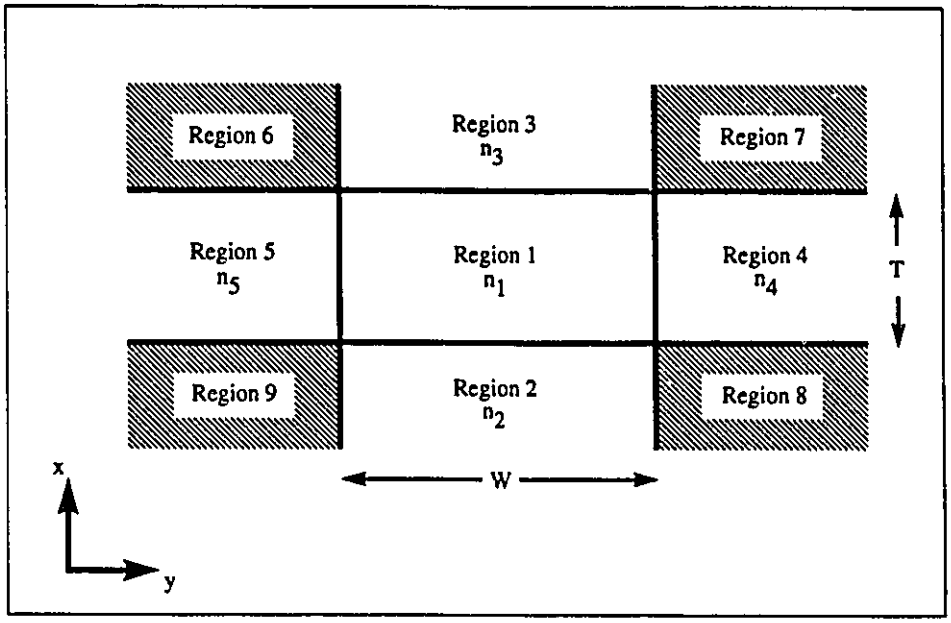

Figure 1.4: The geometry used for Marcatili's method. In most semiconductor devices $T < W$ and $\hat{x}$ is normal to the substrate.

$$\begin{aligned}
\text{Region2} &: A\cos(k_x T - \phi_1)\cdot\cos(k_y y + \phi_2) \\
&\quad \cdot\exp(\gamma_{x2}(x+T)) && (1.38)\\
\text{Region3} &: A\cos\phi_1\cdot\cos(k_y y + \phi_2)\cdot\exp(-\gamma_{x3}x) && (1.39)\\
\text{Region4} &: A\cos(k_y W/2 + \phi_2)\cdot\cos(k_y x + \phi_1) \\
&\quad \cdot\exp(-\gamma_{y4} - W/2) && (1.40)\\
\text{Region5} &: A\cos(k_y W/2 + \phi_2)\cdot\cos(k_x x + \phi_1) \\
&\quad \cdot\exp(\gamma_{y5}(y + W/2)) && (1.41)
\end{aligned}$$

with the parameters β and γ given by

$$\begin{cases} \beta^2 = k_0^2 n_1^2 - k_x^2 - k_y^2 \\ \gamma_{xi}^2 = (\beta^2 + k_y^2) - k_0^2 n_i^2 \\ \gamma_{yi}^2 = (\beta^2 + k_x^2) - k_0^2 n_i^2 \end{cases} \tag{1.42}$$

The phase term is

$$\phi_1 = \frac{\pi}{2} - \tan^{-1}\left(\frac{n_3}{n_1}\right)^2\left(\frac{k_x}{\gamma_{x3}}\right). \tag{1.43}$$

The eigenvalue equation for k_x is

$$k_x T = (n+1)\pi - \tan^{-1}\left(\frac{n_3}{n_1}\right)^2\left(\frac{k_x}{\gamma_{x3}}\right) - \tan^{-1}\left(\frac{n_2}{n_1}\right)^2\left(\frac{k_x}{\gamma_{x2}}\right) \tag{1.44}$$

and for k_y is

$$k_y W = (m+1)\pi - 2\tan^{-1}\left(\frac{k_y}{\gamma_{y4}}\right). \tag{1.45}$$

Marcatili's method works well for step-index waveguides but for strip-loaded waveguides the effective index method is called for.

Effective Index Method

The effective index method [4] is based on considering distinct regions along one direction (y) and treating the problem in each region as a slab waveguide problem with $n = n(x)$. The arrived upon β's are used to define an effective index for the different regions in the y direction.

$$N_{eff}^{(y)} = \frac{\beta^{(y)}}{k_0} \tag{1.46}$$

These effective index values are then used to solve for the dependence of the electric field profile using a slab waveguide solution. Strip-loaded waveguides can be simply handled with this method. The effective index method is discussed in detail in section 3.6.

Numerical Methods

Numerical methods are a more accurate alternative to the approximate methods above. Finite element methods exist for the calculation of three dimensional modes by direct solution of the vector wave equation, but they are computationally intensive. A variation of the Beam Propagation Method which solves the paraxial wave equation in imaginary space, can also be used to solve for the modes of a waveguide. It is discussed in Section 3.9.

A further benefit to numerical methods is their relatively easy expansion to problems where the refractive index varies as a function of the propagation direction (z). In this case the waveguide modes themselves vary as a function of z. Beam propagation methods (BPM's) can handle this situation. They will be discussed in Chapter 3.

1.3.7 Design of Single-mode Waveguides

Most practical optical waveguides are designed to be single-mode and support only the E^x_{00} and E^y_{00} modes. One reason for this is that any small defects in the waveguides can cause mode conversion to a higher order mode and this can lead to mode interference effects and degraded waveguide performance.

The design of a single-mode optical waveguide by the effective index method requires that the transverse (x) slab waveguides which define the effective indices in the different lateral (y) regions are themselves single-mode. The lateral slab waveguide can then be designed as single mode which, unless very close to a mode cutoff, will give the parameters of a single-mode waveguide.

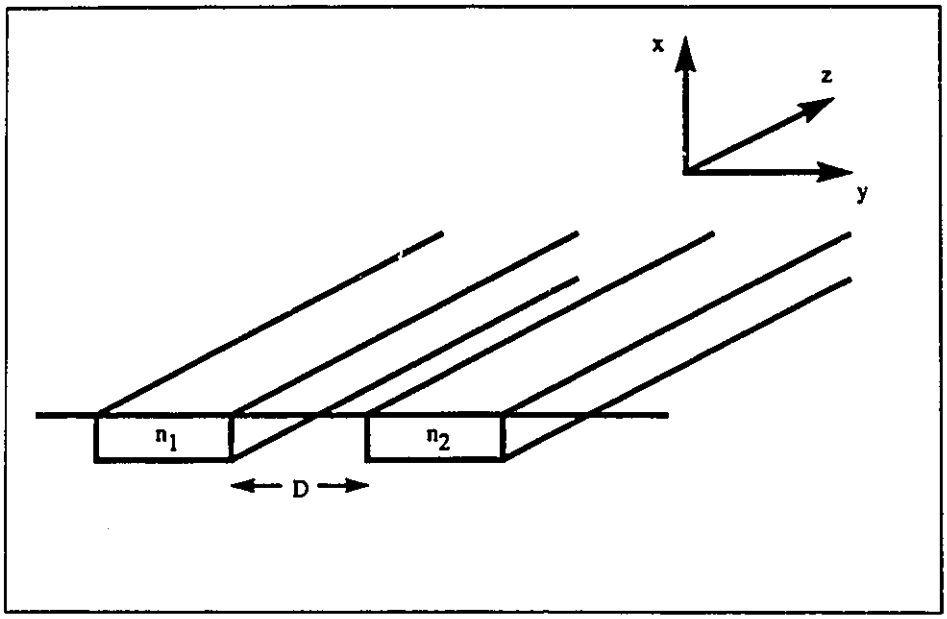

Figure 1.5: The basic geometry for coupling of two waveguide modes.

1.3.8 Coupled-Mode Theory

Coupled mode theory is a general method of calculating the behavior of two waveguides which are parallel to each other and close enough together to affect the guiding behavior. An understanding of coupled waveguides is useful to provide a qualitative understanding of the behavior of X-crossed waveguides. Figure 1.5 shows the basic geometry for understanding coupled mode theory. When the distance between the two waveguides is much greater than the operating wavelength, the modes propagate independently with eigenmode solutions ψ_1 and ψ_2 having a propagation constants β_1 and β_2 respectively.

As the distance between the two waveguides is made smaller, the modes ψ_1 and ψ_2 become coupled and are no longer the eigenmodes of the two-waveguide system. Instead there exists a symmetric mode (ψ_s) and an antisymmetric mode (ψ_a). These modes have propagation constants β_s which is larger than β_1 and β_2 and β_a which is smaller than β_1 and β_2.

If the modes ψ_s and ψ_a are both excited there will be a transfer

of power along the propagation direction between waveguide one and waveguide two due to the beating of ψ_s and ψ_a. If the guides are weakly coupled (i.e. not too close together) $\psi_1+\psi_2$ will resemble ψ_s and $\psi_1-\psi_2$ will resemble ψ_a and the power transfer will make it appear as if the original modes are coupled together leading to the common terminology of coupled mode theory.

A formalism exists [8] [7] which gives an approximate form for ψ_s and ψ_a and the beat length given the unperturbed modes ψ_1 and ψ_2 and the degree of coupling between the waveguides. The modes ψ_1 and ψ_2 are assumed to be of the form:

$$\psi_1(x,y,z,t) = A_1(z)f_1(x,y)e^{i(\omega t-\beta_1 z)} \quad (1.47)$$

$$\psi_2(x,y,z,t) = A_2(z)f_2(x,y)e^{i(\omega t-\beta_2 z)} \quad (1.48)$$

where $f_n(x,y)$ is the field distribution for mode n in the absence of any coupling.

This leads to a pair of coupled differential equations for the z dependence of the modes ψ_1 and ψ_2 in the presence of the perturbation due to the other waveguide.

$$\frac{dA_1(z)}{dz} = -i\kappa_{1,2}A_2(z)e^{-i(\beta_2-\beta_1)z} \quad (1.49)$$

$$\frac{dA_2(z)}{dz} = -i\kappa_{2,1}A_1(z)e^{-i(\beta_1-\beta_2)z}. \quad (1.50)$$

If the perturbation is zero then $A_1(z) \Rightarrow 1$.

The coupling parameters, $\kappa_{1,2}$ and $\kappa_{2,1}$, are measures of the overlap integral between the modes (Figure 1.6), weighted by the perturbation as in the following equation:

$$\kappa_{1,2} = c\int_{pert.} f_1^* \Delta\varepsilon f_2 dxdy. \quad (1.51)$$

The constant c is one if the modes f_1 and f_2 are normalized and the $\Delta\varepsilon$ is the permittivity difference between the two waveguide structure and the single waveguide structure on which the calculation of f_1 is based.

These expressions lead to, when $\beta_1 = \beta_2$, the behavior of $A_1(z)$ and $A_2(z)$ shown in Figure 1.7 Power appears to oscillate between the modes with a coupling length given by

$$L = \frac{\pi}{2\kappa}. \quad (1.52)$$

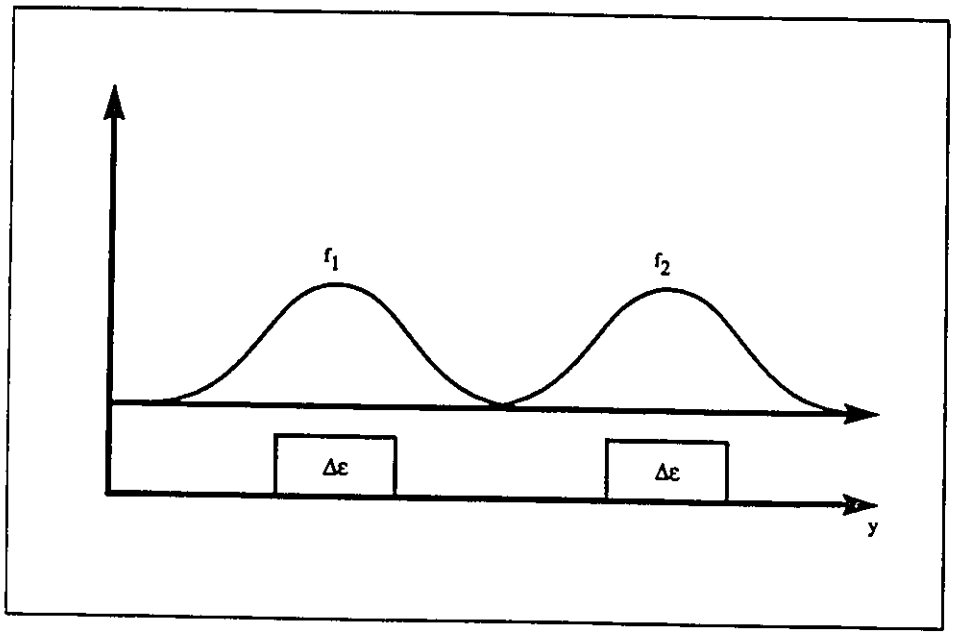

Figure 1.6: The coupling parameters are calculated by weighting the mode overlap integral by the perturbation $\Delta\varepsilon$.

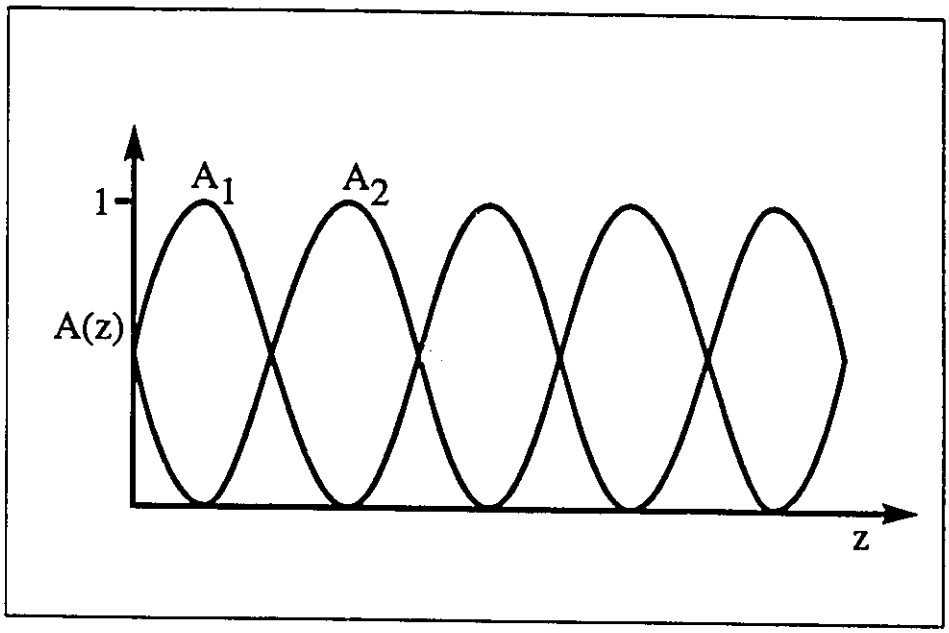

Figure 1.7: The behaviour of the mode amplitudes $A_1(z)$ and $A_2(z)$ for the case of two identical parallel waveguides.

1.4 Fabrication of Waveguide Devices

The fabrication of semiconductor waveguide devices generally consists of the following steps:

1. material growth
2. photolithographic masking
3. reactive ion beam etching
4. metallization
5. dielectric overlayer deposition.

Material growth is used to form electrical and optical structures which are planar in nature. These structures include n and p doped layers of varying band gap and refractive index. The growth direction is perpendicular to the substrate. The growth of these structures is typically accomplished by molecular beam epitaxy (MBE)[9][10] or metal-organic chemical-vapor deposition (MOCVD)[11]. Photolithography is used to define etch and deposition regions in the plane of the substrate.

1.5 Scope of Thesis

This thesis deals with two problems associated with the design of semiconductor waveguide devices. The first of these problems is directly related to the list of processing steps given above. Each of these processes can add mechanical stress. This mechanical stress can lead to unexpected optical and electrical properties. Experimental results in this thesis will show how a weakly confining strip loaded waveguide can have largely perturbed waveguide modes due to stress induced by deposited metal and dielectric overlayers. A method of measuring this stress as well as modeling its effects on waveguide modes will be presented.

The second problem examined in this thesis is that of the design of intersecting waveguides. In OEIC's it is often necessary to have

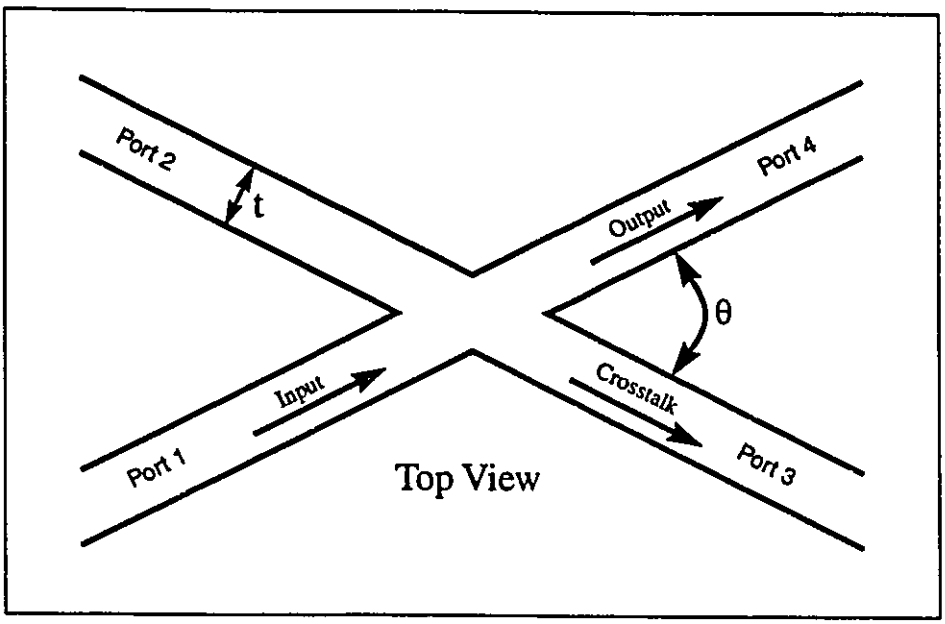

Figure 1.8: A typical X-crossed waveguide structure.

one waveguide cross another with high throughput and low crosstalk. Figure 1.8 shows a typical structure. It is sometimes necessary to use small crossing angles, unfortunately the crosstalk can be large at these angles. This thesis presents general modifications to these crossings which can dramatically improve their low angle performance.

Chapter 2

The Degree of Polarization of Photoluminescence

2.1 Introduction

Stress induced by the processing of InP waveguide structures is of concern to manufacturers of optoelectronic integrated circuits for a variety of reasons. The stress can be a result of oxides and metals [12] [13] [14] [15], the etching of rib waveguides [16], lattice mismatch of epilayers [17] [18] [19], and thermally induced mismatch [20].

With active devices, such as diode lasers, stress causes reduced lifetimes, changes in the threshold current and polarization state of the light output from the laser[21][22]. With both active and passive waveguide devices, the waveguiding properties of the device can be changed due to the refractive index variations produced by the photoelastic effect.

Many techniques are available for the measurement of stress in semiconductor devices. These techniques include: Automatic Bragg Angle Control X-ray diffraction (ABAC) [23], X-ray topography [24], Raman Microprobe spectroscopy [25], photoluminescence spectroscopy [26], electron beam induced current (EBIC) [27], and infrared birefringence [28].

Each of these techniques has problems associated with it that make it less than ideal for semiconductor devices. Raman spectroscopy and

photoluminescence spectroscopy have low stress resolution compared to the degree of polarization of photoluminescence (DOP) which is the subject of this chapter. This is due to having to resolve small changes in large peaks. ABAC techniques are good for measuring stresses due to single overlayers but can not measure the combined stresses due to many overlayers which are not continuous over the wafer surface. Also stresses due to etched structures are beyond the scope of this technique. EBIC requires long measurement times and has not been shown to be a quantitative technique. The other techniques have spatial resolutions above $5\mu m$ which are far from sufficient for the small structures in OEICs.

It has been shown that externally applied stress can be correlated with changes in the polarization state of the laser output [29]. This led to the development of the technique of the degree of polarization of photoluminescence (DOP) [30]. This technique scans the semiconductor under study and locally measures the photoluminescence from the semiconductor. A spatial resolution on the order of $1\mu m$ is possible.

In the case described here, a cleaved end facet of the waveguide is scanned. The geometry is shown in Figure 2.1. The photoluminescence is resolved into two perpendicular polarization states. If the power in each of the two polarizations are denoted by L_x and L_y, where z is the direction of light propagation, the degree of polarization of photoluminescence is defined as

$$\rho = \frac{L_x - L_y}{L_x + L_y}. \tag{2.1}$$

The DOP is shown in Section 2.2 to be related to the stress by

$$\rho = K_\sigma \left(\sigma_{xx} - \sigma_{yy}\right). \tag{2.2}$$

K_σ is an experimentally determined constant with units of inverse stress.

2.2 Theory

The general theory of polarization changes due to stress is presented in this chapter. This chapter is a general overview of the technique. Readers interested in more detail should consult the references, in particular

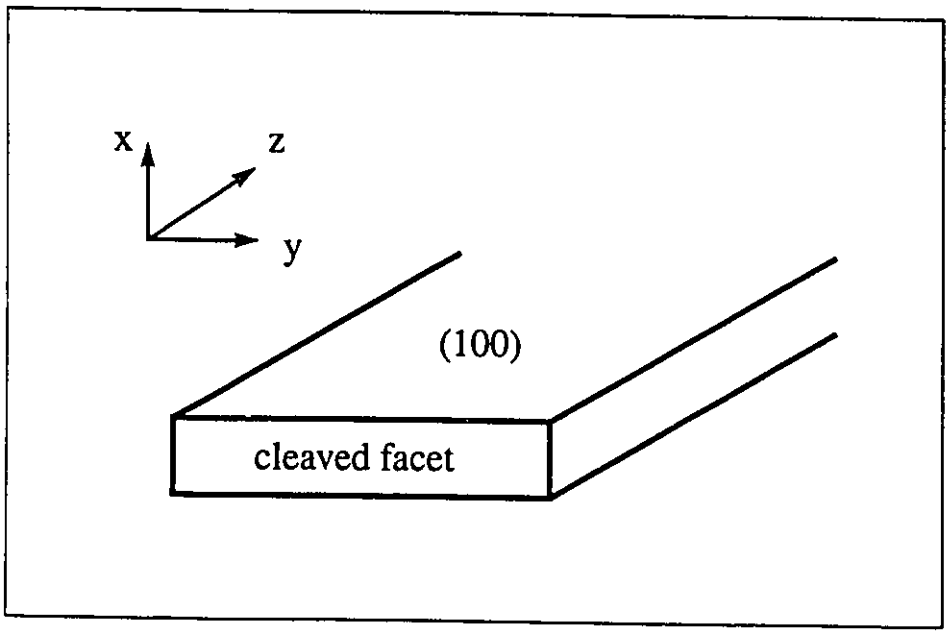

Figure 2.1: The geometry used in describing the technique of the degree of polarization of photoluminescence.

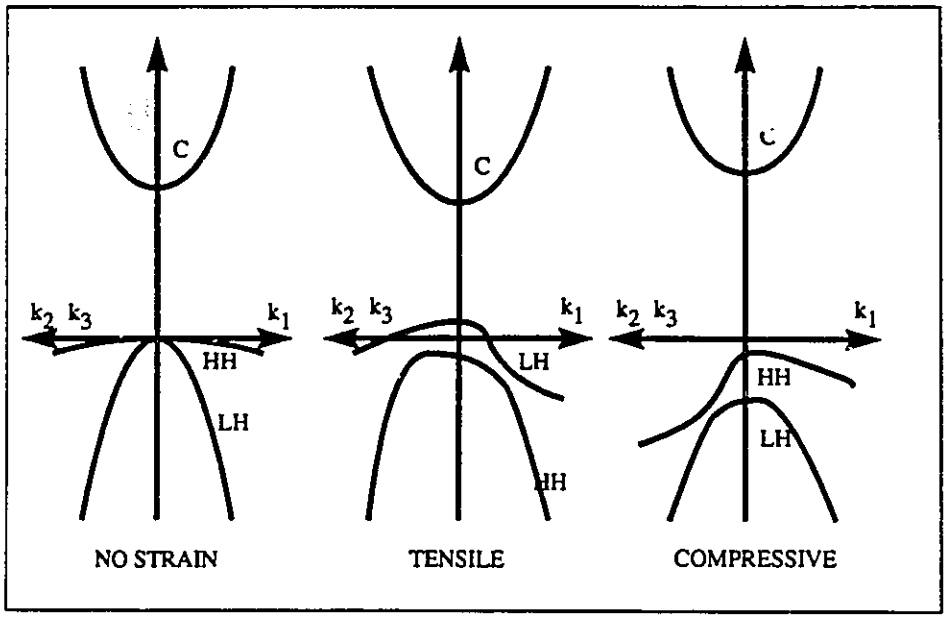

Figure 2.2: The band structure of a III-V semiconductor for various types of stress.

those by Colbourne et al. The theory uses many simplifying assumptions, such as room temperature and stresses below $2x10^9 dyn/cm^2$. Second order effects are ignored. It is well known that the band structure of III-V semiconductors is affected by applied stress. The case to be considered here is a uniaxial stress. The stress induces an anisotropy in the crystal which causes a band splitting between the light hole and heavy hole bands [31] [32]. There is also a band deformation [33].

Figure 2.2 shows the relationship between the conduction, heavy-hole and light-hole bands for the three cases of: a) no stress, b) uniaxial compression, and c) uniaxial tension. This diagram is the basis for understanding the DOP technique.

Pikus and Bir [31] have developed an expression which approximates the energy shifts in the hole bands (+ for heavy hole and - for light hole) as

$$\delta E_h = \pm \frac{3bB}{2B} \sum_i \frac{k_i^2}{k^2} \epsilon_{ii} \tag{2.3}$$

where

$$\overline{B} = \sqrt{B^2 + C^2/5} \tag{2.4}$$

$$k = \sqrt{k_x^2 + k_y^2 + k_z^2}. \tag{2.5}$$

The parameter b is a valence band deformation potential, B and C are valence band edge parameters as in, for example, [34], k is the magnitude of the electron wavevector, and ϵ_{ii} is a component of the strain tensor along its principle axes. The value of i is either x, y, or z. The above expression accounts for only the energy shifts that are directionally dependent. The directionally independent energy shifts have no bearing on the polarization of the photoluminescence.

The optical matrix element for the transition between initial state ψ_i and final state final state ψ_f is given by

$$M = \langle \psi_i | \mathbf{e} \cdot \mathbf{p} | \psi_f \rangle \tag{2.6}$$

where $\mathbf{e}$ is the polarization vector of the photon and $\mathbf{p}$ is the electron momentum operator. The wavefunctions for the states ψ_i and ψ_f can be chosen from the set of wavefunctions for the conduction, heavy-hole, light-hole, and split-off bands (for $\mathbf{k}$ along the z axis) which are given as in [35] by

$$\psi_c = S \tag{2.7}$$

$$\psi_{hh} = (X + iY)/\sqrt{2} \tag{2.8}$$

$$\psi_{lh} = (2Z - (X + iY))/\sqrt{6} \tag{2.9}$$

$$\psi_{so} = -(Z + (X + iY))/\sqrt{3}. \tag{2.10}$$

Since the wavefunctions X,Y and Z have p-orbital symmetry in their respective directions, There are only three non-zero elements of the matrix. These are given as

$$M = \langle X | p_x | S \rangle = \langle Y | p_y | S \rangle = \langle Z | p_z | S \rangle . \tag{2.11}$$

If we neglect the split-off band since it is usually well separated from the light and heavy hole bands, these matrix elements can be simplified

for an electric field at an angle α to $\mathbf{k}$. The elements are given by [36] as

$$|M_{hh}|^2 = \left(\frac{Pm_0}{\hbar}\right)^2 \left(1-\cos^2\alpha\right) \quad (2.12)$$

$$|M_{lh}|^2 = \left(\frac{Pm_0}{\hbar}\right)^2 \left(\frac{1}{3}+\cos^2\alpha\right) \quad (2.13)$$

where α is the angle between the electron momentum vector $\mathbf{k}$ and the electric field vector $\mathbf{e}$.

Integrating the interaction probability for a single electron over the entire electron population yields

$$L = \int |M|^2(\theta,\phi) f_e(E_e(k)) f_h(E_h(k)+\delta E(\theta,\phi)) k^2 \sin\phi dk d\theta d\phi \quad (2.14)$$

where f_e and f_h are the electron and hole Fermi functions. δE is the strain dependent energy shift as given in equation 2.3.

The above integral can be simplified by expanding the hole Fermi function to two terms [30]. The integral becomes

$$L = G\int |M'|^2(\theta,\phi)\left(1+\frac{\delta E_h(\theta,\phi)}{kT}\right) d\Omega \quad (2.15)$$

where

$$G = \frac{P^2 m_0^2}{h^2}\int f_e(E_e(k)) f_h(E_h(k)) k^2 dk \quad (2.16)$$

and $d\Omega$ is the incremental solid angle element.

These expressions are given for strain parallel to the polarization direction as

$$L_{hh\parallel} = G_{hh}\int \left(1-\cos^2\alpha\right)\left(1+\frac{3bB\epsilon}{2\overline{B}kT}\cos^2\alpha\right) d\Omega \quad (2.17)$$

$$L_{lh\parallel} = G_{lh}\int \left(\frac{1}{3}+\cos^2\alpha\right)\left(1-\frac{3bB\epsilon}{2\overline{B}kT}\cos^2\alpha\right) d\Omega \quad (2.18)$$

and for strain perpendicular to the polarization direction as

$$L_{hh\perp} = G_{hh}\int \left(1-\cos^2\alpha\right)\left(1+\frac{3bB\epsilon}{2\overline{B}kT}\cos^2\beta\right) d\Omega \quad (2.19)$$

$$L_{lh\perp} = G_{lh}\int \left(\frac{1}{3}+\cos^2\alpha\right)\left(1-\frac{3bB\epsilon}{2\overline{B}kT}\cos^2\beta\right) d\Omega. \quad (2.20)$$

α and β are given as in [30] by

The degree of polarization is given by the expression

$$\rho = \frac{L_x - L_y}{L_x + L_y} = \frac{L_\parallel - L_\perp}{L_\parallel + L_\perp} \tag{2.21}$$

where

$$L_\parallel = L_{hh\parallel} + L_{lh\parallel} \tag{2.22}$$

$$L_\perp = L_{hh\perp} + L_{lh\perp}. \tag{2.23}$$

Substituting in from above gives

$$L_\parallel - L_\perp = -\frac{4\pi b B \epsilon_{xx}}{5\overline{B}kT}(G_{hh} + G_{lh}) \tag{2.24}$$

$$L_\parallel + L_\perp = \frac{16\pi}{3}(G_{hh} + G_{lh}) \tag{2.25}$$

which leads to

$$\rho = -\frac{3bB}{20\overline{B}kT}(\epsilon_{xx} - \epsilon_{yy}) \tag{2.26}$$

for an arbitrary strain in the x and y directions.

Using Young's modulus E_{el} and Poisson's ratio ν, the above expression can be converted to an expression in terms of stress instead of strain, giving

$$\begin{aligned} \rho &= -\frac{3bB(1+\nu)}{20E_{el}\overline{B}kT}(\sigma_{xx} - \sigma_{yy}) \\ &= K_\sigma(\sigma_{xx} - \sigma_{yy}). \end{aligned} \tag{2.27}$$

It is important to note that in InP the electron-photon interaction is dependent on the crystallographic orientation of the stress. However, this anisotropy is small [37] and isotropy is assumed in this thesis. Colbourne et al. [38] have experimentally determined a value of K_σ of $-9.4x10^{-11}\text{cm}^2/\text{dyn}$ for n-type InP along a (100) facet.

Chapter 3

The Beam Propagation Method

3.1 Introduction

The beam propagation method (BPM) was developed in the late 1970's [39]. It allows the calculation of optical fields in circumstances where the index profile changes in the propagation direction and includes high order and radiation mode effects. It consists of developing a relationship between the optical fields in two axially separated planes and applying this consecutively until the beam has propagated through the structure. The BPM method is simple in implementation and extremely versatile. These characteristics have made it an extremely widely used method in optoelectronic and fibre-optic design. The basis of the method will be discussed in this chapter.

3.2 The Starting Points of BPM

The basis of all BPM methods is the scalar Helmholtz equation. It is derived directly from Maxwell's Equations. They are given by the following four equations: Faraday's Law:

$$\nabla \times \mathbf{E} = -\frac{\partial}{\partial t}\mu_0 \mathbf{H} - \frac{\partial}{\partial t}\mu_0 \mathbf{M} \tag{3.1}$$

Ampere's Law:

$$\nabla \times \mathbf{H} = \frac{\partial}{\partial t}\varepsilon_0 \mathbf{E} + \frac{\partial \mathbf{P}}{\partial t} + \mathbf{J} \tag{3.2}$$

Gauss's Laws:

$$\nabla \cdot \varepsilon_0 \mathbf{E} = -\nabla \cdot \mathbf{P} + \rho \tag{3.3}$$

$$\nabla \cdot \mu_0 \mathbf{H} = -\nabla \cdot \mu_0 \mathbf{M}. \tag{3.4}$$

In linear, isotropic and dispersion free media the following two constitutive relations hold.

$$\mathbf{P} = \varepsilon_0 \chi_e \mathbf{E} \tag{3.5}$$

$$\mathbf{M} = \chi_m \mathbf{H} \tag{3.6}$$

Equations 3.1 and 3.2 can then be written

$$\nabla \times \mathbf{E} = -\mu \frac{\partial \mathbf{H}}{\partial t} \tag{3.7}$$

$$\nabla \times \mathbf{H} = \varepsilon \frac{\partial \mathbf{E}}{\partial t} + \mathbf{J} \tag{3.8}$$

also equations 3.3 and 3.4 become

$$\nabla \cdot \varepsilon \mathbf{E} = \rho \tag{3.9}$$

and

$$\nabla \cdot \mu \mathbf{H} = 0 \tag{3.10}$$

where

$$\varepsilon = \varepsilon_0 (1 + \chi_e) \tag{3.11}$$

and

$$\mu = \mu_0 (1 + \chi_m). \tag{3.12}$$

3.3 The Vector Wave Equation

If the medium is source free and we take the curl of 3.7 and substitute in 3.8 we obtain

$$\nabla \times (\nabla \times \mathbf{E}) = -\mu\varepsilon \frac{\partial^2 \mathbf{E}}{\partial t^2} \tag{3.13}$$

The following identity is true if a vector $\mathbf{V}$ is twice differentiable.

$$\nabla \times (\nabla \times \mathbf{V}) = \nabla (\nabla \cdot \mathbf{V}) - \nabla^2 \mathbf{V} \tag{3.14}$$

This allows us to write equation 3.13 as

$$\nabla (\nabla \cdot \mathbf{E}) - \nabla^2 \mathbf{E} = -\mu\varepsilon \frac{\partial^2 \mathbf{E}}{\partial t^2}. \tag{3.15}$$

We can expand the first term in 3.15 as

$$\nabla (\nabla \cdot \mathbf{E}) = -\nabla \left(\frac{1}{\varepsilon} \nabla\varepsilon \cdot \mathbf{E} \right). \tag{3.16}$$

giving

$$\nabla^2 \mathbf{E} + \nabla \left(\frac{1}{\varepsilon} \nabla\varepsilon \cdot \mathbf{E} \right) = \frac{\partial^2}{\partial t^2} (\mu_0 \varepsilon \mathbf{E}). \tag{3.17}$$

Similarly for the magnetic field we can take the curl of equation 3.8 and substitute in equation 3.7 to obtain

$$\nabla^2 \mathbf{H} = \varepsilon\mu_0 \frac{\partial^2}{\partial t^2} \mathbf{H} + (\nabla \times \mathbf{H}) \times \frac{\nabla\varepsilon}{\varepsilon}. \tag{3.18}$$

We can define

$$\nabla_T^2 = \frac{\partial^2}{\partial x^2} + \frac{\partial^2}{\partial y^2}. \tag{3.19}$$

For modal fields of the form

$$\mathbf{E} = \mathbf{E}_{m,l}(x,y) e^{i(\omega t - \beta_{m,l} z)} \tag{3.20}$$

$$\mathbf{H} = \mathbf{H}_{m,l}(x,y) e^{i(\omega t - \beta_{m,l} z)} \tag{3.21}$$

The above equations reduce to the vector form of the wave equations:

$$\left(\nabla_T^2 - \beta_{m,l}^2 + k_0^2 n^2\right) \mathbf{E}_{m,l} + e^{i\beta_{m,l} z} \nabla \left(\frac{\nabla n^2 \cdot \mathbf{E}_{m,l} e^{-i\beta_{m,l} z}}{n^2} \right) = 0 \tag{3.22}$$

$$\left(\nabla_T^2 - \beta_{m,l}^2 + k_0^2 n^2\right) \mathbf{H}_{m,l} - e^{i\beta_{m,l} z} \left(\nabla \times \left(\mathbf{H}_{m,l} e^{-i\beta_{m,l} z} \right) \right) \times \frac{\nabla n^2}{n^2} = 0. \tag{3.23}$$

where $k_0^2 = \omega^2 \mu_0 \varepsilon_0$ and $n^2 = \varepsilon/\varepsilon_0$ have been used for simplicity.

3.4 The Scalar Wave Equation

If $\nabla n^2 << n^2$, equations 3.22 and 3.23 reduce to the scalar wave equations

$$\left(\nabla^2 - \mu_0\varepsilon\frac{\partial^2}{\partial t^2}\right)\mathbf{E} = 0 \tag{3.24}$$

$$\left(\nabla^2 - \mu_0\varepsilon\frac{\partial^2}{\partial t^2}\right)\mathbf{H} = 0 \tag{3.25}$$

If the fields for any mode m and polarization l are of the form

$$\mathbf{E}(x,y,z,t) = \mathbf{E}_{m,l}(x,y)e^{-i(\beta_{m,l}z-\omega t)} \tag{3.26}$$

$$\mathbf{H}(x,y,z,t) = \mathbf{H}_{m,l}(x,y)e^{-i(\beta_{m,l}z-\omega t)} \tag{3.27}$$

then the scalar wave equations become

$$\left(\nabla_T^2 - \beta_{m,l}^2 + k_0^2 n^2\right)\mathbf{E}_{m,l}(x,y) = 0 \tag{3.28}$$

$$\left(\nabla_T^2 - \beta_{m,l}^2 + k_0^2 n^2\right)\mathbf{H}_{m,l}(x,y) = 0 \tag{3.29}$$

3.5 The Paraxial Approximation

The solution of these equations is more easily formulated in a solution suitable for numerical methods using this approximation[40]. If we write $n = n_0 + \delta n$ where n_0 is a constant and that the propagation vector is directed close to the waveguide axis $\left(k_z \approx k - \frac{k_x^2+k_y^2}{2k}\right)$. Writing the fields in terms of the normalized index gives

$$\mathbf{E}'(x,y,z,t) = \mathbf{E}(x,y,z)e^{i(\omega t - k_0 n_0 z)} \tag{3.30}$$

where $\mathbf{E}'$ is the normal time dependent electric field vector and $\mathbf{E}$ is a modified time independent electric field vector. Writing the field in terms of the normalized index n_0 is an essential step for BPM calculations. It allows the fields to be written in a way in which they vary slowly with respect to z. Without this step, the calculations would require many more calculation steps in every micron of propagation making the calculation prohibitively long.

Calculating the second derivative with respect to z of $\mathbf{E}'$ gives

$$\frac{\partial^2 \mathbf{E}'}{\partial z^2} = \frac{\partial}{\partial z}\left(\frac{\partial \mathbf{E}}{\partial z} e^{i(\omega t - k_0 n_0 z)} - i k_0 n_0 \mathbf{E} e^{i(\omega t - k_0 n_0 z)}\right) \quad (3.31)$$

$$= \left(\frac{\partial^2 \mathbf{E}}{\partial z^2} - 2ik_0 n_0 \frac{\partial \mathbf{E}}{\partial z} - k_0^2 n_0^2 \mathbf{E}\right) e^{i(\omega t - k_0 n_0 z)}. \quad (3.32)$$

Since $\mathbf{E}$ varies slowly with z, one can neglect the second derivative with respect to z. This is the paraxial approximation and leads to the following wave equation, sometimes known as the Fresnel Equation:

$$\left(\nabla_T^2 + \frac{\partial^2}{\partial z} + k_0^2 n^2\right) \mathbf{E} = 0 \quad (3.33)$$

$$2ik_0 n_0 \frac{\partial \mathbf{E}}{\partial z} = \left(\left(n^2 - n_0^2\right) k_0^2 + \nabla_T^2\right) \mathbf{E}. \quad (3.34)$$

The parallel equation for the magnetic field ($\mathbf{H}$) also exists.

3.6 The Effective Index Method

The effective index method allows the simplification of a two dimensional waveguide problem into a one waveguide dimensional problem. It is useful when strong confinement exists in one direction and weak confinement in the other. Figure 3.1 shows a geometry for which the effective index method works well. The y direction exhibits good confinement while the rib provides weak confinement in the x direction.

A solution of this geometry is first attempted by assuming a solution in the x and y directions of the form

$$\mathbf{E}(x, y, z) = \frac{\mathbf{E}}{|\mathbf{E}|} Y(x, y) X(x) e^{i\beta z}. \quad (3.35)$$

Solving the following wave equation for each unique value of x leads to two values of β_{eff}.

$$\frac{\partial^2 Y}{\partial y^2} + \left(n^2(x, y) k_0^2 - \beta_{eff}^2(x)\right) Y = 0 \quad (3.36)$$

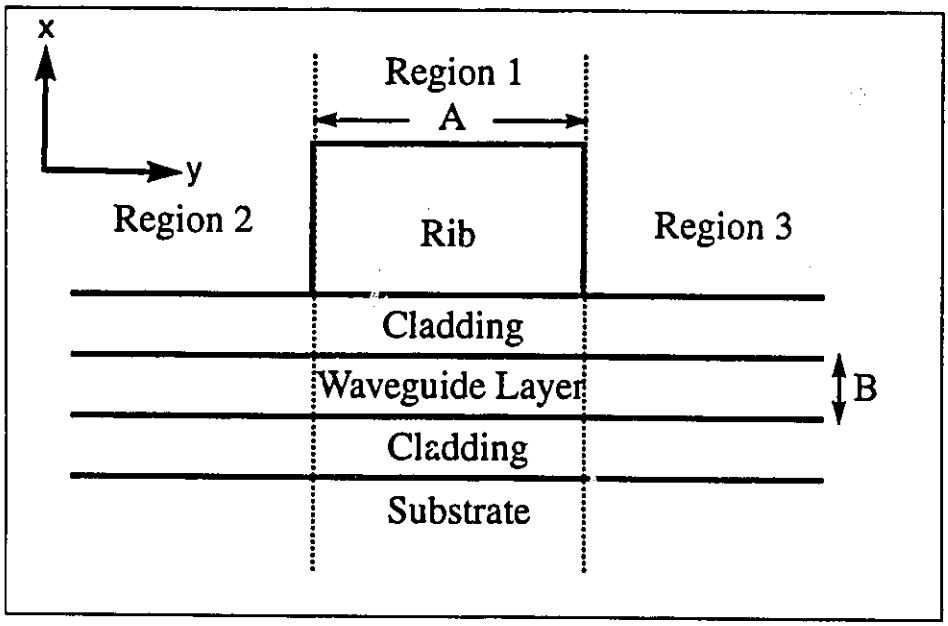

Figure 3.1: The geometry for which the effective index method is a good approximation. The x direction exhibits strong confinement while the strip loading of the rib provides relatively weak confinement in the y direction ($A \gg B$).

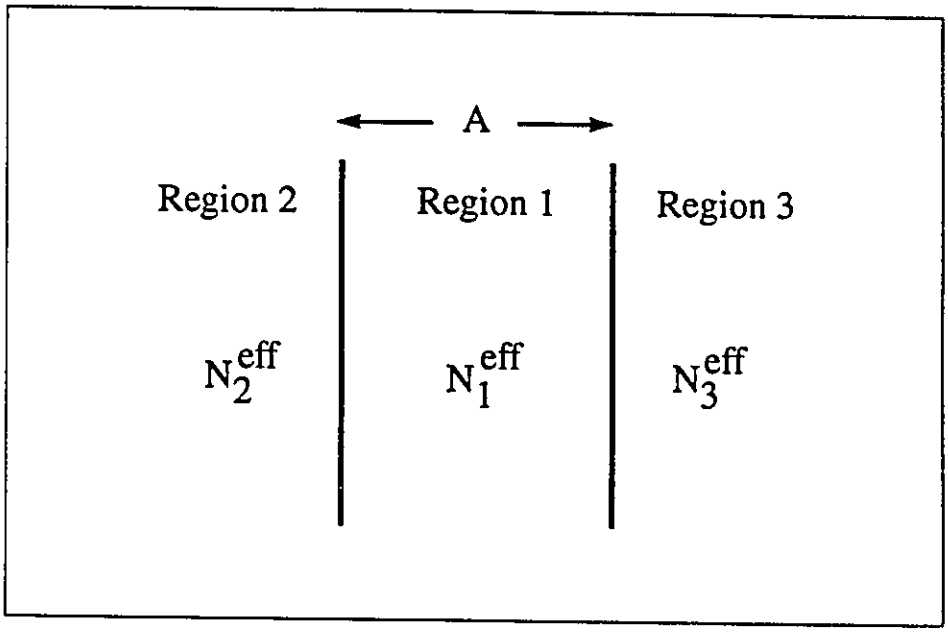

Figure 3.2: The transformed two dimensional problem. The effective indices now define a new one dimensional problem.

These β_{eff}'s then determine a new problem shown in Figure 3.2 in which the refractive indices are given by

$$n_{eff}^{L} \equiv \frac{\beta_{eff}^{L}}{k_0} \tag{3.37}$$

The wave equation to be solved now becomes

$$\frac{d^2X}{dx^2} + \left(\beta_{eff}^2(x) - \beta^2\right) X = 0. \tag{3.38}$$

The above is a good approximation since the cross terms of $\nabla_T^2 \mathrm{E}$ are neglected as

$$2\frac{\partial X}{\partial x}\frac{\partial Y}{\partial x} + X\frac{\partial^2 Y}{\partial x^2} << Y\frac{\partial^2 X}{\partial x^2} + X\frac{\partial^2 Y}{\partial y^2}. \tag{3.39}$$

3.7 Numerical Implementation

The numerical propagation of the field through a structure depends on developing a recursion relation between the fields $\Phi(z)$ and $\Phi(z+dz)$. Rewriting the wave equation in terms of the generic field Φ gives

$$\frac{\partial \Phi}{\partial z} = \frac{1}{2ik_0 n_0}\left(k_0^2\left(n^2 - n_0^2\right) + \nabla_T^2\right)\Phi \tag{3.40}$$

Integrating the above allows a recursive solution for Φ.

$$\Phi(x,y,z+\Delta z) = e^{\frac{-i\Delta z}{2k_0 n_0}\nabla_T^2} e^{\frac{-ik_0 n_0}{2}\int_z^{z+\Delta z}\left(\frac{n^2(x,y,z')}{n_0^2}-1\right)dz'} \Phi(x,y,z) \tag{3.41}$$

It has been shown that the accuracy may be increased by splitting the operator [41] in Equation 3.40. The above equation becomes

$$\Phi(x,y,z+\Delta z) = e^{\frac{-i\Delta z}{4k_0 n_0}\nabla_T^2} e^{\frac{-ik_0 n_0}{2}\int_z^{z+\Delta z}\left(\frac{n^2(x,y,z')}{n_0^2}-1\right)dz'} e^{\frac{-i\Delta z}{4k_0 n_0}\nabla_T^2} \Phi(x,y,z) \tag{3.42}$$

The above expression consists of three operators. The first and the last operators each represent propagation through a homogeneous medium over a distance of $dz/2$. The middle term represents the phase correction due to the refractive index variation. It may be referred to as a phase lens term.

3.8 The Finite Difference BPM

The finite difference beam propagation method (FDBPM) was invented in the late 1980's[42][41] and takes its name from the use of a finite difference approximation to the ∇^2 operator. It consists of applying the three operators discussed in Section 3.7 one after another. The free space operators are approximated by a rational function (Padé) approximation given by

$$e^{\frac{-i\Delta z}{4k_0 n_0}\nabla_T^2} \approx \frac{1 - \frac{i\Delta z}{8k_0 n_0}\nabla_T^2}{1 + \frac{i\Delta z}{8k_0 n_0}\nabla_T^2} \tag{3.43}$$

Evaluation of Equation 3.43 consists of tridiagonal matrix multiplication and matrix inversion. The algorithm is generally less accurate than other methods, such as the fast Fourier transform beam propagation method (FFTBPM)[42] but is much faster.

Much effort has been spent in trying to increase the allowable step size of the FFTBPM in order to increase efficiency. It has been found that multiplying the numerator and denominator of Equation 3.43 by the factor F, where

$$F = \frac{-i\Delta z k_0 (n^2 - n_0^2)}{16 n_0}, \tag{3.44}$$

allows the step size to be increased to as much as 0.2μm depending on the structure.

3.9 The Imaginary Distance BPM

The imaginary distance beam propagation method is used to calculate the eigenmodes and propagation constants of a waveguide structure[43]. The method works by substituting iz for z. The input field at $z = 0$ may be thought of as a linear combination of the waveguide eigenmodes and the radiation modes. The lowest order waveguide mode will have the largest propagation constant. As the field propagates, the individual modes which make up the field will grow by $e^{\beta_m z}$ where m is a mode index. The lowest order mode grows the fastest since it has the largest

propagation constant. If the field is normalized periodically, after a suitable propagation distance the field will approximate the lowest order mode and the propagation constant can be evaluated by examining the ratio of the modal power before and after a fixed step.

The method is extremely fast compared with other methods[44] but if modes other than the fundamental are required, other methods can be more efficient since their calculation using the imaginary distance BPM requires the calculation of all modes of lower order and subtracting these modes from the propagating field.

Chapter 4

Experimental Determination of Metallization Stress

4.1 Introduction

When it is desirable to employ weakly guiding ($\frac{\Delta n}{n} < 0.5\%$) optical waveguides in the presence of metal or dielectric overlayers the guiding properties can be significantly altered by the stress induced by these overlayers. Possible sources of this stress have been discussed in 2.1.

In this chapter a weakly guiding InP based waveguide with a metal overlayer is examined. The waveguide consists of InP cladding layers on either side of an InGaAsP guiding layer containing quantum wells (Figure 4.1). The lateral confinement is achieved by etching a rib in the cladding layer to create a strip loaded waveguide. The lateral effective index step is approximately 0.005 and the rib width is 5μm. In the absence of stress-induced refractive index perturbations this would result in a single lateral mode. The metallization is evaporated Ti/Pt/Au (250Å/500Å/2000Å) annealed in a rapid thermal annealer at 420°C for 30s. A 3000Å spun on SiO_2 layer completes the structure.

Experimental results showing the effect and magnitude of the stress for TE guiding are presented followed by a model that confirms the experimental results using beam propagation waveguide modeling.

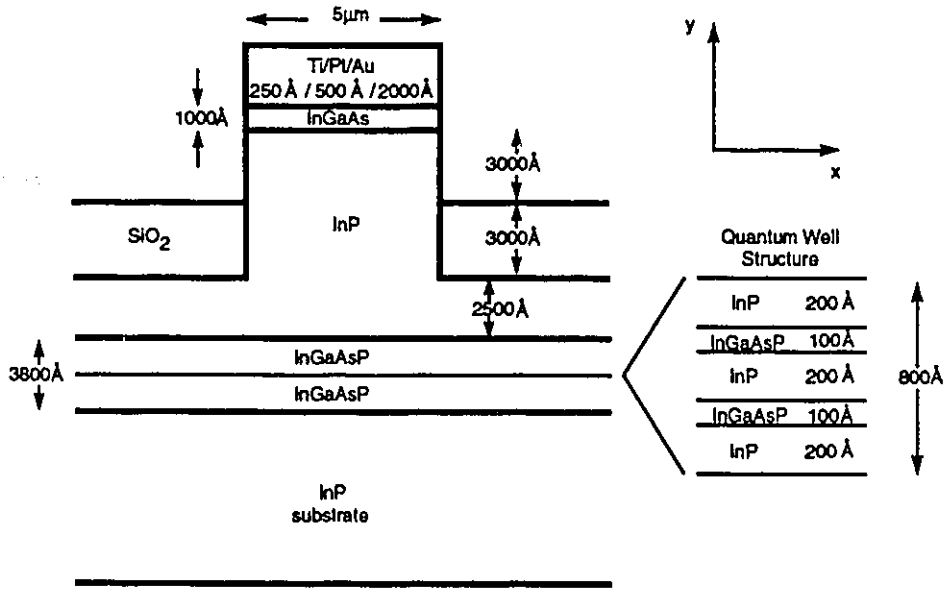

Figure 4.1: The waveguide structure. The wavelengths of the room temperature photoluminescence peaks of the quantum wells and the waveguiding quaternary layer are 1.38μm and 1.21μm respectively.

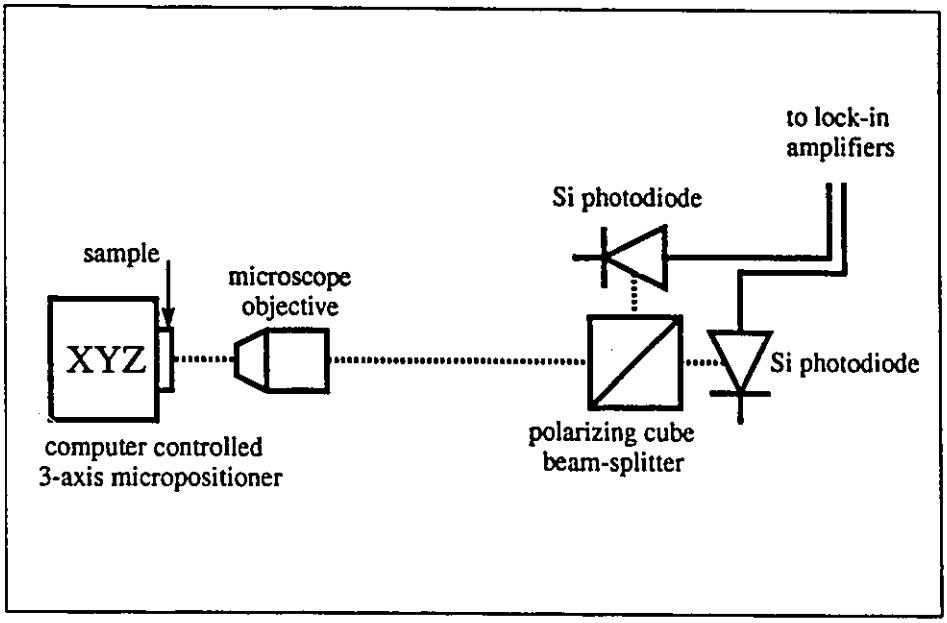

Figure 4.2: The experimental apparatus for measuring the mode profiles.

4.2 Experiment

The metal was deposited in a series of isolated contacts along the length of the waveguide. When one contact was forward biased, electroluminescence produced TE mode light at 1.38 μm that propagated along the passive unbiased sections of the waveguide. The output from the cleaved end facet was scanned in order to plot the near field pattern of the waveguide mode. In separate experiments longer wavelength ($\lambda = 1.55\mu$m) light from an external laser was fiber coupled into the waveguide at one end facet and the profile of the output at the other end was scanned. The samples were typically 3 mm long. The experimental apparatus for these experiments is shown in Figure 4.2.

Output light from the waveguide was collected with a spatial resolution near the diffraction limit using a 20x microscope objective. A computer controlled translation stage was used to raster the sample facet in front of the imaging system to produce a two-dimensional map of the TE polarized waveguide mode. The results of the electrolu-

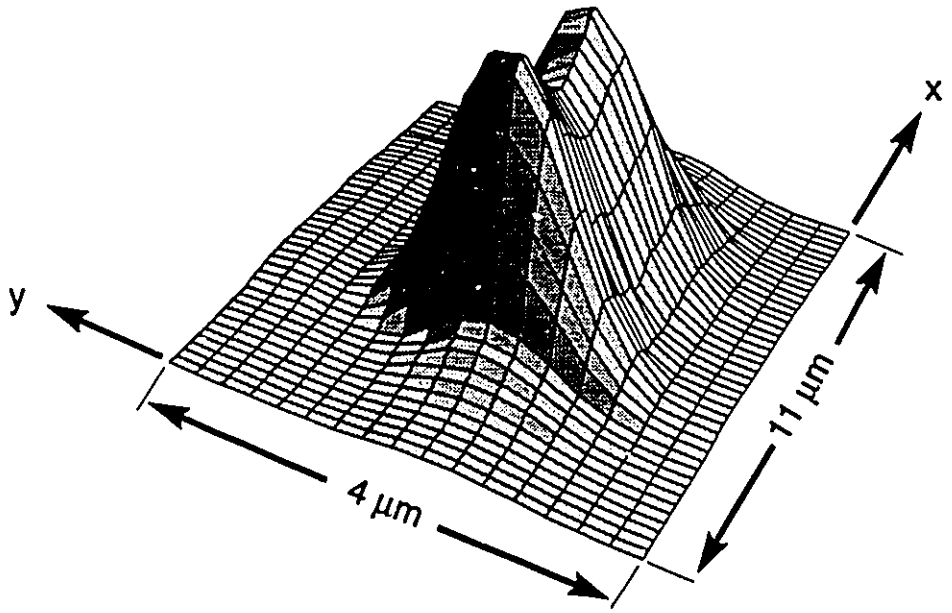

Figure 4.3: The near-field output of the waveguide with metal and dielectric overlayers.

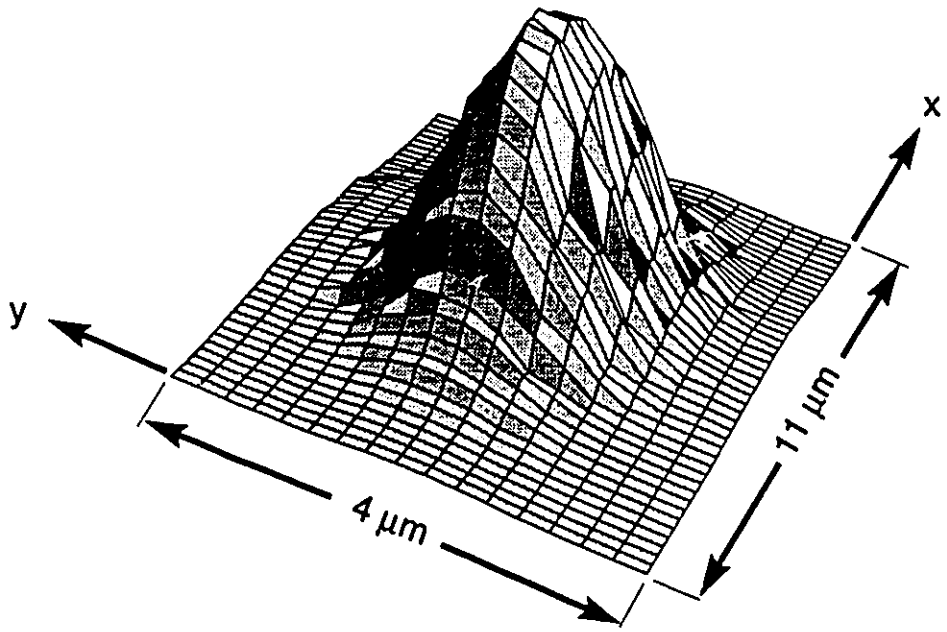

Figure 4.4: The near-field output of the waveguide in the absence of metal and dielectric overlayers.

minescence experiment (Figure 4.3) show a doubly peaked waveguide mode profile across the rib. The peaking is attributed to the stress in the guiding layer caused by the contact metal. Very similar patterns were also observed with light fiber coupled into the waveguide from an external source at 1.4μm and 1.55μm.

In order to establish the origin of the two field maxima the metal and dielectric layers were removed and the near-field pattern was again measured. Figure 4.4 shows that the waveguide mode then displays a single maximum in accordance with the absence of the overlayer-induced stress.

The waveguide mode in Figure 4.3 has a FWHM (in the x direction) of 5μm with the peaks approximately corresponding with the rib edges. Figure 4.4 has a FWHM of 4μm and the peak intensity occurs at the rib centre. The stress-induced modification has the effect of placing a larger fraction of the optical power outside of the expected waveguide mode. This is further illustrated by performing an overlap integral with the data in Figures 4.3 and 4.4. The mode in Figure 4.3 has approximately 16% of its power displaced to the outside of the unstressed mode shown in Figure 4.4.

The stress was measured with a spatial and polarization resolved photoluminescence technique as discussed in Chapter 2 [29][45]. The photoluminescence (PL) from an unstressed crystal of InP will not have a preferred polarization. Once stress is applied, the stress causes the PL to have unequal intensities in the two orthogonal polarizations. By resolving these polarizations one can infer the magnitude of the stress in the InP. Note that the PL from the quantum wells is polarized even in the absence of stress but this experiment is sensitive only to the wavelengths of the PL in the InP substrate.

This is accomplished experimentally (Figure 4.5) by focusing a 632.8 nm HeNe laser on the sample and collecting the PL at a wavelength of 920 nm with the focusing optics. The reflected HeNe light is filtered from the beam using a cold mirror and a beamsplitting polarizer cube allows the two polarizations to be resolved. The sample is rastered under the imaging optics. This technique has a spatial resolution of approximately 1μm. The detectors are calibrated by scanning a piece of unstressed InP.

The degree of polarization (DOP,ρ) is defined as follows in terms of

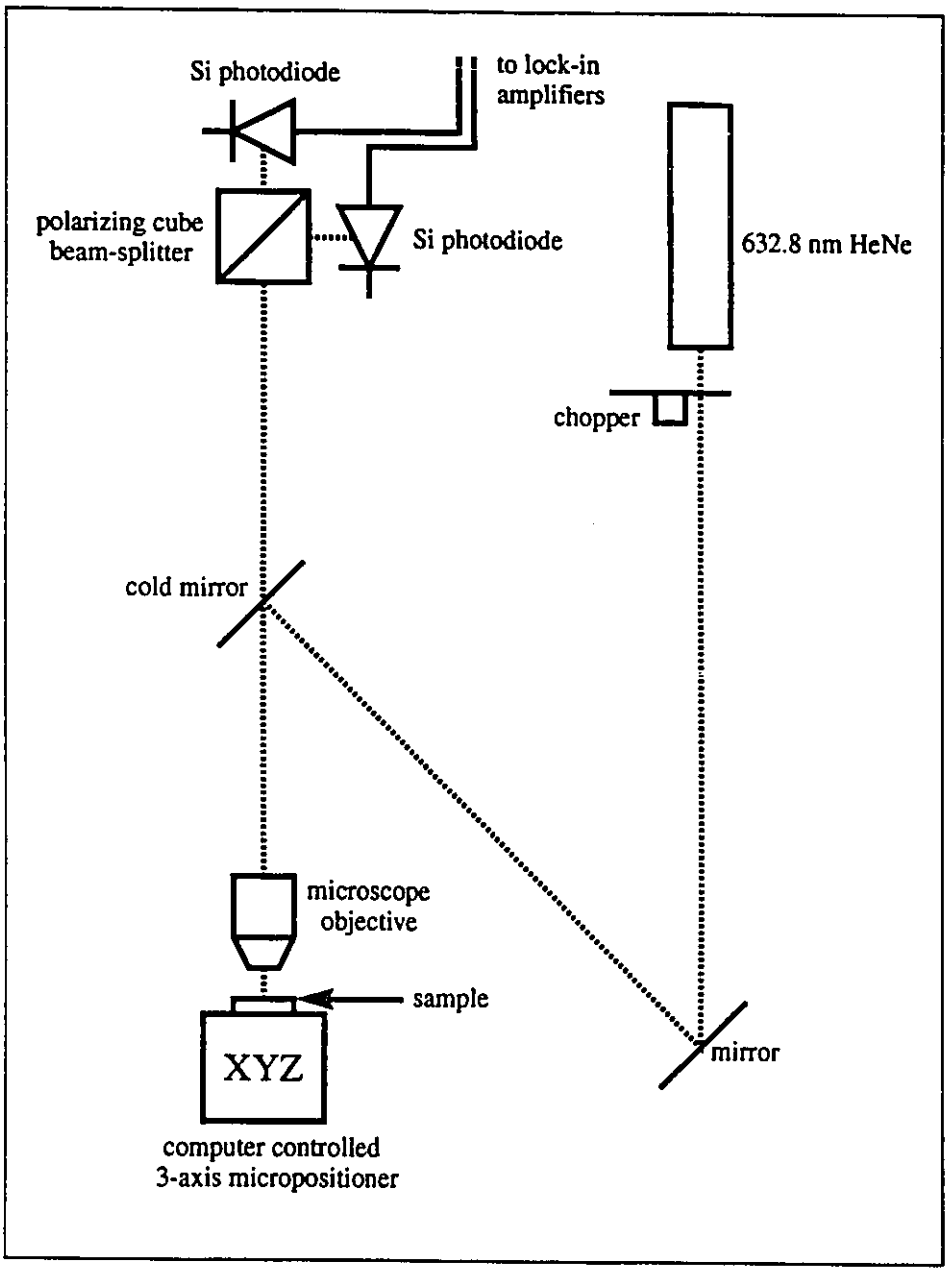

Figure 4.5: The experimental apparatus used for measuring the DOP.

the power in each of the TE (L_x) and TM (L_y) modes:

$$\rho = \frac{(L_x - L_y)}{(L_x + L_y)}. \tag{4.1}$$

The DOP has been shown to be proportional to the difference in the tensile stress in the x and y directions ($\sigma_{xx} - \sigma_{yy}$) with a proportionality constant of $-9.4\text{x}10^{-11}$ for n-type InP along a (110) facet [38].

A cleaved edge perpendicular to the waveguides was scanned with the photoluminescence technique. The results are shown in Figure 4.6. The pattern clearly shows the stress maxima located near the edges of the rib with a relatively large DOP of approximately 2%. It is important to note that the pattern shown is for the InP below the waveguide. The experiment is not sensitive to the luminescence from the quantum wells which is more difficult to interpret due to their polarization properties.

4.3 Modeling

This structure can be approximately modeled by the geometry in Figure 4.7 The stress is modeled as a line stress (S dyn/cm) along each edge of the metallization on an isotropic medium given by [46]

$$\sigma_{xx} = \frac{2S}{y\pi}\left(\cos^3\left[\arctan\left[y/x\right]\right]\sin\left[\arctan\left[y/x\right]\right]\right) \tag{4.2}$$

$$\sigma_{yy} = \frac{2S}{y\pi}\left(\cos\left[\arctan\left[y/x\right]\right]\sin^3\left[\arctan\left[y/x\right]\right]\right). \tag{4.3}$$

The elastic constants for InP are [47]

$$\begin{aligned} C_{11} &= 10.22\text{x}10^{11}\ \text{dyn/cm}^2 \\ C_{12} &= 5.73\text{x}10^{11}\ \text{dyn/cm}^2 \\ C_{44} &= 4.42\text{x}10^{11}\ \text{dyn/cm}^2. \end{aligned} \tag{4.4}$$

Further the relationship between stress and strain is

$$\sigma_{xx} = (\lambda + 2\mu)e_{xx} + \lambda e_{yy} \tag{4.5}$$

$$\sigma_{yy} = \lambda e_{xx} + (\lambda + 2\mu)e_{yy} \tag{4.6}$$

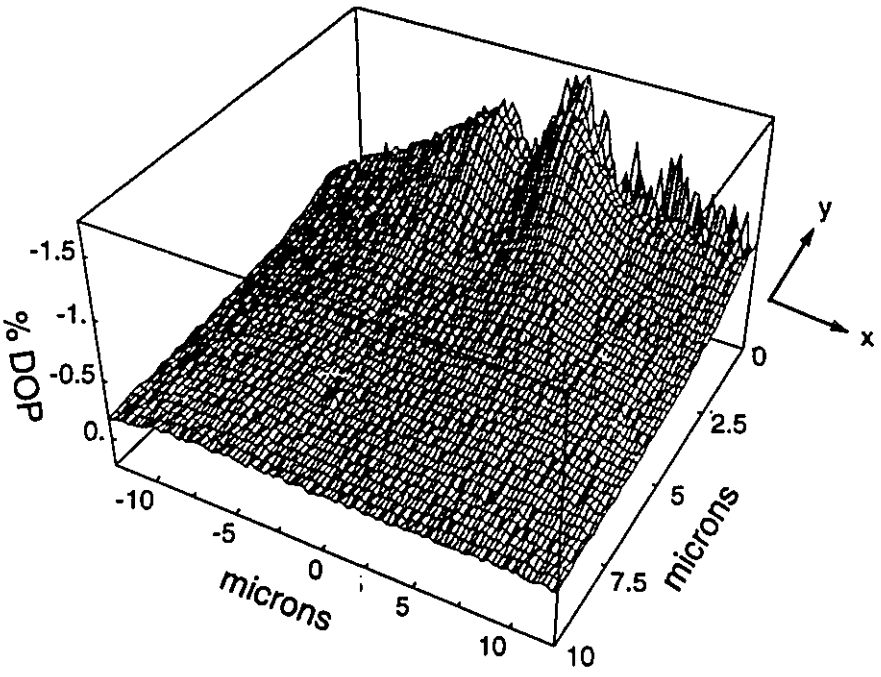

Figure 4.6: The degree of polarization pattern as measured by polarization resolved photoluminescence. The rib is centred at x=0 and the metal semiconductor interface is at $y = -4\mu$m.

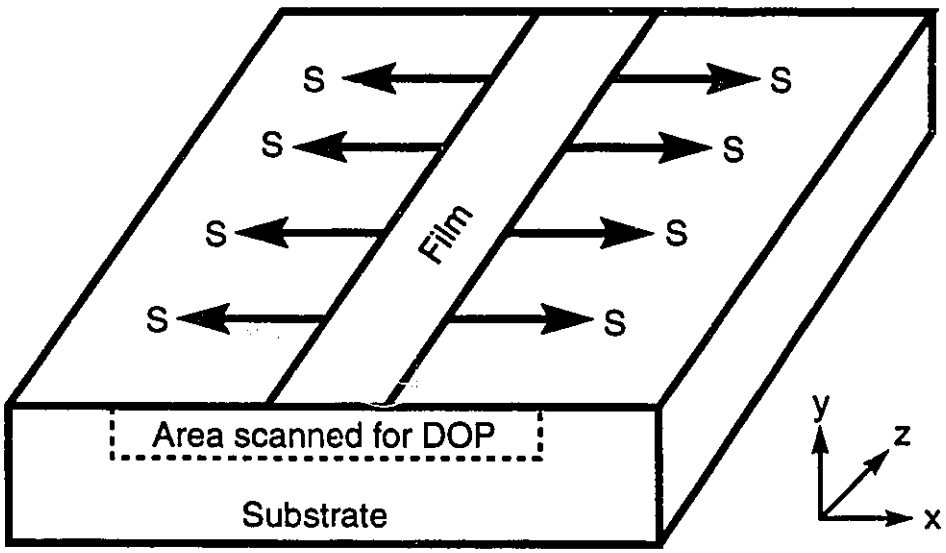

Figure 4.7: The geometry used to model the stress. Each edge of the metal is modeled as a uniformly distributed line stress on an isotropic medium.

in which

$$\lambda = 4.86\text{x}10^{11}\ \text{dyn/cm}^2 \tag{4.7}$$

$$\mu = 3.55\text{x}10^{11}\ \text{dyn/cm}^2 \tag{4.8}$$

are the Lamé constant and shear modulus which were calculated as in [48] using Equation 4.4.

The permittivity change for each polarization is

$$\Delta\epsilon_{TE} = -\epsilon^2\{e_{xx}\left[\frac{1}{2}(p_{11}+p_{12})+p_{44}\right]+e_{yy}p_{12}\} \tag{4.9}$$

$$\Delta\epsilon_{TM} = -\epsilon^2\{e_{xx}p_{12}+e_{yy}p_{11}\}. \tag{4.10}$$

The photoelastic constants for InP are $p_{11} = -0.150$, $p_{12} = -0.115$ and $p_{44} = -0.056$ [49].

Using this approximate model the degree of polarization (DOP) may be calculated as

$$\rho = -9.4\text{x}10^{-11}(\sigma_{xx} - \sigma_{yy}) \tag{4.11}$$

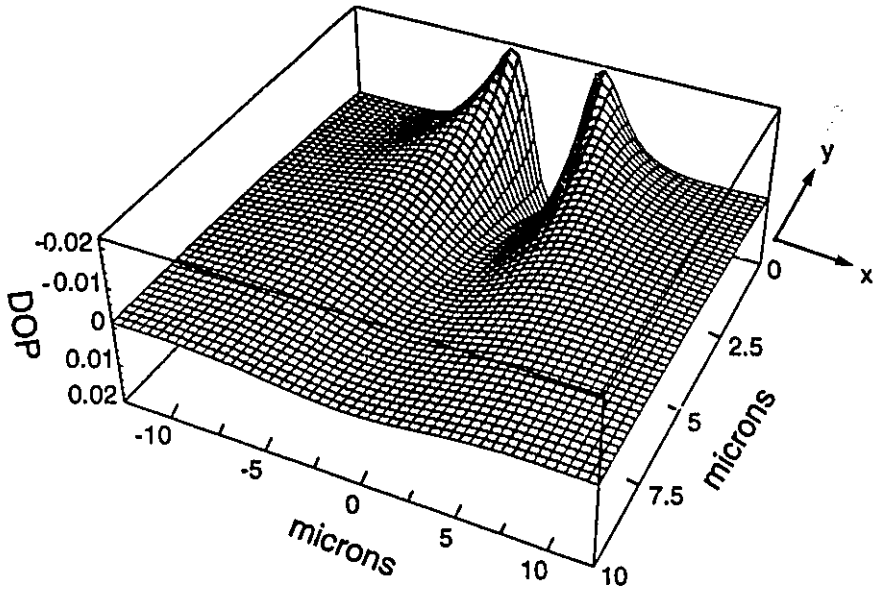

Figure 4.8: The calculated DOP pattern for the same region as in Figure 4.

for InP [38]. The quantum wells and the InGaAsP layers do not follow the above DOP expression due to a different emission wavelength and the polarization properties of the quantum wells. After cropping the top three microns from both the calculations and the data to eliminate these effects good agreement is found (Figures 4.6 and 4.8).

Using the model and matching to the DOP data, the strain in the waveguide layer may be extrapolated and subsequently the refractive index change in the waveguiding layer may be calculated (The parameters for InP have been used throughout since the photoelastic constants of InGaAsP are not well known). The edge force when extrapolated to the metal-semiconductor interface corresponds to 2.5×10^5 dyn/cm causing a peak to peak stress variation of 1×10^9 dyn/cm^2 in the waveguiding layer.

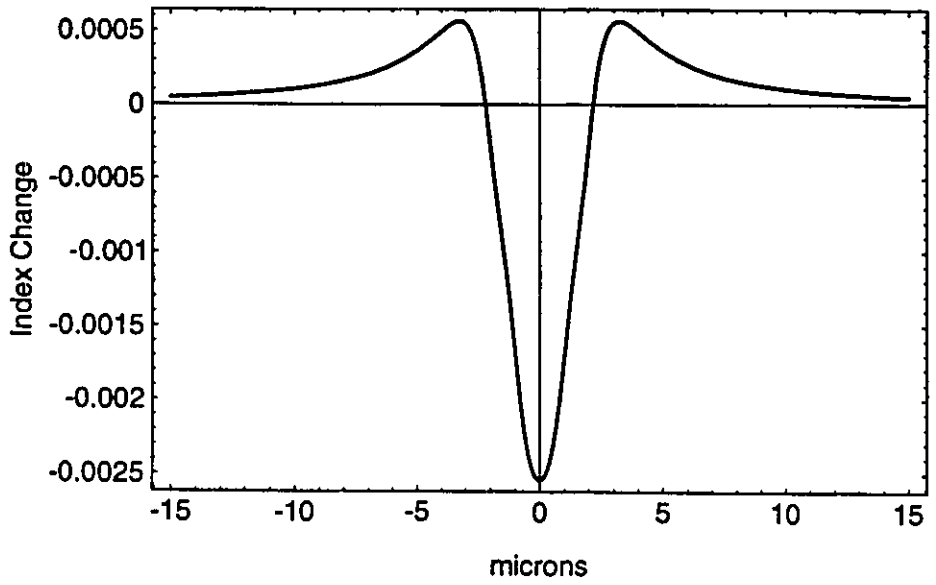

Figure 4.9: The index change in the waveguiding layer for TE propagation.

The index change is shown in Figure 4.9. The stress causes the waveguiding to be suppressed in the centre of the guide and enhanced at the metal edges as the experimental observations verify.

4.4 Waveguide Mode Calculations

The mode profile in the stressed waveguide may be calculated using a two dimensional imaginary distance beam propagation technique (BPM)[50][42] as discussed in 3.9. The imaginary distance technique converges to the lowest order waveguide mode. The BPM method used here employs finite differences on a 256 by 64 point grid. The stress induced refractive index change as calculated by the model was added to the bulk refractive index in each layer. The calculations were carried out for a wavelength of $1.38\mu m$.

The BPM results in Figure 4.10 for the calculated mode profiles clearly show the transition from a singly-peaked mode to a doubly-

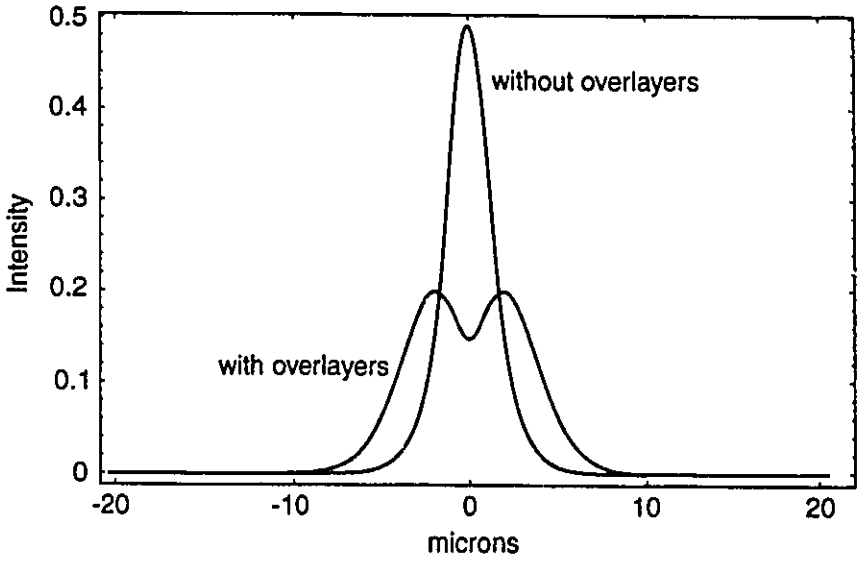

Figure 4.10: The calculated TE mode BPM intensity profiles for the waveguide with and without stress.

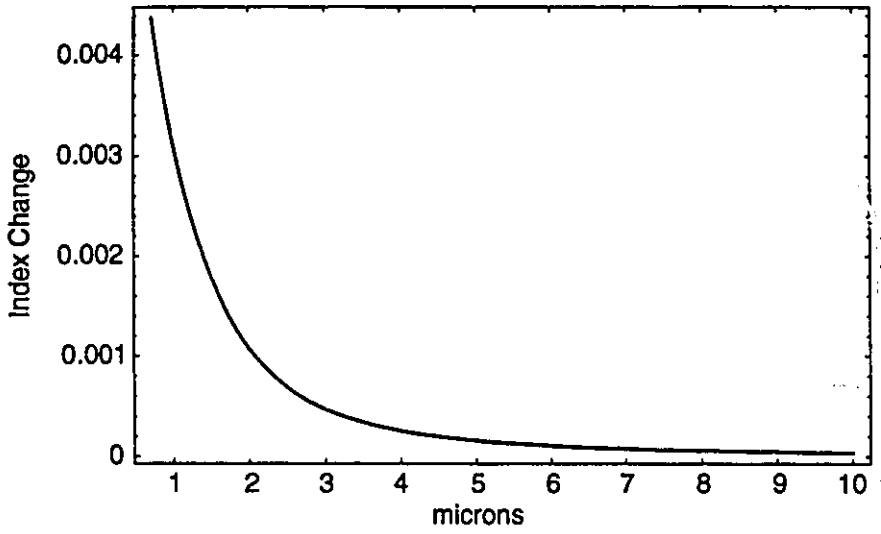

Figure 4.11: The local peak to peak index change as a function of distance from the metal.

peaked mode with the addition of stress. The calculated profile that includes the stress contribution is only slightly wider than the measured profile (Figure 4.3). The discrepancy is possibly a result of errors in the assumed values of the photoelastic constants.

4.5 Chapter Summary

In this chapter, we have shown the importance of considering the stress of metal and dielectric overlayers when designing waveguiding structures. We have also demonstrated that the BPM method can be combined with polarization resolved photoluminescence to determine waveguide stress in a self-consistent fashion. As better values of the photoelastic constants for InP and InGaAsP become available our technique for measuring processing induced stress in waveguides should prove increasingly useful.

To reduce stress in a weakly confined waveguide the thickness of the three metal layers can be varied when feasible. Alternatively, the source of the stress can be displaced away from the waveguiding layer. Figure 4.9 shows that a peak to peak index variation of 0.003 is induced in the waveguiding layer. In Figure 4.11 the calculated dependence of that variation on the depth of the waveguiding layer from the metal-semiconductor interface is shown. The depth should be large enough such that the effective index difference due to the stress is much smaller than that which provides the lateral confinement.

Chapter 5

Crossed Waveguide Design

5.1 Introduction

Many designs of guided wave integrated optical circuits require waveguide crossings to realize the increasingly complicated optical signal processing and switching functions [51][52]. This need occurs due to the planar nature of present OEIC's and from the fact that many of the most useful of the present OEIC's are built for signal switching and routing.

Waveguide X-crossings are essentially two waveguides which cross one another. In the basic X-crossing structure shown in Figure 5.1 there are two input ports and two output ports. The ideal X-crossing would allow a waveguide mode input on port 1 to be transmitted without loss to port 4 and without coupling to port 3. Port 2 would behave similarly, transmitting without loss to port 3 and not coupling any power to port 4. Unfortunately at some angles the departure from the ideal X-crossing is large. It is possible in fact to couple all of the available output power into the wrong output port. This effect is used to make electrooptic switches [7].

Therefore, the two most important considerations when designing an X-crossing are the throughput of the waveguides from the input port to the output port and the fraction of power coupled into the crossing waveguide which is crosstalk between the two waveguides. The relative throughput approaches unity and the crosstalk becomes very small as

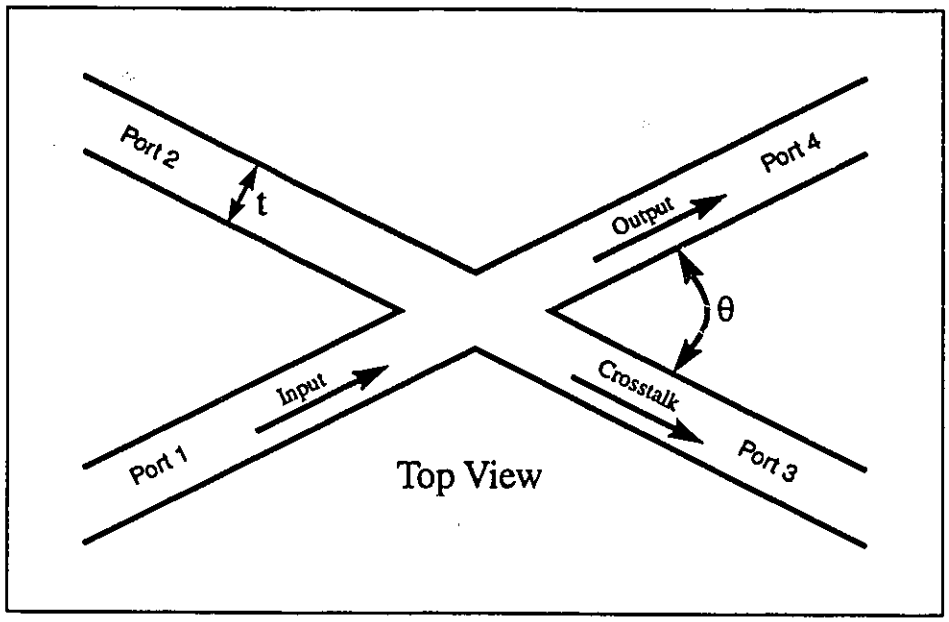

Figure 5.1: A top view of a standard rib waveguide X-crossing.

the angle θ is increased. However, there are several additional design constraints which will be discussed later that may make it advantageous to have crossings that use small angles where the crosstalk can be high.

The waveguide structure which is investigated here as the basis of the X-crossings is shown in Figure 5.2. It is an InP-based structure with real refractive indices. The guiding region is a 3000Å thick slab of index n=3.5 with the lateral confinement supplied by a 3.0μm wide rib of index n=3.2 separated from the guiding region by a 2500Å thick buffer of index n=3.2. The calculations were carried out for a wavelength of 1.3μm.

In order to study the behavior of various X-crossing structures, the two-dimensional finite-difference beam propagation method, as discussed in Section 3.6, was used. The computational window was 120μm and 4000 points wide. A comparison of the results of the two-dimensional method with a scalar three-dimensional method showed no appreciable difference. The two-dimensional method was chosen as it is computationally less intensive.

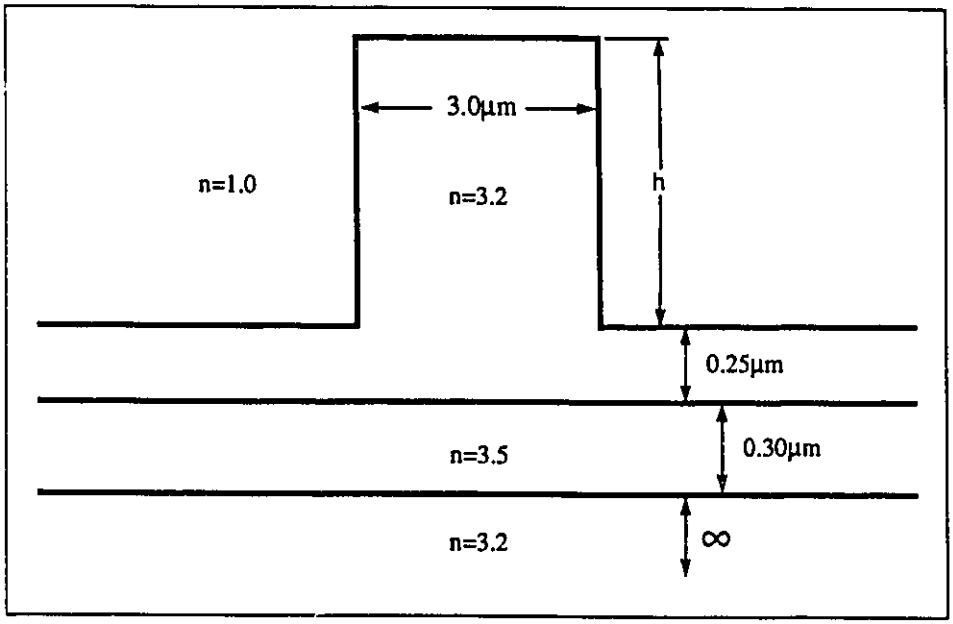

Figure 5.2: The rib waveguide structure under study. The value of h was chosen large enough so that it was effectively infinite.

X-crossings in $LiNbO_3$ waveguides have been studied more thoroughly than in semiconductor rib waveguides [53][54]. However, the refractive index profiles in the crossing regions are quite different for the two types of structures. Due to the changing rib width in the intersection region and the diffusion of the titanium, the refractive index of $LiNbO_3$ is increased in the intersection region relative to an isolated waveguide. Conclusions drawn from studies of $LiNbO_3$ can not be applied directly to the semiconductor case. In fact, we tried to duplicate some of the improvements shown for $LiNbO_3$ by Murphy[53] in the present structure and obtained a performance degradation instead of a performance improvement.

The calculations of the wave propagation through the structure are first carried out by calculating the effective index for the region under the rib and the cladding region. For the structure in Figure 5.2, the effective indices are N_{rib} and N_{clad}. These effective indices, along with the width of the waveguide and the wavelength of propagating light are the input parameters to an imaginary distance beam propagation method program. This program, after a long enough propagation distance, outputs a field profile of the lowest order mode of the waveguide structure. This field profile is used as the input field for the real-space BPM program.

To better understand the propagation of the field through a structure, a series of field profiles in Figures 5.4 and 5.5 are output at 20μm intervals throughout the propagation. These profiles show the lossless propagation before the intersection region in the low z traces of Figure 5.4. The field interacts with the intersection region in the high z traces of Figure 5.4 and the low z traces of Figure 5.5. The output mode combined with the radiation modes and crosstalk modes are clearly visible in the last traces of Figure 5.5.

A curve showing the throughput of the launching guide and the crosstalk of the second guide as a function of the angle was generated using the effective index method and the one-dimensional finite-difference beam propagation method (BPM). The result is shown in Figure 5.3.

The curve of Figure 5.3 exhibits three distinct regions. The first region (to $\theta < 4°$) is one in which the output power rapidly changes as a function of crossing angle from one arm to the other. This behavior is similar to that of a two-mode-interference coupler in which the width

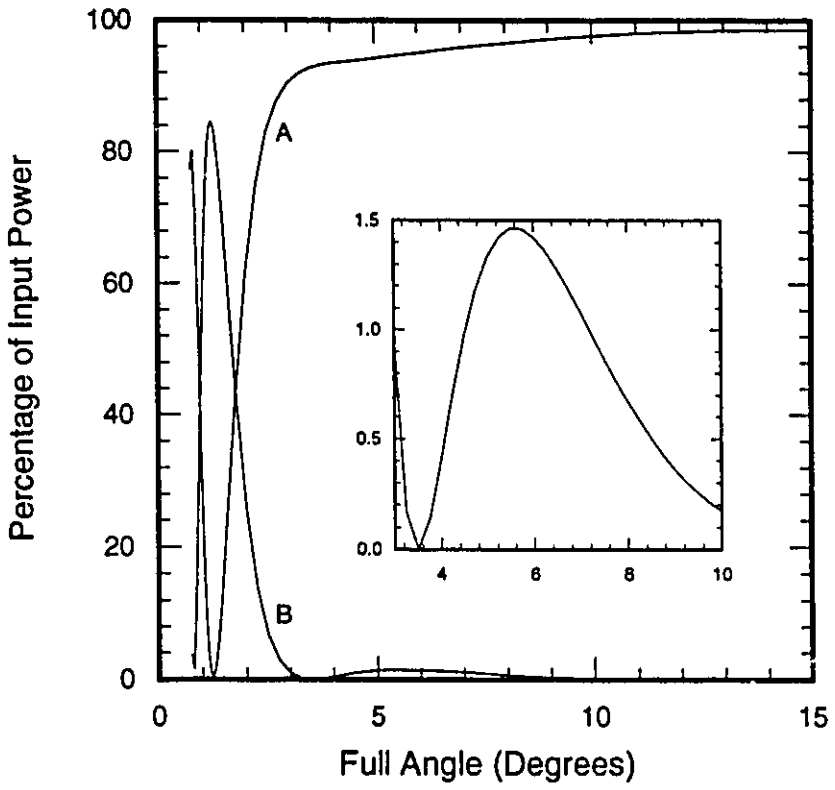

Figure 5.3: The output power in both the straight-through guide (curve A) and the crossing guide (curve B) as a function of the crossing angle. The data points consist of intervals of 0.05° from 0.75° to 1.25° and 0.25° thereafter. The inset shows a blow-up of curve B in the region of interest.

of the interaction region is uniform (see Section 5.2). In a two-mode-interference device, if the length of the interaction region is chosen so that the accumulated phase difference between its two allowed modes is an odd (or even) multiple of π, then the output power couples exclusively to the straight-through (or crossed) output guide. Thus the power coupled into either of the output guides oscillates as a function of the interaction length.

In the waveguide X-crossing (Figure 5.1) the effective interaction length between coupled modes is uniquely determined by t and θ. With t = 3μm, the interaction length is such that the phase difference between the two modes is π or more for $\theta = 1.7$ degrees or less. In this range the output power changes rapidly from one waveguide to the other as a function of crossing angle.

The second region ($4° < \theta < 10°$) is one in which the length of the crossing becomes much smaller than that required for a π phase difference. As well, the mode spreading is reduced as the crossing length becomes shorter. The final region ($\theta > 10°$) is one in which most traces of the mode coupling are gone and the throughput is very large due to a shorter nonconfining region and therefore, less mode spreading.

As will be discussed later, in many structures it can become necessary to operate in the second region and it is here that the improvements described in this thesis have a large effect.

5.2 Coupled-Mode Description

The behavior of the throughput and crosstalk as shown in Figure 5.3 can be understood by analogy to the two coupled parallel waveguides as presented in Section 1.3.8.

If the distance between the parallel waveguides at which the coupling is negligible is d then the maximum propagation length over which coupling occurs in the X-crossing (assuming propagation vectors along the symmetry line of the X-crossing) is

$$L_{eff} = \frac{\frac{a}{\cos\frac{\theta}{2}} + d}{\tan\left(\frac{\theta}{2}\right)}. \tag{5.1}$$

Figure 5.7 shows the relationship between the coupling length L_{eff}

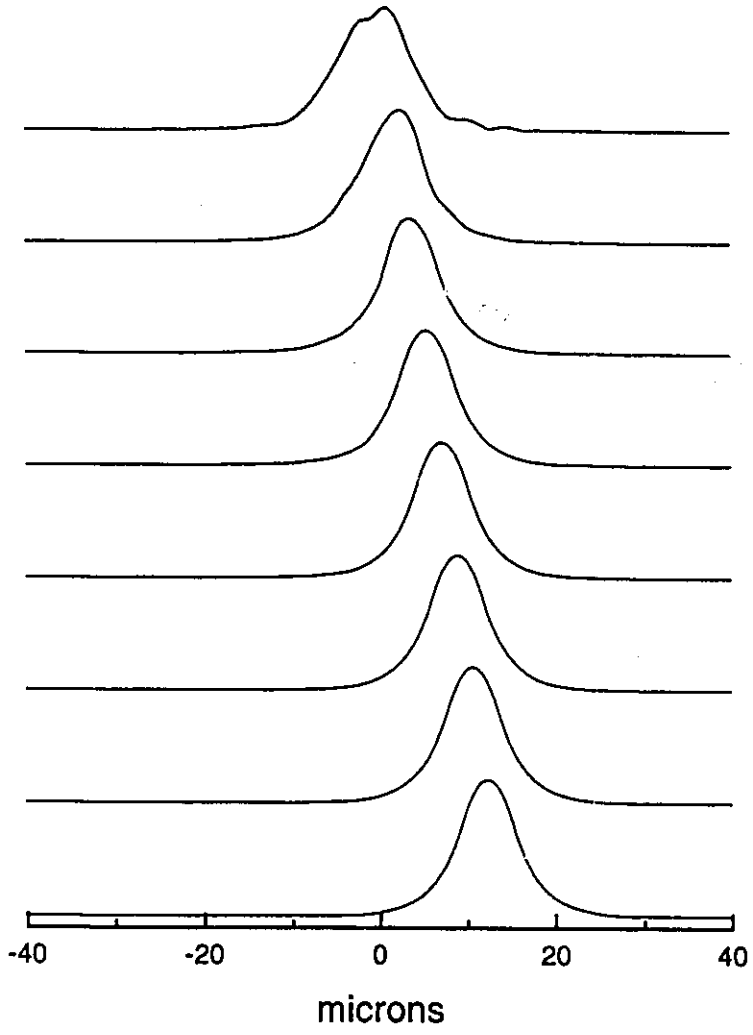

Figure 5.4: The magnitude of the electric field profiles at z = 10, 30, 50, 70, 90, 110, 130, and 150μm (from bottom to top) for the structure of Figures 5.1 and 5.2 at 5°.

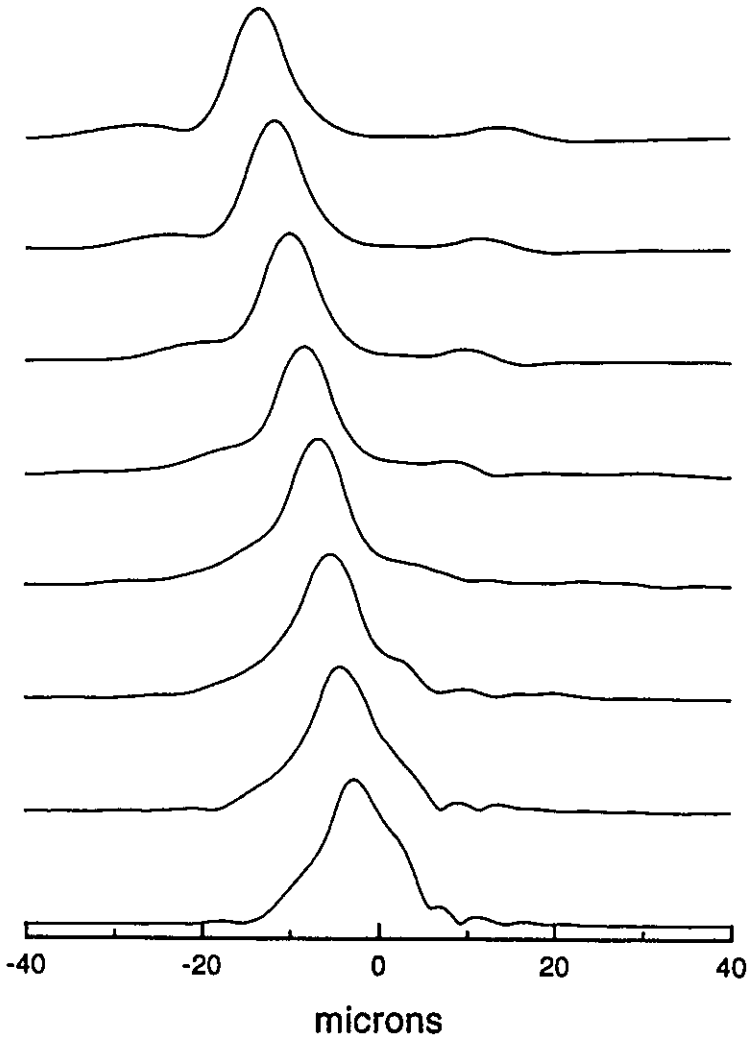

Figure 5.5: The magnitude of the electric field profiles at z = 170, 190, 210, 230, 250, 270, 290 and 310μm (from bottom to top) for the structure of Figures 5.1 and 5.2 at 5°.

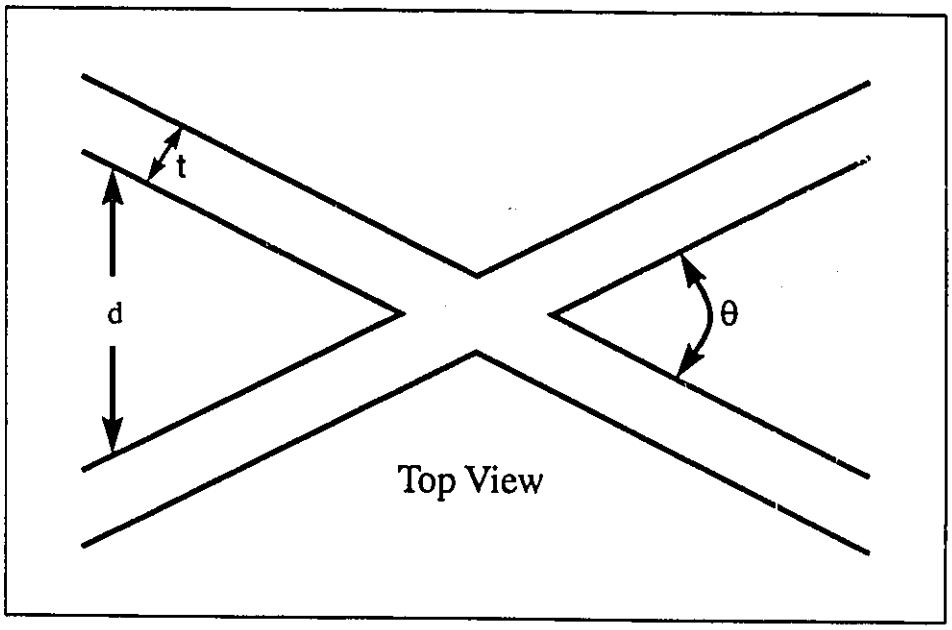

Figure 5.6: The geometry used for the comparison of the X-crossing with two parallel waveguides.

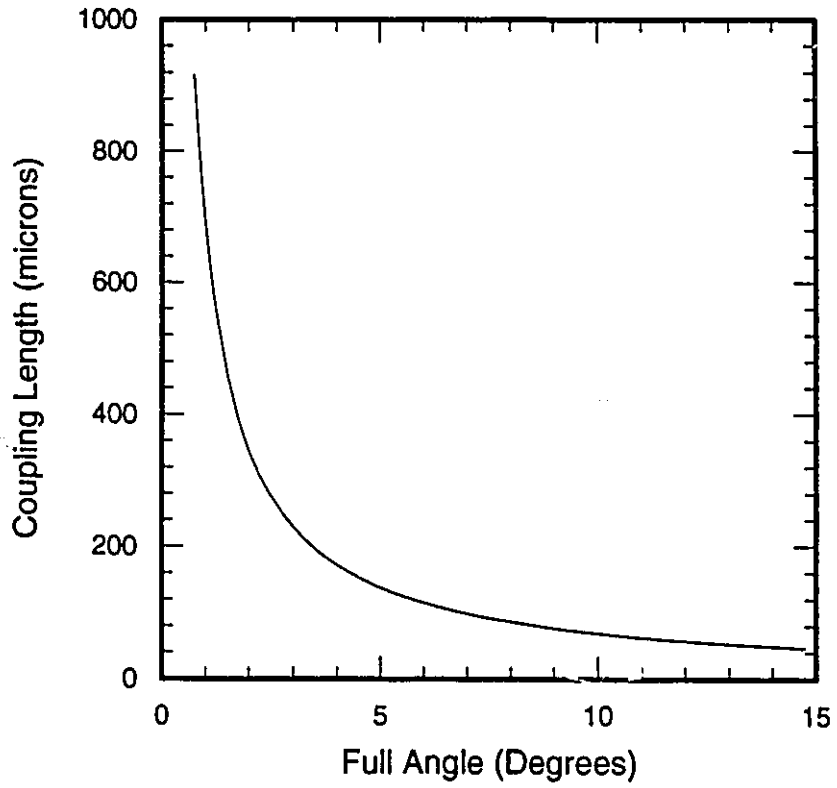

Figure 5.7: The effective coupling length for the X-crossing assuming $a = 3\mu$m and $d = 3\mu$m.

and the angle θ.

The analogy between the parallel waveguide coupling and the X-crossing breaks down in two other areas. The first being the fact that the two coupled modes have phase fronts which are not parallel. This acts to reduce the coupling from that of a parallel waveguide and the effect gets larger as the angle θ increases.

The second point is the fact that the distance between the waveguides changes as a function of z. In other words, the coupling gets larger as the space between the waveguides diminishes. The coupled mode formalism given above is only valid for waveguides which are far enough apart that the power in the waveguides can be approximated by

$$P = |\psi_1|^2 + |\psi_2|^2 \tag{5.2}$$

rather than the correct expression

$$P = |\psi_s|^2 + |\psi_a|^2 . \tag{5.3}$$

In Equations 5.2 and 5.3 ψ_1 and ψ_2 are the modal fields for the isolated waveguides while ψ_s and ψ_a are the symmetric and antisymmetric modal fields for the complete system. Equation 5.2 is clearly not appropriate for the X-crossing where the waveguides actually cross.

The above coupled mode formalism can be extended to handle this strong coupling but this requires explicit consideration of all waveguide modes including the radiation modes for each value of z. This is prohibitively numerically intensive and unnecessary since the beam propagation method can handle the problem.

5.3 Waveguide Curves

When X-crossings are used in practical integrated optical circuits they are usually combined with curved or S-bend waveguide sections so that the waveguides are parallel at the input and output. The structure shown in Figure 5.8 forms a basic building block that is incorporated into many waveguide array and matrix switch structures [55][56]. If the curved sections are circular arcs then the radius of curvature is

$$R = \frac{H^2 + L^2}{4H} \tag{5.4}$$

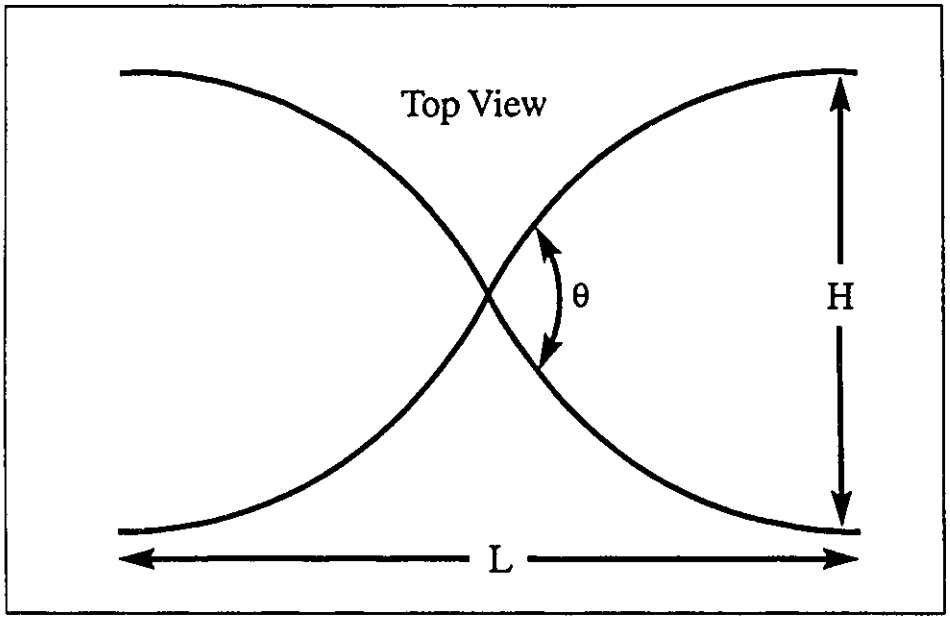

Figure 5.8: A typical curved waveguide structure used for crossed waveguides. Two parallel inputs cross, using circular arcs, with an angle θ over to two parallel outputs.

where H and L are defined in Figure 5.8. H is often constrained to be $150\mu m$ or greater to facilitate coupling to optical fibers. Depending on the degree of lateral confinement in the waveguides, R may be required to be 1.0 cm or larger to keep bending losses to acceptably low levels [57][58][59].

The angle θ of the waveguide crossing is given by

$$\theta = 2\sin^{-1}\left(\frac{L}{2R}\right). \tag{5.5}$$

For fixed H, θ decreases as R and L increase. If typical values of H and R are specified (150μm and 1.0cm for example) then θ is fixed at 3.5 degrees. Increasing θ in order to reduce crosstalk will involve a design compromise that increases bending loss. Also, as structures, including sources, become fully integrated smaller values of H will be used. This makes the crossing angle smaller for a given radius of curvature. It has been shown that other curvature profiles, such as a $1-\cos(x)$ profile, have lower losses than the two circular arcs [60] but using these profiles gives a smaller value of θ for the same H and L.

5.4 Curvature Losses

In order to understand some of the constraints on X-crossed waveguides which employ curved waveguides, it is necessary to understand the losses in such waveguides. It is clear that as a waveguide mode propagates around a curve, the outermost edge of this mode will travel farther. Some of these 'edge photons' will not be able to propagate at the required velocity and will radiate away.

Marcatili[6] has derived analytical expressions for these losses which are applicable to integrated optical waveguides. Marcatili introduces perturbations in the propagation component in the plane of curvature which are related to the change of field profile and the radiation loss. For a waveguide of width a and index n_1, with index n_2 in the cladding layers, the attenuation per radian $\alpha_c R$ is

$$\alpha_c R = \frac{1}{2}\left(1-\frac{n_2^2}{n_1^2}\right)^{-\frac{1}{2}}\left(\frac{n_2 k_{x0} a}{n_1}\right)^2\left(\frac{A}{\pi a}\right)^3\left[1-\left(\frac{k_{x0}A}{\pi}\right)^2\right]^{\frac{1}{2}}.$$

$$\frac{\mathcal{R}e^{-\frac{R}{3}\left[1-\left(\frac{k_{x0}A}{\pi}\right)^2\left(1+\frac{2C}{ak_{x0}}\right)^2\right]^{\frac{3}{2}}}}{1-\left(1-\frac{n_2^4}{n_1^4}\right)\left(\frac{k_{x0}A}{\pi}\right)^2+2\frac{n_2^2A}{n_1^2a}\left[1-\left(\frac{k_{x0}A}{\pi}\right)^2\right]^{-\frac{1}{2}}}. \tag{5.6}$$

The parameter c is related to mode conversion between guided and radiation modes:

$$c=\frac{1}{2k_{x0}a}\left(\frac{\pi a}{A}\right)^3\frac{1}{\mathcal{R}}. \tag{5.7}$$

$\mathcal{R}$ and A are given by

$$\mathcal{R}=\frac{2\pi^3R}{k_{x0}^2A^3}=2\frac{k_1^3}{k_{x0}^2}\left(1-\frac{n_2^2}{n_1^2}\right)^{\frac{3}{2}}R \tag{5.8}$$

and

$$A=\frac{\lambda}{2\left(n_1^2-n_2^2\right)^{\frac{1}{2}}}, \tag{5.9}$$

respectively. $k_1 = kn_1$, k_{x0} is the axial propagation constant of the straight waveguide, R is the radius of curvature.

$$k_{x0}a=\pi-2\tan^{-1}\frac{n_2^2}{n_1^2}\left[\left(\frac{\pi}{k_{x0}A}\right)^2-1\right]^{-\frac{1}{2}} \tag{5.10}$$

The above expression has been presented in a different form by Tamir[61] as

$$\alpha_cR = \frac{2b\left(1-b\right)\Delta nR}{a\left(2n_1\Delta nb\right)^{\frac{1}{2}}+\lambda}\cdot e^{-\frac{8\pi\Delta n}{3\lambda}\left(\frac{2\Delta n}{n_1}\right)^{\frac{1}{2}}R\left[1-(1-b)\left(1+\frac{n_1a}{4\Delta n(1-b)R}\right)^2\right]^{\frac{3}{2}}} \tag{5.11}$$

where b is given by

$$b=\frac{\frac{\beta^2}{k^2}-n_2^2}{n_1^2-n_2^2}. \tag{5.12}$$

The bending losses in dB/radian calculated by Equation 5.11 for the waveguide structure in Figure 5.2 are plotted in Figure 5.9. The magnitude of the loss is a strong function of the waveguide curvature.

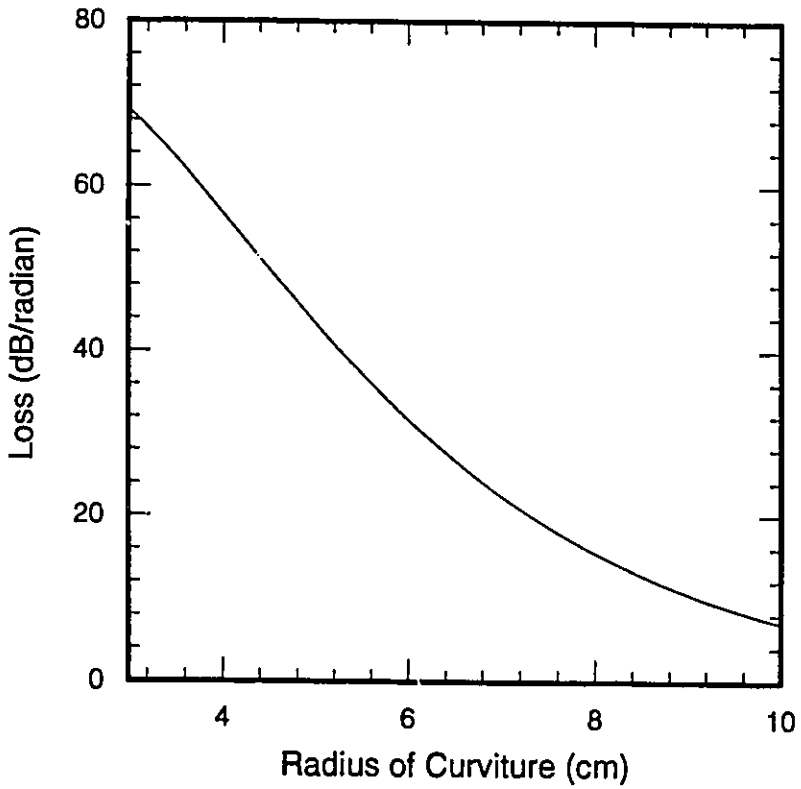

Figure 5.9: The bending loss in dB/radian for the structure under investigation.

This information may also be presented in terms of a total bending loss for crossing regions of different lengths having a fixed waveguide crossing angle of 5° and $H = 150\mu$m (Figure 5.10). Equations 5.4 and 5.5 are used to relate R and θ.

Clearly the bending loss in the waveguide curves must be one of the primary factors to be considered in designing a waveguide X-crossing structure such as that in Figure 5.8. An excess X-crossing loss of a few percent is often negligible with respect to the curvature losses and priority should be given to minimizing curvature losses while maximizing the throughput to crosstalk ratio.

5.5 Chapter Summary

Waveguide X-crossings have been presented in context with their current use in integrated optics. The small angle performance of an X-crossing has been calculated using the Beam Propagation Method. A discussion of the various features of the performance curve is discussed by analogy to double-mode interference couplers.

A discussion of waveguide curves and their relationship with X-crossings in many designs highlights the fact that depending upon the total structure the waveguide losses may actually be dominated by the curvature losses and not the X-crossing losses. Since this is the case, it is apparent that priority must be given to increasing X-crossing performance at the angles where the curvature losses are minimized. The performance increase to be sought is an increase in the crosstalk immunity of the crossing. A small increase in the throughput loss of the X-crossing can be tolerated if it results in a complete structure with a much smaller curvature loss. Results showing such performance improvements are presented in the next chapter.

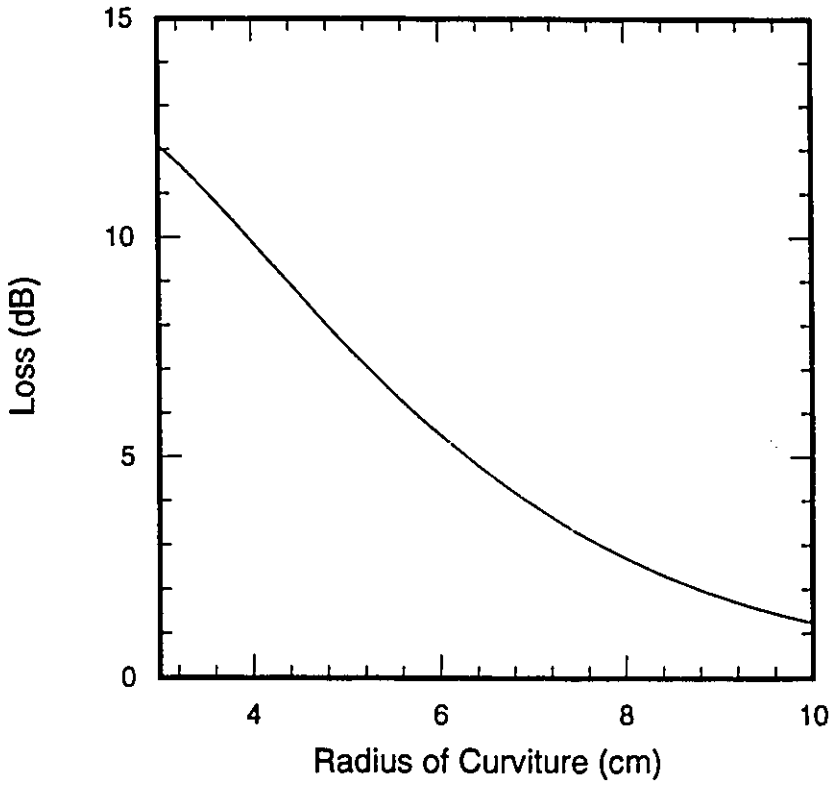

Figure 5.10: The bending loss in dB for the structure under investigation with parallel input and output waveguides, circular arcs and a 5° crossing angle.

Chapter 6

Modifications of X-crossings

6.1 Introduction

As shown in Figure 5.3 the performance of a rib waveguide X-crossing degrades as the crossing angle becomes smaller. As discussed in Chapter 5 it would, at times, be beneficial to have good X-crossing performance at angles $4° < \theta < 10°$.

Figure 5.3 shows as much as a 1.5% crosstalk signal in this region. This is clearly not acceptable for many purposes. This crosstalk rise arises primarily from two effects. The first is the coupling of the waveguide modes in the intersection region. The primary geometrical influence on this coupling is the region between the two waveguides (The acute vertices). Section 6.2 discusses modifications of these vertices to improve the X-crossing performance.

The second reason for the crosstalk is mode expansion into the crossing guide. The mode expansion also contributes to the through loss. To improve this source of crosstalk, Section 6.3 discusses modifications to these obtuse vertices which can improve the performance with respect to the mode expansion.

The combined effects of both of these modifications will be shown in Section 6.4 to dramatically improve the performance in the $4° < \theta < 10°$ range.

6.2 Modification of the Acute Vertices

To improve the crossing performance between the angles $4° < \theta < 10°$, one wishes to minimize the rise in crosstalk while maintaining high throughput. For crossing angles greater than about four degrees the losses and crosstalk may be viewed as resulting, in part, due to cross coupling of the two waveguides that occurs in the regions on either side of the crossing. Here the guides are separated by only a small distance and the coupling mechanism is similar to that of a dual channel coupler. A small fraction of the input power will couple to the crossed waveguide before the two guides combine. Similarly, at the output, some cross coupling will occur after the guides have separated but while they still are close to each other.

If the shape of the waveguide crossing is modified as shown in Figure 6.1 the cross coupling between the guides as they converge at the input and diverge at the output is greatly reduced. The result is a significant reduction in the overall crosstalk. The crossing region is made longer by this modification, which increases the effects of mode expansion. Our calculations show, however, that this results in only a small reduction in the throughput for reasonable cut widths, w.

The resultant throughput and crosstalk curves for a blunted vertex with $w = 2.0\mu m$ is shown in Figure 6.2. The inset shows that the peak value of the crosstalk in this region has been decreased by a factor of three with respect to the standard X-crossing results in Figure 5.3. The throughput of the primary guide has only minimally decreased with respect to the same figure. A plot of the throughput divided by the crosstalk as a function of crossing angle is given as Figure 6.3. For the modified structure there is a significant improvement in the signal to crosstalk ratio for angles near six degrees where the local maximum in the crosstalk is reduced. Also, the range of angles for which the signal to crosstalk ratio is low is narrowed considerably, making the greatest improvements at the edges of this region (i.e. crossing angles near 4 or 10 degrees).

Figure 6.4 shows the improvement in the signal to crosstalk ratio as a function of cut width, w, for several different crossing angles. At the ends of the relevant region of angles it is possible to achieve a nine times improvement in the signal to crosstalk ratio. At all angles a four

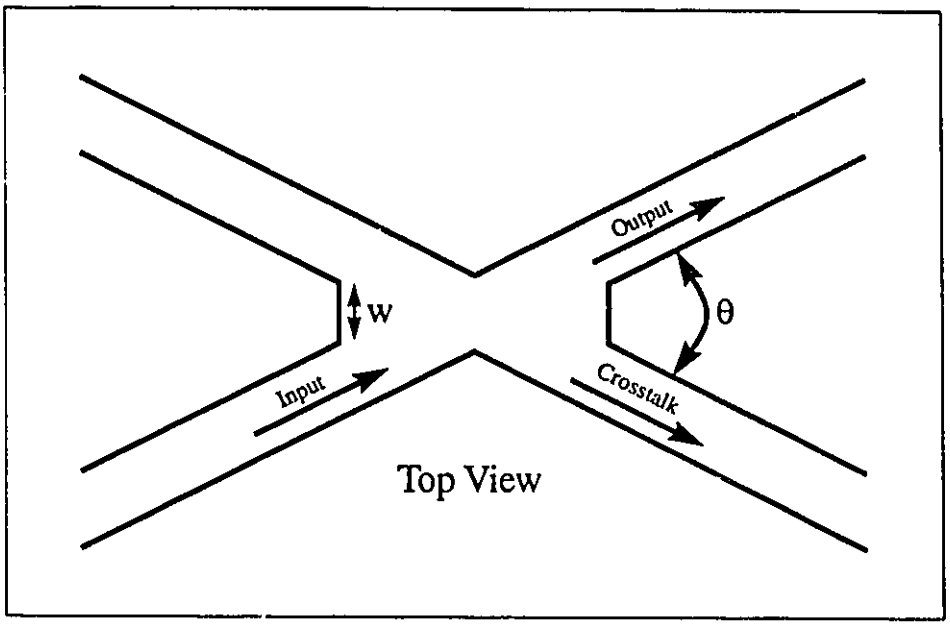

Figure 6.1: The modified waveguide profile. The vertices between the two input and two output guides have been blunted.

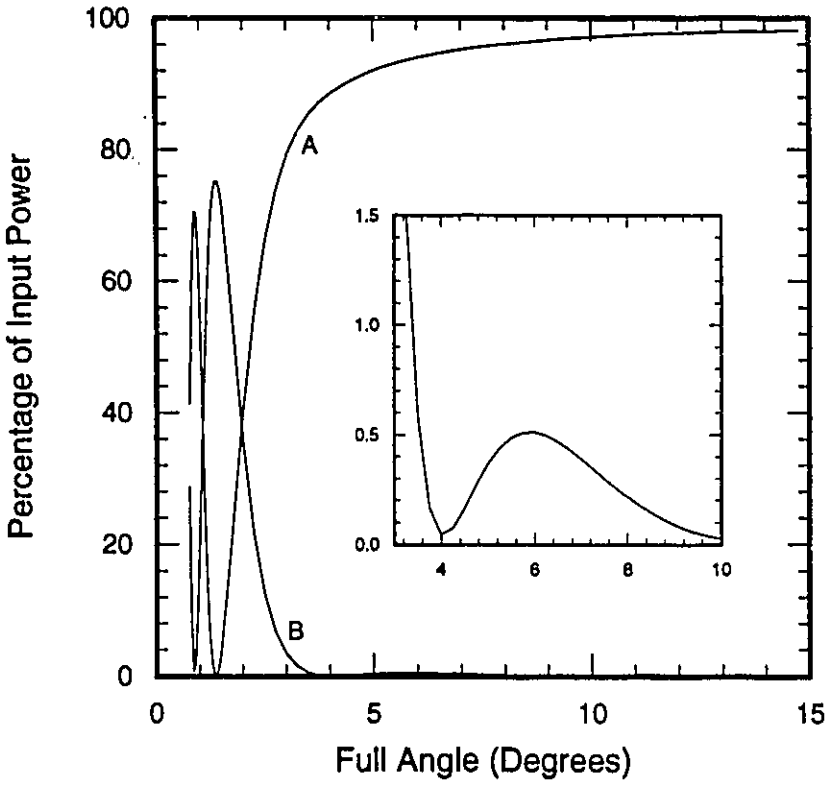

Figure 6.2: The throughput (curve A) and crosstalk (curve B) for the structure of Figure 6.1 with $w = 2.0\mu m$. The crosstalk in the region shown in the blow-up has decreased by approximately three times from Figure 5.3.

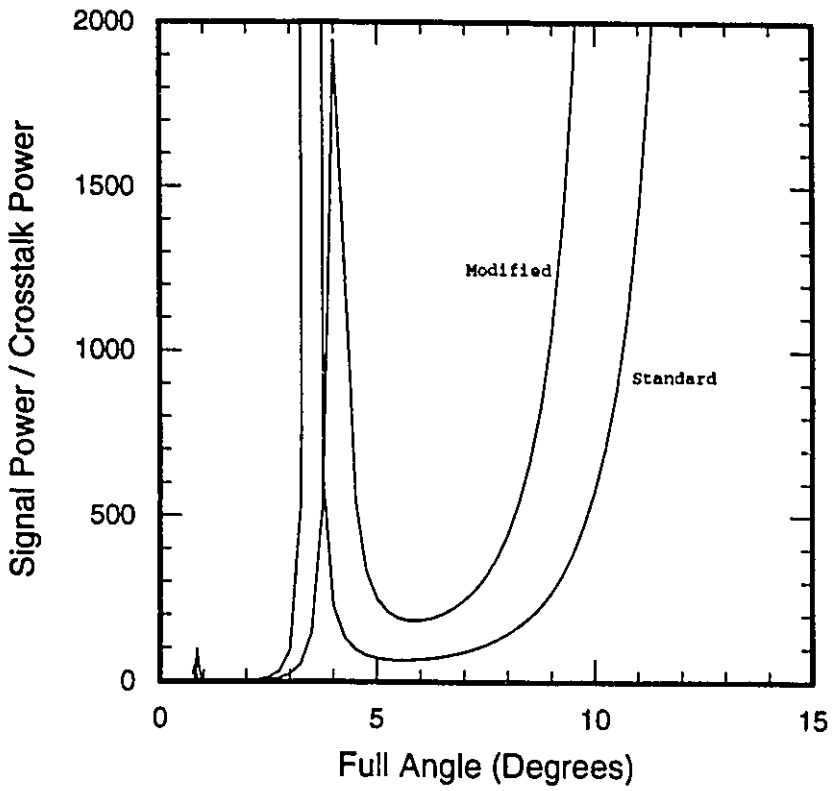

Figure 6.3: The throughput to crosstalk ratio for both the original and modified (w = 2.0μm) x-crossings.

times improvement is possible. The peaking of the 4° degree data is due to the movement of the crosstalk minimum in Figure 6.2 at $\theta = 4°$ to longer angles as w is increased.

A plot of the throughput relative to the throughput of the original X-crossing (Figure 6.5) shows that at the larger angles the performance improvement can be made with only a two to three percent reduction in throughput. For most of the angles in the region of interest, the throughput to crosstalk improvement plateaus at w = 3μm. Although the throughput loss continues to increase, its slope is gentle. These gentle slopes make fabrication of improved X-crossings easy to achieve, since the precise choice of w is not critical. The exact angles at which the improvement occurs is dependent on the structure under study. The angles of interest can typically shift by up to two degrees. The angles of interest shift to larger angles as the lateral confinement of the waveguide is increased. The last crosstalk minimum before the region of interest is typically in the region of between three to five degrees for InP based structures at 1.3μm.

6.3 Modification of the Obtuse Vertices

We will now consider the minimization of the crosstalk rise subject to high throughput for $4° < \theta < 10°$ by changing the geometry of the obtuse vertices. In this region of angles the losses and crosstalk partly result from the spreading of the input waveguide mode as it propagates within the wider crossing region. As the expanded mode is not perfectly matched to the mode of the straight-through guide at the output the throughput is less than 100% while the overlap of the expanded mode with the crossed waveguide's mode gives rise to crosstalk. Further, an additional contribution to crosstalk results from the cross coupling of the two waveguides in the regions on either side of the crossing where the guides are separated by a small distance. A small fraction of the input power will then couple to the crossed waveguide before the two guides combine in the same manner as in a dual channel coupler. A similar effect is of course present at the output.

In the previous section, improvements of up to nine times in the signal to crosstalk ratio achieved by suitably tailoring the two vertices

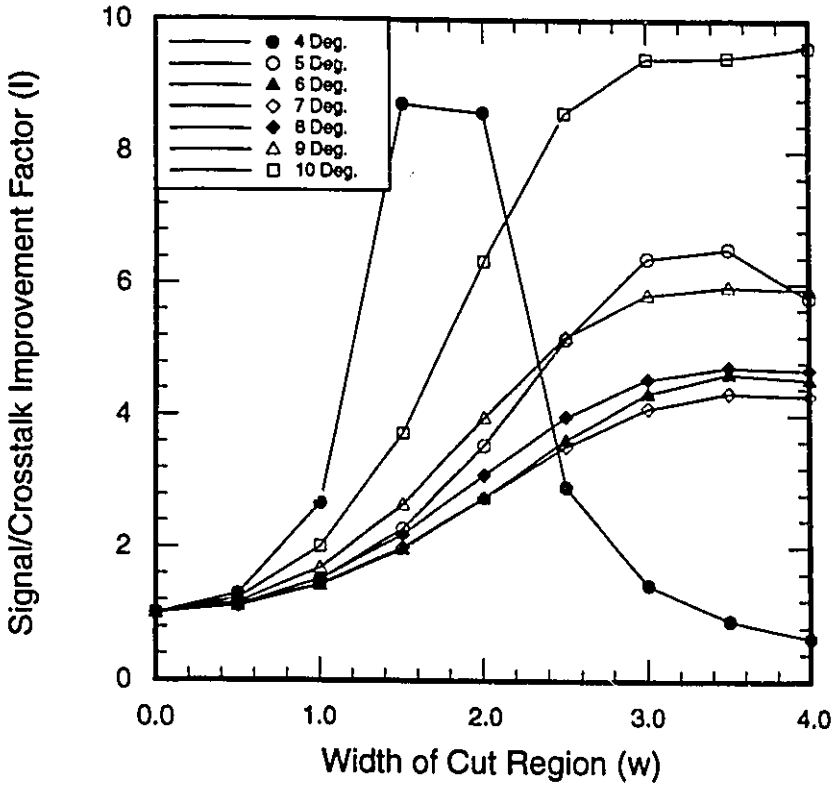

Figure 6.4: The improvement in throughput/crosstalk ratio for a variety of angles and cut widths w.

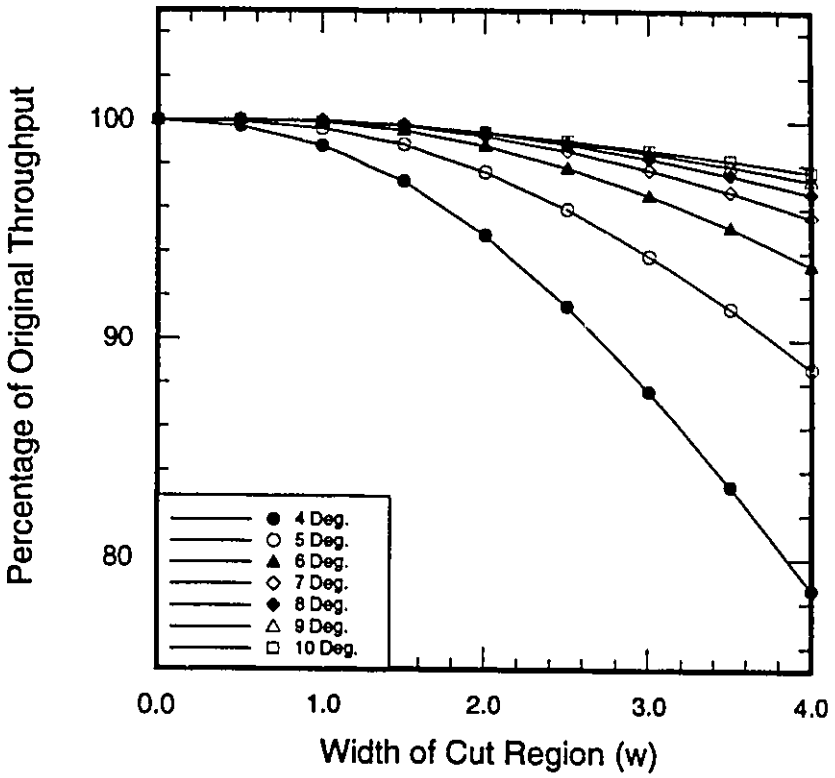

Figure 6.5: The change in throughput relative to an unmodified X-crossing.

between the waveguides. In this section the two remaining vertices are modified, as in Figure 6.6, to achieve typical crosstalk suppression factors between one and 14.

Our new design improvement labeled with the symbol p consists of linearly decreasing the width of the waveguide intersection region starting from the projection in the y direction of the end of the acute vertex between the two waveguides as shown in Figure 6.6. The waveguide width continues to decrease towards points located a distance p from the obtuse vertex. The thinned region is terminated when it reaches the projection of the output waveguide's edge into the intersection region. In this manner the distortion of a given input waveguide does not interfere significantly with the throughput of the other input waveguide.

Figure 6.7 shows the signal to crosstalk improvement factor, defined as

$$I = \frac{\left[\frac{Signal}{Crosstalk}\right]_{modified}}{\left[\frac{Signal}{Crosstalk}\right]_{unmodified}}, \tag{6.1}$$

for various values of the thinning parameter, p with $w = 0.00$. The signal to crosstalk improvement achievable for $5° < \vartheta < 10°$ range from $I \approx 1.3$ to $I > 14$. Further by plotting the throughput of the modified X-crossing relative to that of the unmodified X-crossing as in Figure 6.8 we find that for all angles $\theta \neq 4°$, the performance improvement of Fig. 6.7 is accompanied by a throughput increase of up to 0.5%.

For $\theta = 4°$ the performance improvement of Figure 6.4 is > 50 and exhibits a distinct peaking character which is distinctly different from the behavior of the other angles. This peaking behavior, as in the previous Section, is due to a shifting of the crosstalk minimum shown in Figure 6.2 through $\theta = 4°$. The throughput of the $\theta = 4°$ case is only accompanied by a throughput improvement for $p \leq 1.00\mu$m.

6.4 Simultaneous Modification of Acute and Obtuse Vertices

In this section the modifications used in the two previous sections will be combined. The parameter space investigated is $0.00 \leq w \leq 4.00$

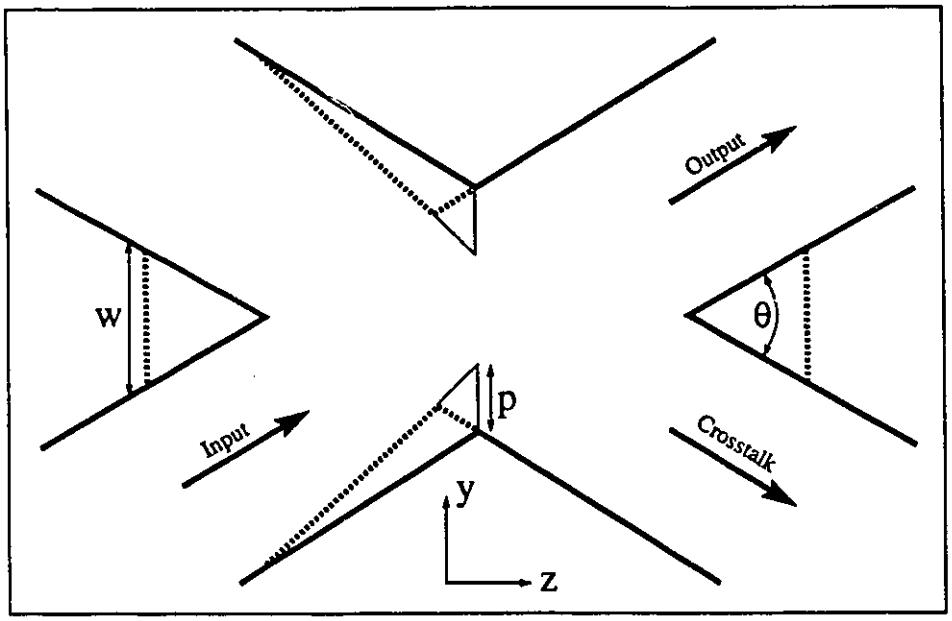

Figure 6.6: The modified waveguide intersection region for the modification of the obtuse vertices. The dashed lines represent the new rib boundaries.

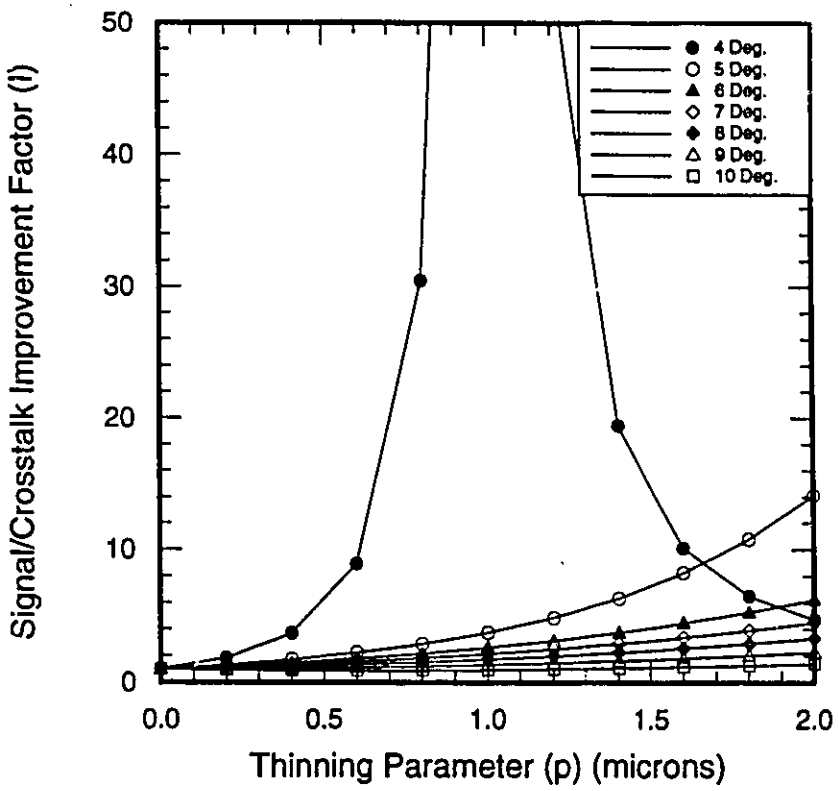

Figure 6.7: The Signal/Crosstalk Improvement Factor for various thinning parameters, p, and w = 0.00μm.

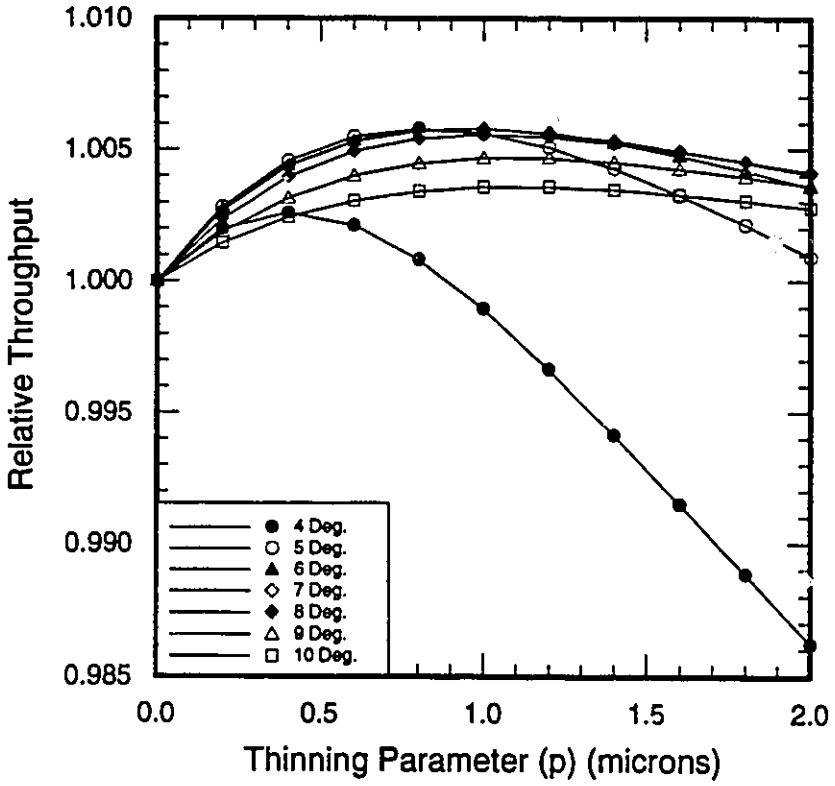

Figure 6.8: The change in throughput relative to an unmodified X-crossing for w = 0.00μm and various thinning parameters, p.

and $0.00 \leq p \leq 2.00$. The results of these simulations are presented in Figures 6.9 through 6.24. Each set of data represents a fixed value of the parameter w and is presented in two consecutive figures. The first is the signal to crosstalk improvement factor while the second is the relative throughput as compared to an unmodified X-crossing.

The distinctive features of these curves are the large, broad peaks in the Signal/Crosstalk Improvement Factor. The peaks are the result of a shifting of the crosstalk minimum shown in Figure 6.2 to larger angles with increasing X-crossing perturbation (either w or p). These peaks are broad enough to make fabrication of structures which utilize them feasible. For all angles except 10° a crosstalk improvement factor of > 100 is achievable with the larger angles favoring larger perturbations. The improvements are achievable with, at most an excess loss of 4%.

The lesser improvement at 10° is less important due to the relatively good original throughput to crosstalk ratio at these angles (Figure 6.3).

A series of fields at $z = 20\mu$m increments for the structure of Figures 5.2 and 6.6 at 5° with $w = 2.00\mu$m and $p = 0.75\mu$m are presented in Figures 6.25 and 6.26. These figures may be directly compared to the standard X-crossing of Figures 5.4 and 5.5. A smoother transition through the intersection region occurs with no visible crosstalk peak at the output as shown in Figure 6.26.

6.5 Chapter Summary

In this chapter we have studied the angular variation of the loss and cross-coupling in modified X-crossed rib waveguides. We find that by changing the shape of the crossing region, the crosstalk, for angles $4° < \theta < 8°$ can typically be reduced by 20 dB to a total crosstalk which is ≈ 37 dB down from the signal level. The resulting increase in design-space enables smaller dimensions or lower total losses, particularly for structures which incorporate curved waveguides, without degrading performance. The achievable improvement in crosstalk is relatively independent of the waveguide widths and rib etch depths although the angular region at which an improvement is registered may be displaced to slightly larger or smaller angles.

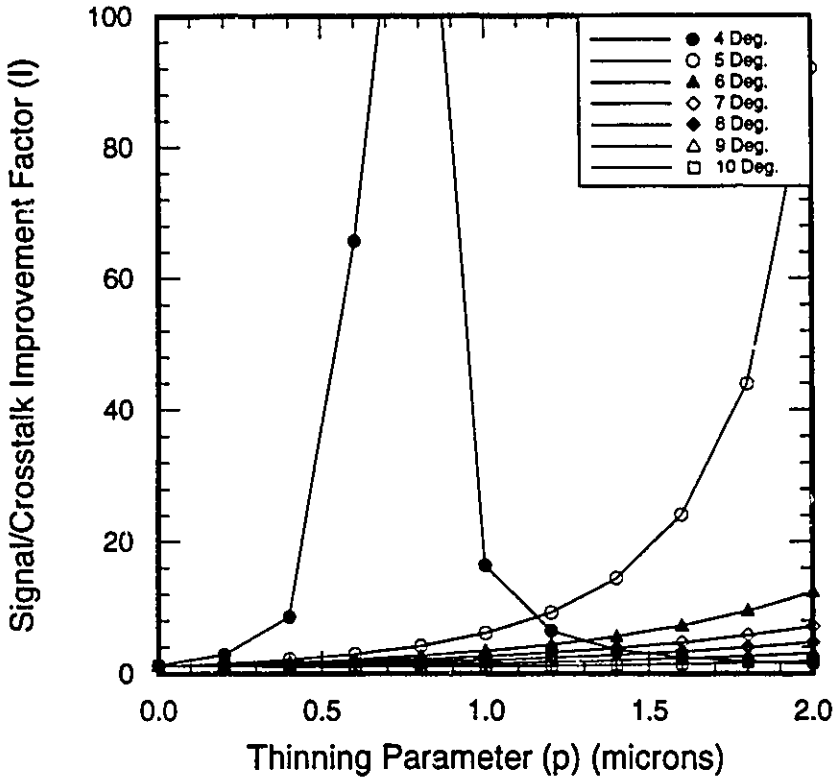

Figure 6.9: The Signal/Crosstalk Improvement Factor for various thinning parameters, p, and w = 0.50μm.

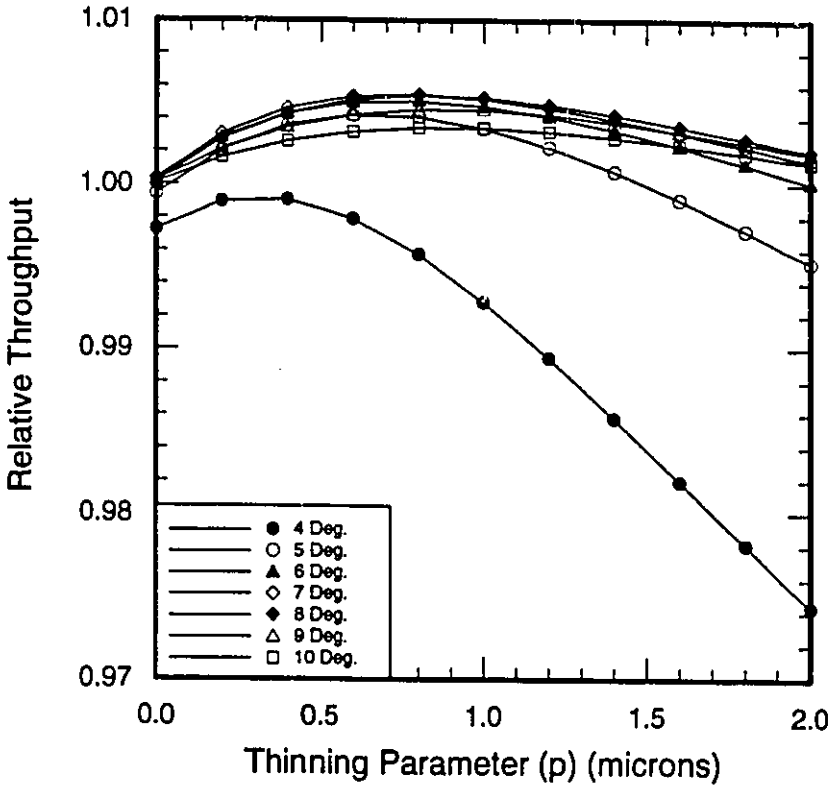

Figure 6.10: The change in throughput relative to an unmodified X-crossing for w = 0.50μm and various thinning parameters, p.

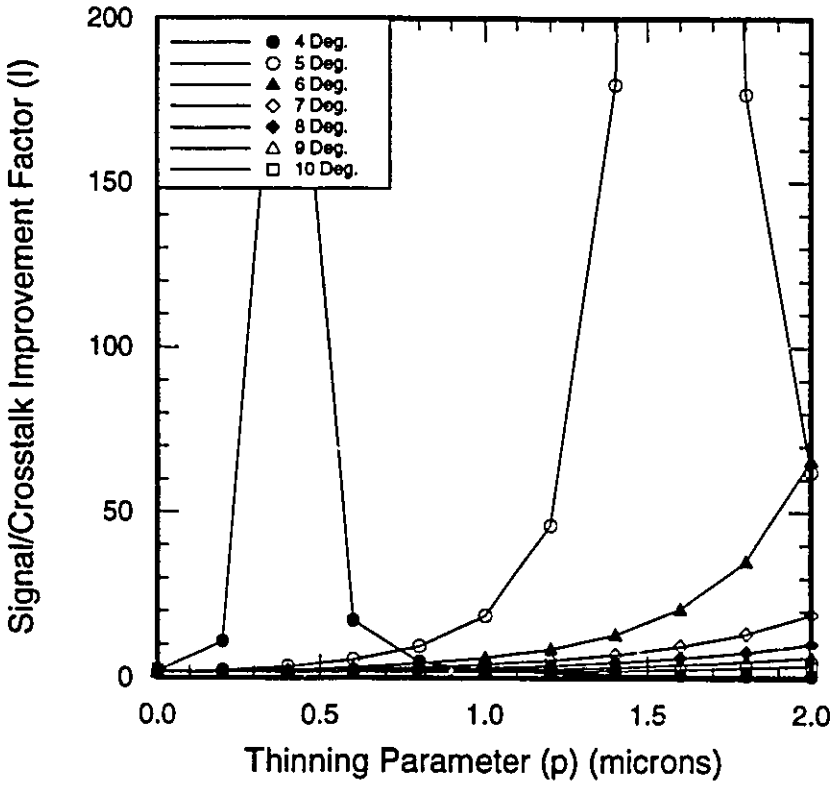

Figure 6.11: The Signal/Crosstalk Improvement Factor for various thinning parameters, p, and w = 1.00μm.

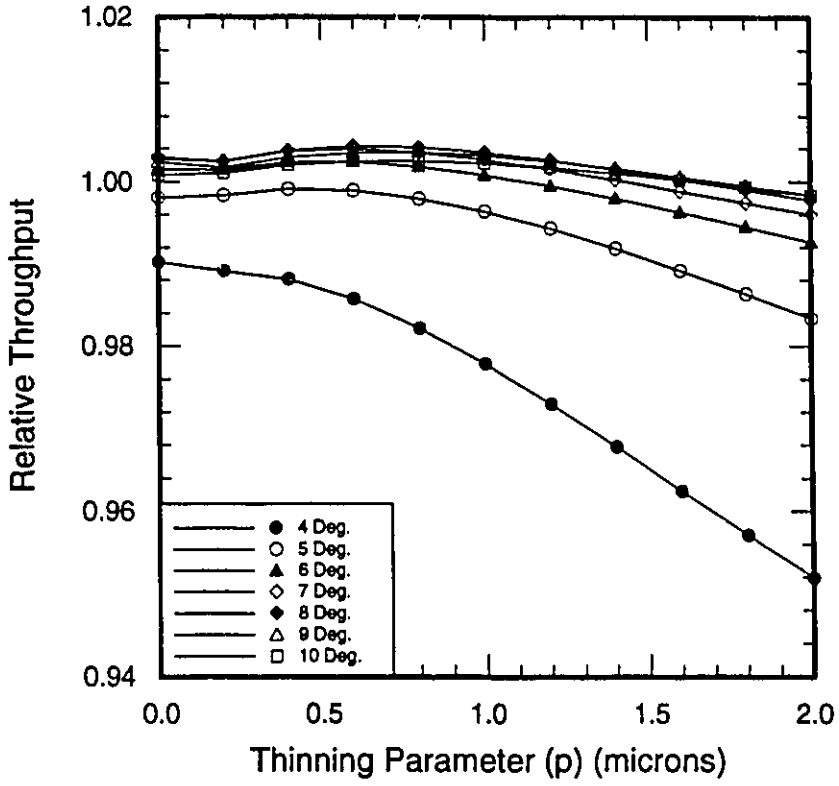

Figure 6.12: The change in throughput relative to an unmodified X-crossing for w = 1.00μm and various thinning parameters, p.

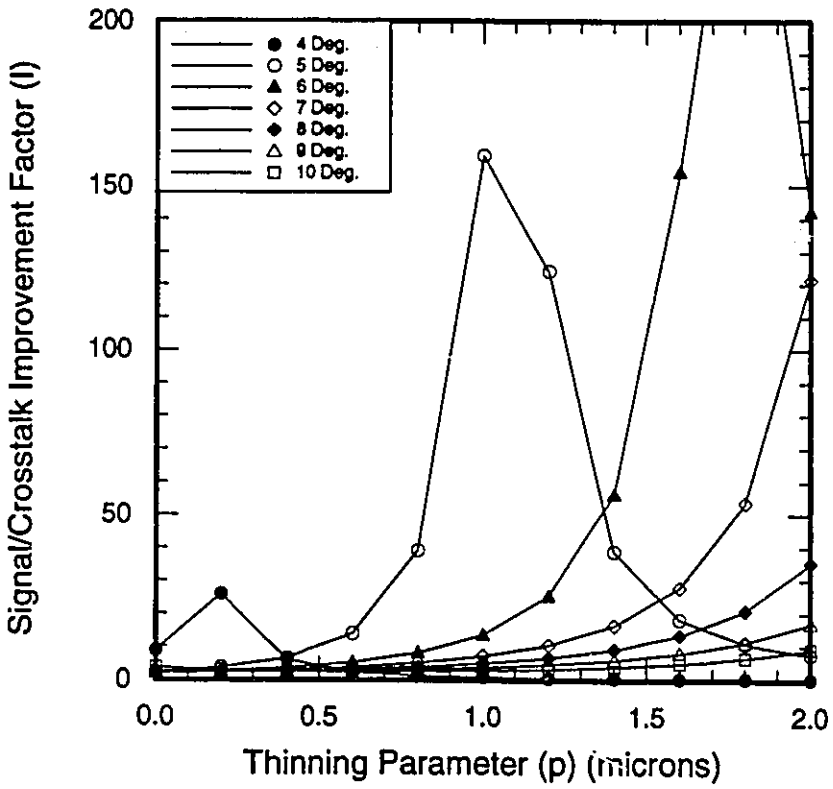

Figure 6.13: The Signal/Crosstalk Improvement Factor for various thinning parameters, p, and w = 1.50μm.

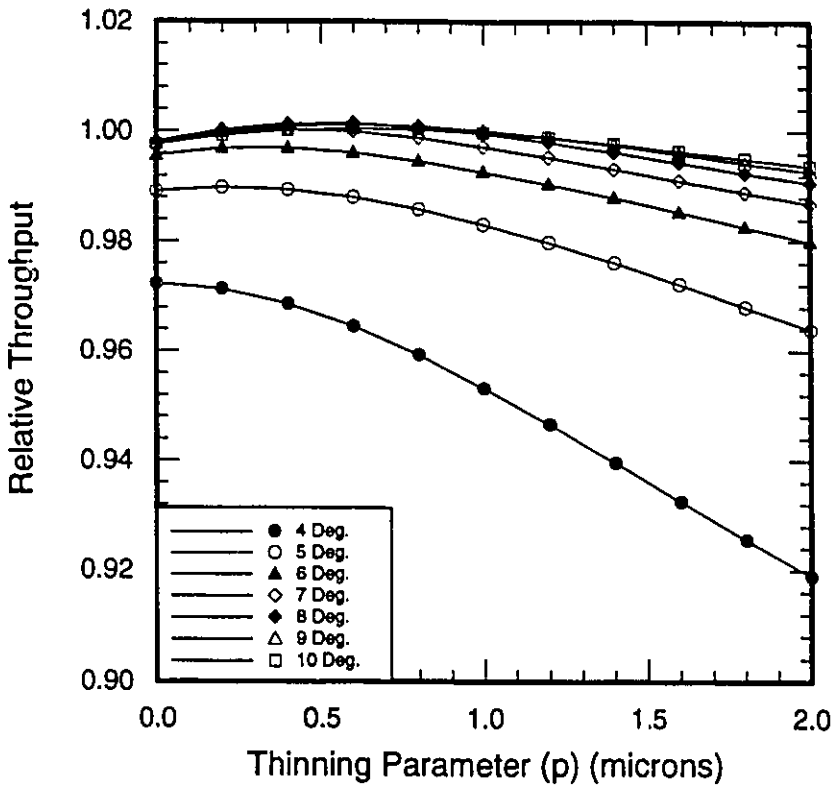

Figure 6.14: The change in throughput relative to an unmodified X-crossing for w = 1.50μm and various thinning parameters, p.

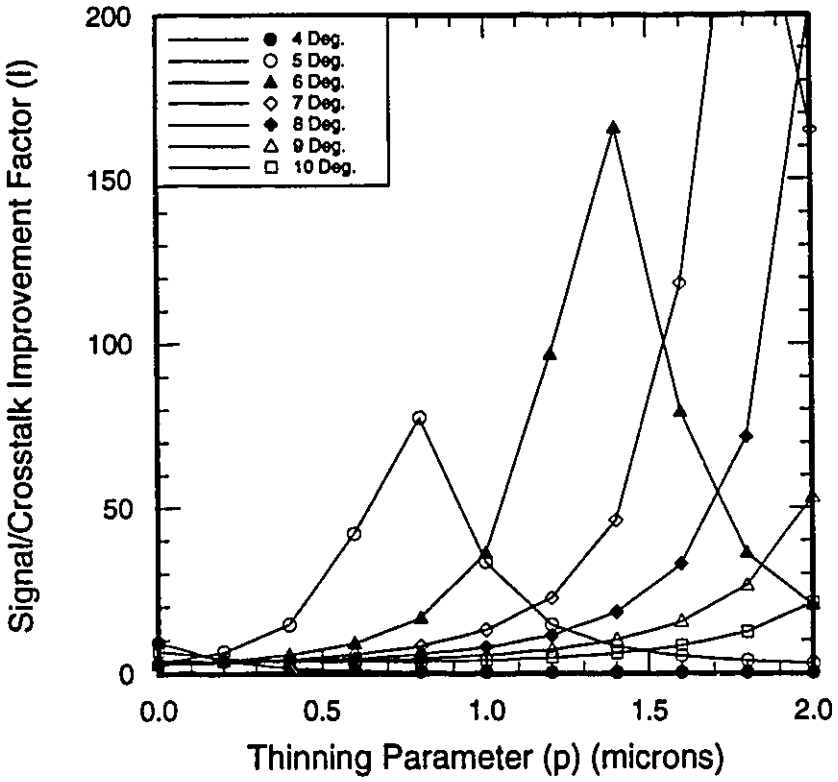

Figure 6.15: The Signal/Crosstalk Improvement Factor for various thinning parameters, p, and w = 2.00μm.

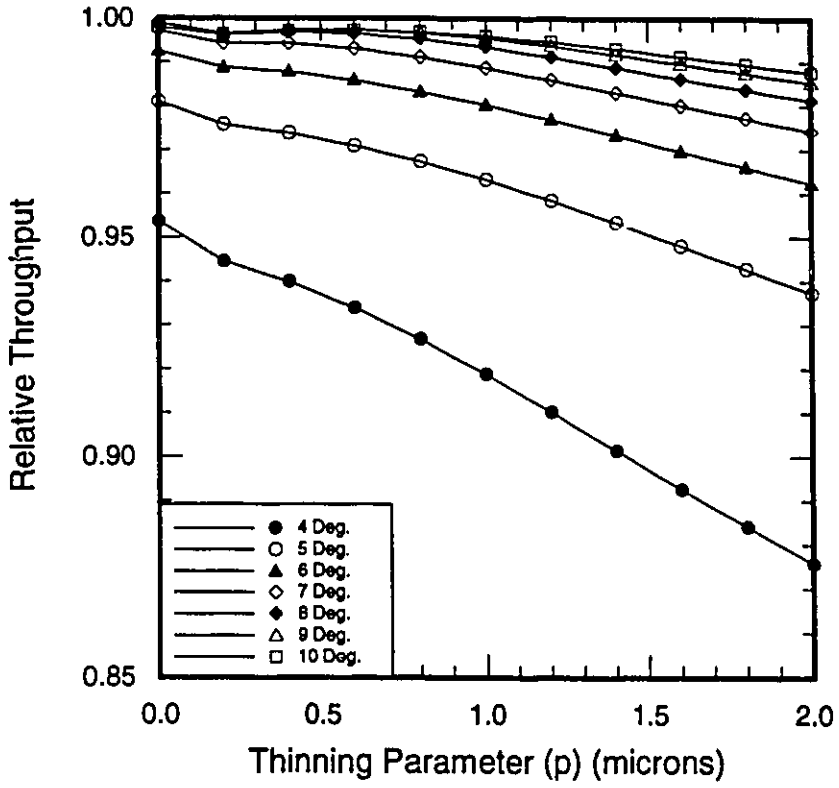

Figure 6.16: The change in throughput relative to an unmodified X-crossing for w = 2.00μm and various thinning parameters, p.

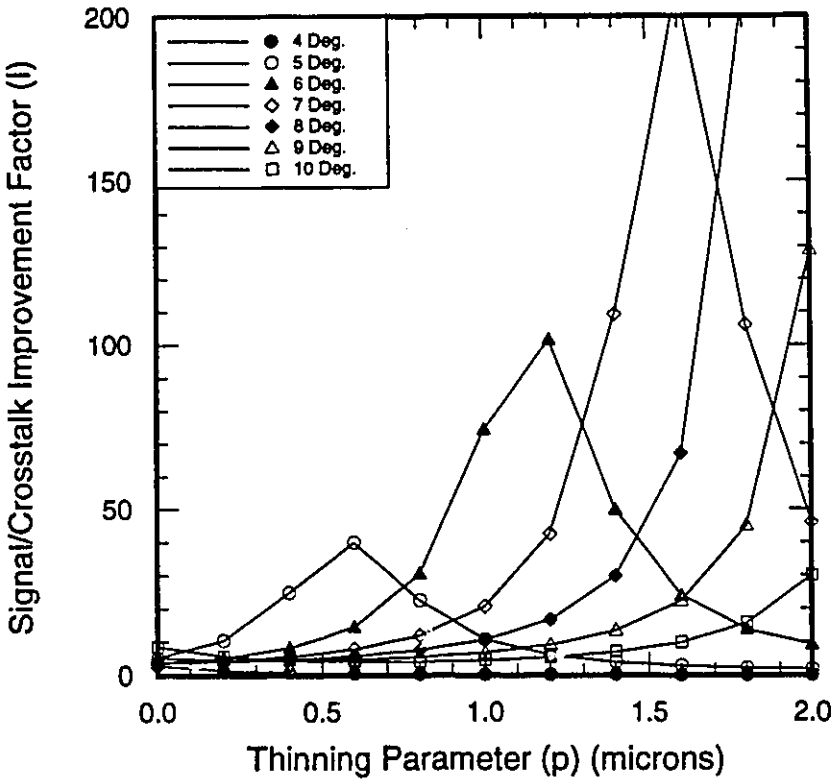

Figure 6.17: The Signal/Crosstalk Improvement Factor for various thinning parameters, p, and w = 2.50μm.

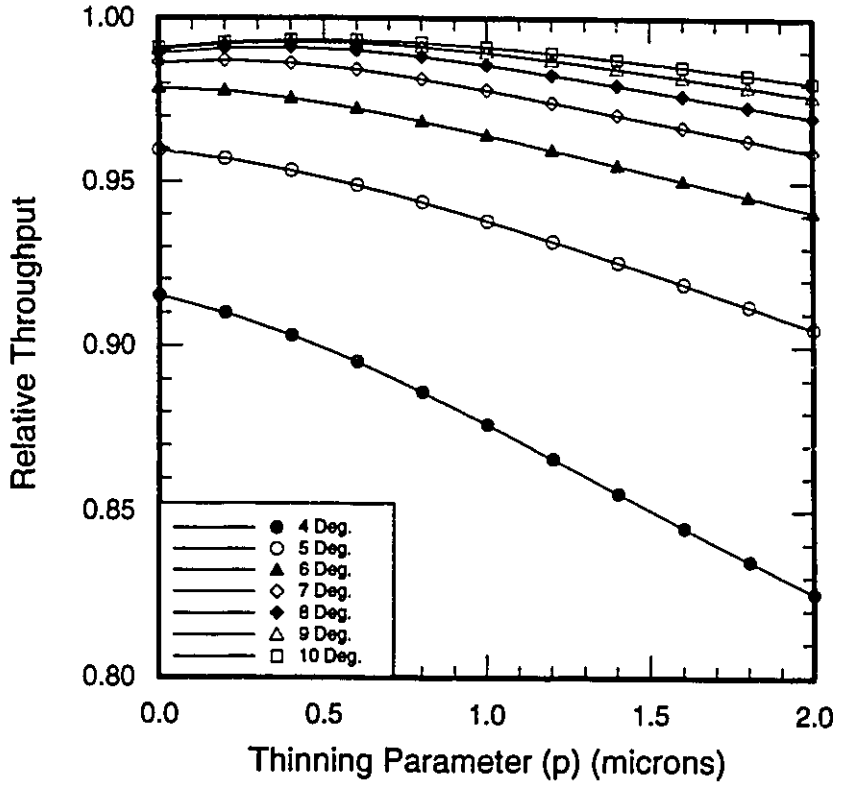

Figure 6.18: The change in throughput relative to an unmodified X-crossing for w = 2.50μm and various thinning parameters, p.

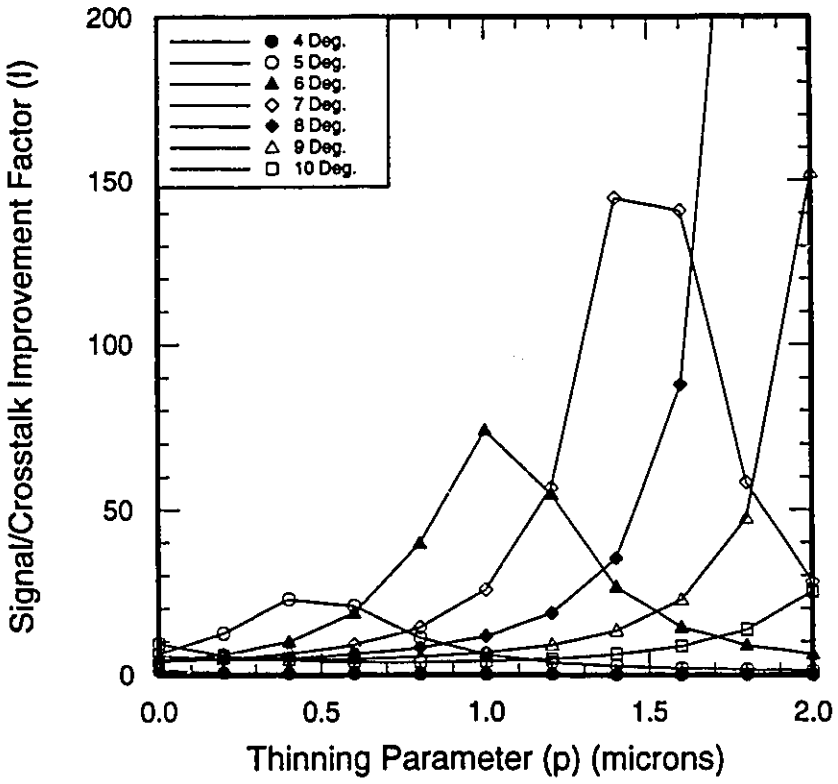

Figure 6.19: The Signal/Crosstalk Improvement Factor for various thinning parameters, p, and w = 3.00μm.

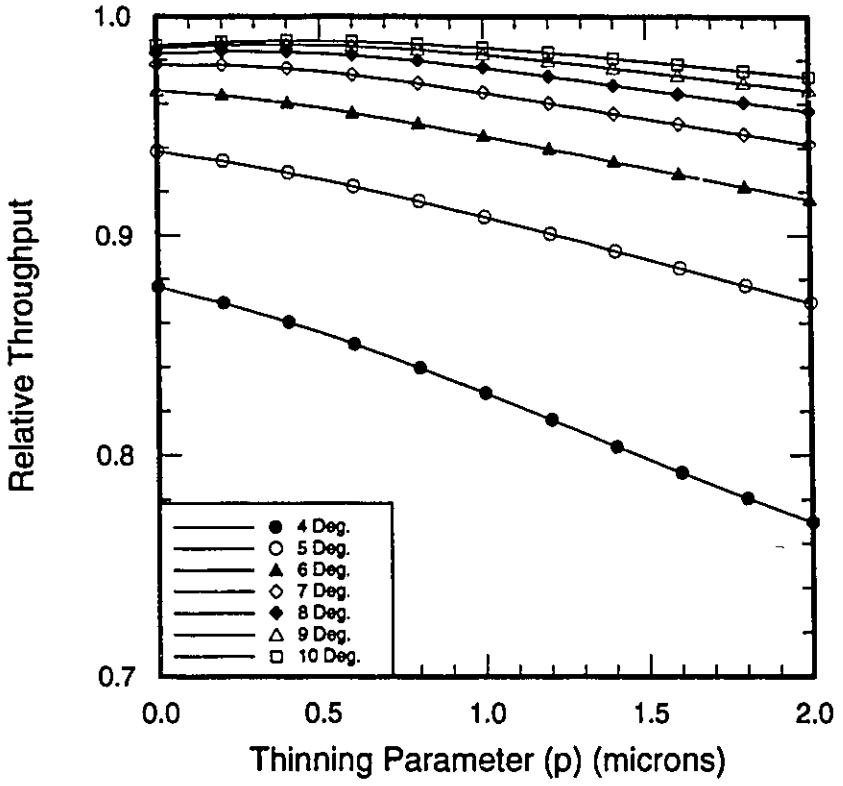

Figure 6.20: The change in throughput relative to an unmodified X-crossing for w = 3.00μm and various thinning parameters, p.

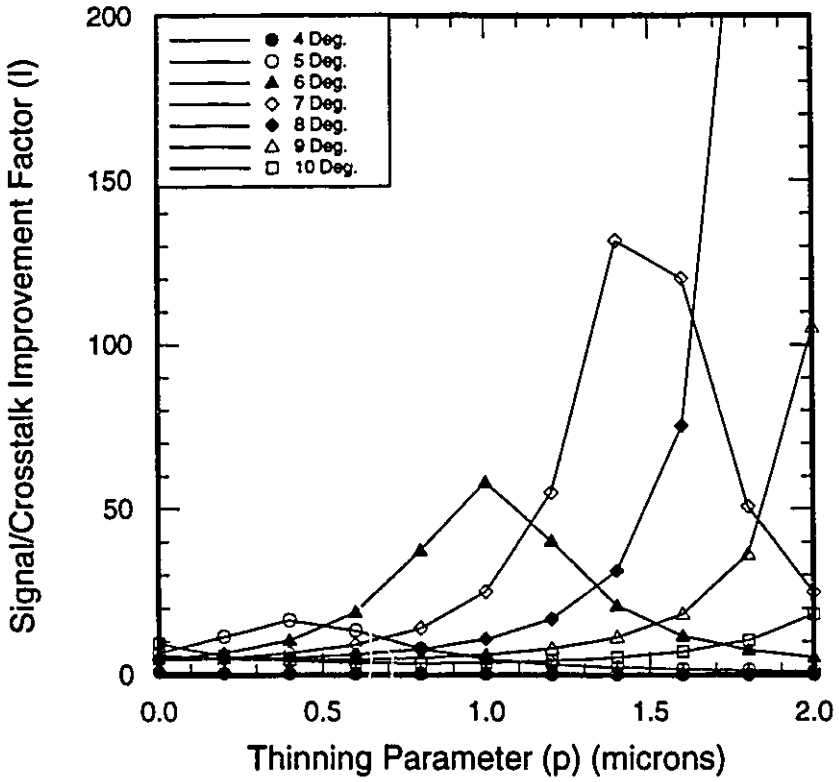

Figure 6.21: The Signal/Crosstalk Improvement Factor for various thinning parameters, p, and w = 3.50μm.

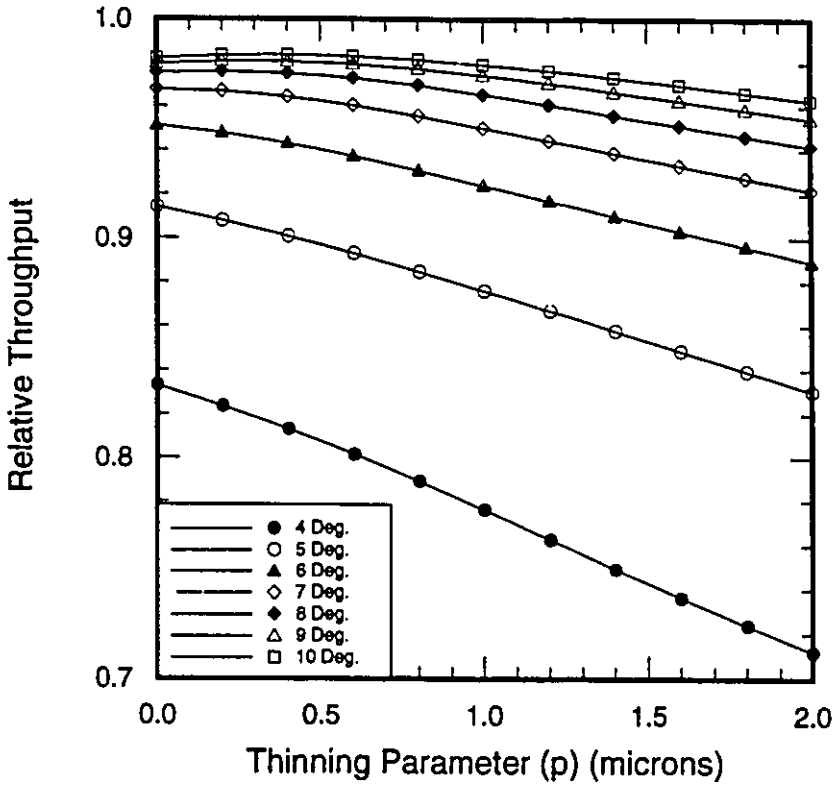

Figure 6.22: The change in throughput relative to an unmodified X-crossing for w = 3.50μm and various thinning parameters, p.

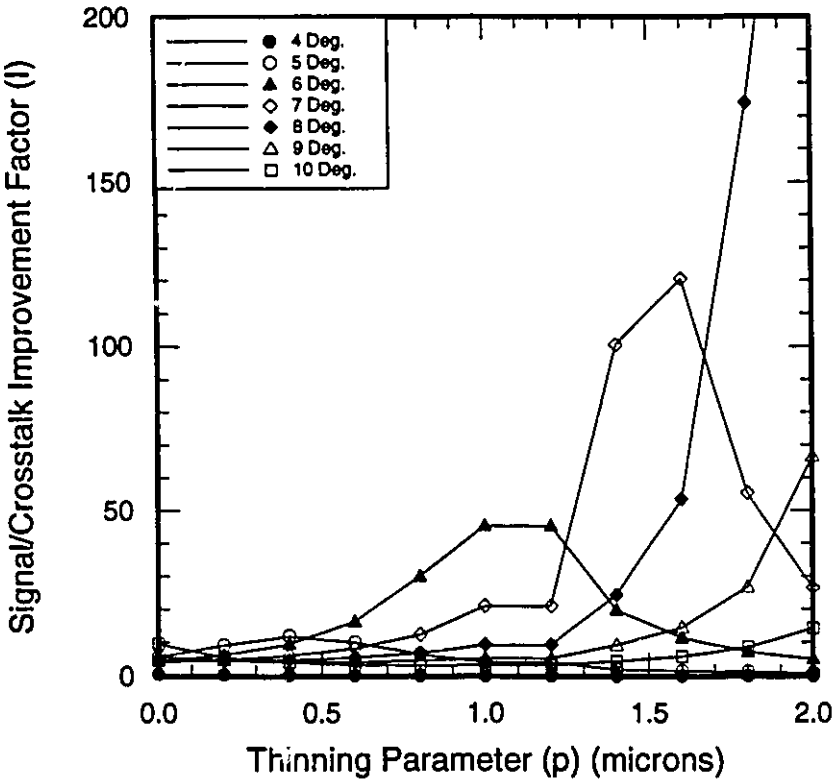

Figure 6.23: The Signal/Crosstalk Improvement Factor for various thinning parameters, p, and w = 4.00μm.

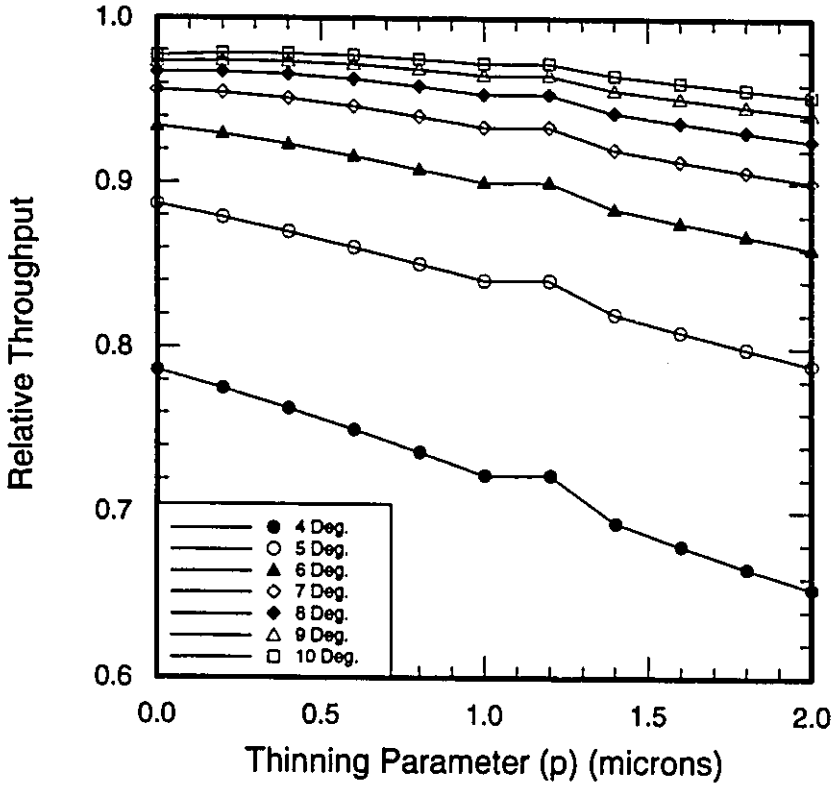

Figure 6.24: The change in throughput relative to an unmodified X-crossing for w = 4.00μm and various thinning parameters, p.

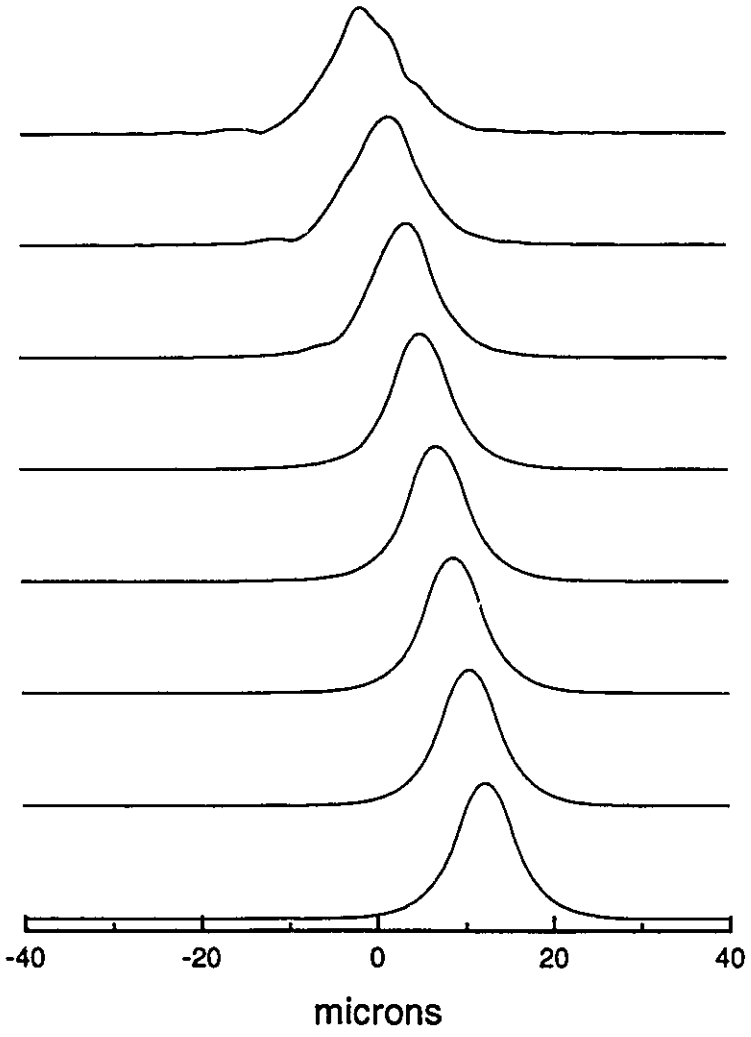

Figure 6.25: The magnitude of the electric field profiles at $z = 10$, 30, 50, 70, 90, 110, 130, and 150μm (from bottom to top) for the structure of Figures 5.2 and 6.6 at 5° with $w = 2.00\mu$m and $p = 0.75\mu$m.

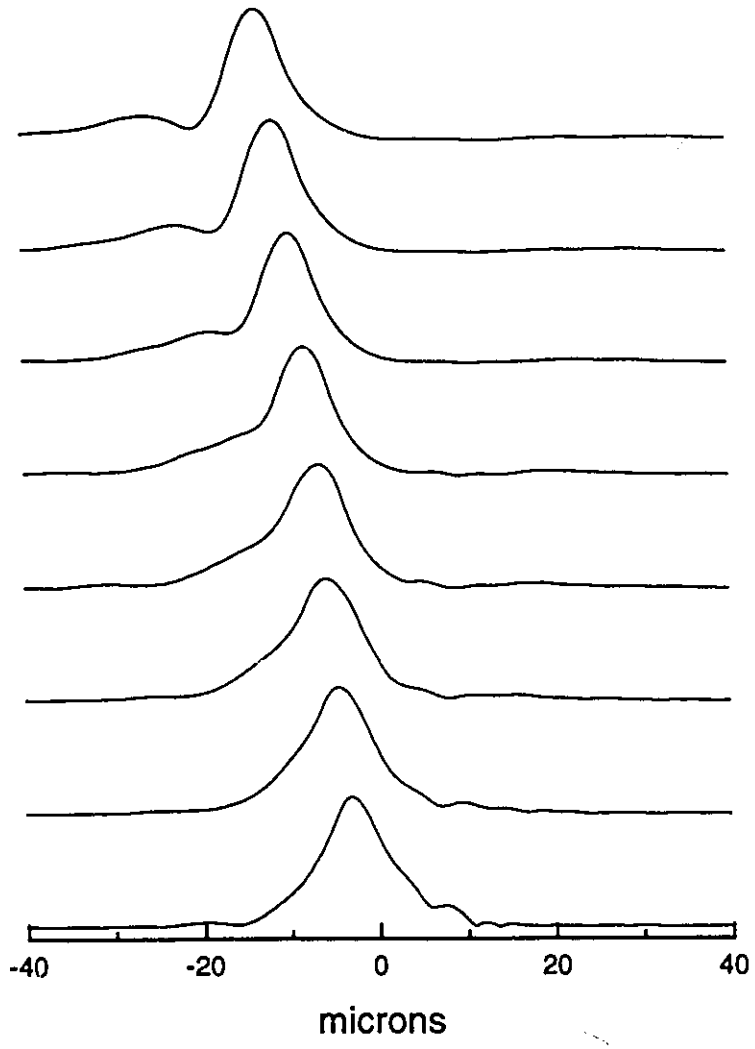

Figure 6.26: The magnitude of the electric field profiles at $z = 170$, 190, 210, 230, 250, 270, 290 and 310μm (from bottom to top) for the structure of Figures 5.1 and 5.2 at 5° with $w = 2.00\mu$m and $p = 0.75\mu$m.

Chapter 7

Conclusions

7.1 Summary of Results

This thesis has studied two problems encountered in designing InP optoelectronic integrated circuits. The first of these problems is the measurement, characterization and modeling of stress in InP waveguides. The degree of polarization method was used to measure the stress in a waveguide that is caused by metal and dielectric overlayers. This stress was modeled and correlated with a change in the refractive index of the waveguide. The refractive index change was shown to be responsible for a large perturbation of the waveguide mode from the expected mode of an unstressed waveguide.

The combination of techniques presented represents a valuable tool for all InP waveguide processors. The presented tools allow for the evaluation of different fabrication processes to minimize process-induced stress which can cause device performance degradation.

The second problem studied is the improvement of the low angle performance of InP crossed waveguides. These structures are important in optoelectronic circuit design and the ability of these crossings to have good performance at low angles increases the designer's parameter space.

Two simple modifications of the standard waveguide X-crossing have been shown to improve the amount of optical crosstalk for some angles by more than 20 dB, leading to a total signal crosstalk which is

40 dB less than the conventional design. These modifications are easily manufactured and merit investigation for any particular waveguide structure under consideration.

7.2 Contributions to the Literature

The work in this thesis resulted in three refereed publications. The first of these publications was on stress in InP waveguides as was discussed in Chapter 4. The second and third publications presented the modifications to the X-crossed waveguides as was discussed in Chapter 6. The publications are listed below:

1. M.G. Daly, D.M. Bruce, P.E. Jessop, Daniel T. Cassidy and David Yevick, Metallization stress in weakly guiding InP/InGaAsP waveguides. *Semicond. Sci. Technol.*, 9:1387, 1994.

2. M.G. Daly, P.E. Jessop and D. Yevick, Intersecting rib waveguide structures with reduced crosstalk. Accepted for publication by *Canadian Journal of Physics* in September 1995.

3. M.G. Daly, P.E. Jessop and D. Yevick, Crosstalk Reduction in Intersecting Rib Waveguides. Accepted for publication by *IEEE J. of Light. Tech.* in November 1995.

Appendix A

Symbol Definitions

Some symbol names are duplicated. It is generally clear from the context which definition applies. Otherwise an effort has been made to clarify the definition in the text.

λ wavelength of light (m).

$\mathbf{k}$ wavevector of light or electrons. $\left(\frac{2\pi}{\lambda}\right)$

σ stress $\left(\frac{\text{dynes}}{\text{cm}^2}\right)$.

ε_0 permittivity of free space $\left(8.854\text{x}10^{-12}\frac{F}{m}\right)$.

ε permittivity of a material $\left(\frac{\text{F}}{\text{m}}\right)$.

ε_r relative permittivity of a material $\left(\frac{\varepsilon}{\varepsilon_0}\right)$.

n refractive index of a material.

$\mathbf{E}$ electric field vector $\left(\frac{\text{V}}{\text{m}}\right)$.

$\mathbf{H}$ magnetic field strength vector $\left(\frac{\text{A}}{\text{m}}\right)$.

$\mathbf{D}$ electric flux density vector $\left(\frac{\text{C}}{\text{m}^2}\right)$.

$\mathbf{M}$ magnetization $\left(\frac{\text{A}}{\text{m}}\right)$.

$\mathbf{B}$ magnetic flux density vector (T).

$\mathbf{P}$ polarization $\left(\frac{\mathrm{C}}{\mathrm{m}^2}\right)$.

$\mathbf{J}$ current density $\left(\frac{\mathrm{A}}{\mathrm{m}^2}\right)$.

μ permeability of a material $\left(\frac{\mathrm{H}}{\mathrm{m}}\right)$.

μ_0 permeability of free space $\left(4\pi \mathrm{x} 10^{-7} \frac{\mathrm{H}}{\mathrm{m}}\right)$.

ρ volume charge density $\left(\frac{\mathrm{C}}{\mathrm{m}^2}\right)$.

∇ grad operator in rectangular coordinates $\left(\nabla = \hat{i}\frac{\partial}{\partial x} + \hat{j}\frac{\partial}{\partial y} + \hat{k}\frac{\partial}{\partial z}\right)$.

∇_T components of the gradient operator perpendicular to the direction of the propagation vector $\left(\nabla_T = \hat{i}\frac{\partial}{\partial x} + \hat{j}\frac{\partial}{\partial y}\right)$.

β propagation constant of the guided mode m^{-1}.

n_{eff} effective refractive index $\left(n_{eff}^L \equiv \frac{\beta_{eff}^L}{k_0}\right)$

Φ generic field vector. Represents either the electric field vector $\mathbf{E}$ or the magnetic field vector $\mathbf{H}$.

ν Poisson's ratio.

E_{el} Young's modulus (Pa).

ρ_{DOP} degree of polarization of photoluminescence.

L light intensity $\left(\frac{\mathrm{W}}{\mathrm{m}^2}\right)$.

M optical matrix element.

K_σ constant of proportionality between the stress and the DOP $\left(\frac{\mathrm{cm}^2}{\mathrm{dynes}}\right)$.

σ stress ($\mathrm{dyn/cm}^2$).

ϵ strain.

ν optical frequency (s^{-1}).

ω radial frequency, $2\pi\nu$ (s^{-1}).

k Boltzmann's constant $\left(1.38\text{x}10^{-23}\frac{J}{K}\right)$

Bibliography

[1] S.E. Miller. Integrated optics: an introduction. *Bell Syst. Tech. J.*, 48(7):2059, 1969.

[2] T. Tamir. *Integrated Optics.* Springer-Verlag, New York, 1975.

[3] R.G. Hunsperger. *Integrated Optics: Theory and Technology.* Springer-Verlag, New York, 1982.

[4] M.J. Adams. *An introduction to optical waveguides.* John Wiley & Sons, Toronto, 1981.

[5] L.M. Walpita. Solutions for planar optical waveguide equations by selecting zero elements in a characteristic matrix. *J. Opt. Soc. Am.*, 2:595, 1985.

[6] E.A.J. Marcatili. Dielectric rectangular waveguide and directional coupler for integrated optics. *Bell Syst. Tech. J.*, 48(9):2071, 1969.

[7] Hiroshi Nishihara, Masamitsu Haruna, and Toshiaki Suhara. *Optical integrated circuits.* McGraw-Hill, Toronto, 1985.

[8] Yariv A. Coupled-mode theory for guided-wave optics. *IEEE Journal of Quantum Electronics*, QE-9:919, 1973.

[9] H.C. Freyhardt, editor. *Crystals: Growth, Properties and Applications*, volume 3, page 75. Springer Verlag, New York, 1980.

[10] E.H.C. Parker, editor. *The Technology and Physics of Molecular Beam Epitaxy.* Plenum, New York, 1985.

[11] R.K. Willardson and A.C. Beer, editors. *Low-Pressure MOCVD of* $Ga_xIn_{1-x}As_yP_{1-y}$ *Alloys.* Semiconductors and Semimetals. Academic Press, Orlando, 1985.

[12] B. Wakefield. Strain-enhanced luminescence degradation in GaAs/GaAlAs double-heterostructure lasers revealed by photoluminescence. *J. Appl. Phys.*, 50:7914, 1979.

[13] M.J. Robertson, B. Wakefield, and P. Hutchinson. Strain-related degradation phenomena in long-lived GaAlAs stripe lasers. *J. Appl. Phys.*, 52:4462, 1981.

[14] A.R. Goodwin, P.A. Kirkby, I.G.A. Davies, and R.S. Baulcomb. The effects of processing stresses on residual degradation in long lived $ga_{1-x}al_xas$ lasers. *Appl. Phys. Lett.*, 42:23, 1979.

[15] M.G. Daly, D.M. Bruce, P.E. Jessop, Daniel T. Cassidy, and David Yevick. Metallization stress in weakly guiding InP/InGaAsP waveguides. *Semicond. Sci. Technol.*, 9:1387, 1994.

[16] P.W. Epperlein, A. Fried, and A. Jakubowicz. Stress-induced defects in GaAs quantum well lasers. *Inst. Phys. Conf. Ser.*, 112:567, 1990.

[17] B. Sieber, J.L. Farvacque, J. Wang, and J.W. Steeds. Possible origin of degradation mechanisms in AlGaAs/GaAs laserlike structures. *Appl. Phys. Lett.*, 60:2654, 1992.

[18] O. Ueda. Degradation of III-V opto-electronic devices. *J. Electrochem. Soc.*, 135:11C, 1988.

[19] H. Shimizu, K. Itoh, M. Wada, T. Sugino, and I. Teramoto. Improvement in operation lives of GaAlAs visible lasers by introduving GaAlAs buffer layers. *IEEE Journal of Quantum Electronics*, QE-17:763, 1981.

[20] W. Both, G. Ebert, A. Klehr, R. Rimpler, G. Stadermann, and U. Zeimer. Catastrophic optical damage in GaAlAs/GaAs laser diodes. *IEE Proc.*, 134(pt. J):95, 1987.

[21] N.B. Patel, J.E. Ripper, and P. Brosson. Behavior of threshold current and polarization of stimulated emission of GaAs injection lasers under uniaxial stress. *IEEE Journal of Quantum Electronics*, QE-9:338, 1973.

[22] N.K. Dutta and D.C. Craft. Effect of stress on the polarization of stimulated emission from injection lasers. *J. Appl. Phys.*, 56:65, 1984.

[23] G.E. Henein and W.R. Wagner. Stresses induced in GaAs by TiPt ohmic contacts. *J. Appl. Phys.*, 54:6395, 1983.

[24] I.A. Blech and E.S. Meieran. Enhanced x-ray diffraction from substrate crystals containing discontinuous surface films. *J. Appl. Phys.*, 38:2913, 1967.

[25] T. Kobayashi, Y. Inoue, T. Nishimura, M. Hirayama, Y. Akasaka, and T. Kato. Local-oxidation-induced stress measured by raman microprobe spectroscopy. *J. Electrochem. Soc.*, 137:1987, 1990.

[26] K. Kawasaki, S. Sakai, N. Wada, and Y. Shintani. Geometrical effects on the thermal stress in GaAs layers grown on Si substrates. *Inst. Phys. Conf. Ser.*, 112:269, 1990.

[27] A. Jakubowicz. Revealing process-induced strain fields in GaAs/AlGaAs lasers via electron irradiation in a scanning electron microscope. *J. Appl. Phys.*, 70:1800, 1991.

[28] F.K. Reinhart and R.A. Logan. Interface stress of $al_xga_{1-x}as-gaas$ layer structures. *J. Appl. Phys.*, 44:3171, 1973.

[29] Daniel T. Cassidy and Charles S. Adams. Polarization of the output of InGaAsP semiconductor diode lasers. *IEEE Journal of Quantum Electronics*, 25(6):1156, 1989.

[30] P. D. Colbourne. *Measurement of Stress in III-V Semiconductors Using the Degree of Polarization of Luminescence.* PhD thesis, McMaster University, 1992.

[31] G.E. Pikus and G.L. Bir. Effect of deformation on the hole energy spectrum of germanium and silicon. *Sov. Phys. Solid State*, 1:1502–1517, 1959.

[32] G.D. Sanders and Y.-C. Chang. Effects of uniaxial stress on the electronic and optical properties of GaAs – $Al_xGa_{1-x}As$ quantum wells. *Phys. Rev. B*, 32(6):4282, 1985.

[33] R.N. Bhargava and M.I. Nathan. Stress dependence of photoluminescence in GaAs. *Phys. Rev.*, 172:695, 1967.

[34] C. Kittel. *Quantum Theory of Solids.* John Wiley & Sons, Toronto, 1987.

[35] E.O. Kane. Band structure of indium antimonide. *J. Phys. Chem. Solids*, 1:249–261, 1957.

[36] Peter S. Zory. *Quantum Well Lasers.* Academic Press, Toronto, 1993.

[37] F.H. Pollak and M. Cardona. Piezo-electroreflectance in Ge, GaAs, and Si. *Phys. Rev.*, 172:816, 1968.

[38] Paul D. Colbourne and Daniel T. Cassidy. Observation of dislocation stresses in InP using polarization-resolved photoluminescence. *Appl. Phys. Lett.*, 61(10):1179, 1992.

[39] M.D. Feit and J.A. Fleck, Jr. Light propagation in graded)index optical fibers. *Appl. Opt.*, 17:3990, 1978.

[40] D. Yevick and B. Hermansson. A split-step fourier transform based analysis of the spontaneous emission factor. *J. Opt. Quant. Elec.*, 17:91, 1985.

[41] D. Yevick and B. Hermansson. A split step finite difference analysis of rib waveguides. *Elect. Lett.*, 25:461, 1989.

[42] David Yevick and Björn Hermansson. New formulations of the matrix beam propagation method: Application to rib waveguides. *IEEE Journal of Quantum Electronics*, 25(2):221, 1989.

[43] B. Hermansson and D. Yevick. Numerical analysis of the modal eigenfunctions of chipped and unchipped multiple-stripe-geometry laser arrays. *J. Opt. Soc. Am.*, 4:379, 1987.

[44] J. Yu. *The Beam Propagation Method and Its Application to the Design of Semiconductor Modulators.* PhD thesis, Queen's University, 1994.

[45] P. D. Colbourne and Daniel T. Cassidy. Imaging of stresses in GaAs diode lasers using polarization-resolved photoluminescence. *IEEE Journal of Quantum Electronics*, 29(1):62, 1993.

[46] Adel. S. Saada. *Elasticity theory and applications.* Robert E. Krieger Publishing Co., Malabar, Florida, 1983.

[47] INSPEC, The Institution ofElectrical Engineers, London and New York. *Properties of Indium Phosphide*, 1991. EMIS Datareviews Series No. 6.

[48] P.A. Kirkby, P.R. Selway, and L.D. Westbrook. Photoelastic waveguides and their effect onstrip-geometry GaAs/GaAlAs lasers. *J. Appl. Phys.*, 50:4567, 1979.

[49] Nobuo Suzuki and Kunio Tada. Elastooptic properties of InP. *Jap. J. Appl. Phys.*, 22(3):441, 1983.

[50] B. Hermansson, D. Yevick, and A. Friberg. Optical coherence calculations with the split-step fast fourier transform method. *Appl. Opt.*, 25:2545, 1986.

[51] P.J. Duthie and M.J. Wale. 16x16 single chip optical switch array in lithium niobate. *Elect. Lett.*, 27(14):1265, 1991.

[52] K. Hamamoto, T. Anan, K. Komatsu, M.Sugimoto, and I. Mito. First 8x8 semiconductor optical matrix switches using GaAs/AlGaAs electro)optic guided wave directional couplers. *Elect. Lett.*, 28(5):441, 1992.

[53] T.O Murphy, R.W. Irvin, and E.J. Murphy. *Uniform low-loss waveguide interconnects*, volume 3, page 184. Optical Society of America, Washington, 1994.

[54] K. Aretz and H. Bulow. Reduction of crosstalk and losses of intersecting waveguide. *Elect. Lett.*, 25(11):730, 1989.

[55] Keiro Komatsu, Kiichi Hamamoto, Mitsunori Sugimoto, Akira Ajisawa, Yuji Kohga, and Akira Suzuki. 4x4 GaAs/AlGaAs optical matrix switches with uniform device characteristics using alternating $\delta\beta$ electrooptic guided wave directional couplers. *IEEE Journal of Lightwave Technology*, 9(7):871, 1991.

[56] Indra Januar and Alan R. Mickelson. Characteristics of s shaped waveguide structures bythe annealed proton exchange process in $LiNbO_3$. *IEEE Journal of Lightwave Technology*, 11(12):2044, 1993.

[57] Kwang T. Koai and Pao-Lo Liu. Modelling of Ti : $LiNbO_3$ waveguidedevices: Part ii – s-shaped channel waveguide bends. *IEEE Journal of Lightwave Technology*, 7(7):1016, 1989.

[58] Henry F. Taylor. Power loss at directional change in dielectric waveguides. *Appl. Opt.*, 13(3):642, 1974.

[59] Hiroaki Takeuchi and Kunishige Oe. Low-loss single-mode GaAs/AlGaAs miniature optical waveguides with straight and bending structures. *IEEE Journal of Lightwave Technology*, 7(7):1044, 1989.

[60] F.J. Mustieles, E. Ballesteros, and P. Baquero. Theoretical S-bend profile for optimization of optical waveguide radiation losses. *Phot. Tech. Lett.*, 5(5):551, 1993.

[61] T. Tamir. *Guided-Wave Optoelectronics.* Springer-Verlag, New York, 2 edition, 1990.